

DEVELOPMENT AND APPLICATIONS OF HIGH TEMPERATURE PIEZOELECTRIC ULTRASONIC TRANSDUCERS

Makiko Kobayashi

(B.Eng., Chiba University – Chiba, Japan, 1997)

(M. Eng., Chiba University – Chiba, Japan, 1999)



Department of Electrical and Computer Engineering

McGill University

Montreal, Quebec, Canada

June 2004

A thesis submitted to McGill University in partial fulfillment of the requirements
of the degree of Doctor of Philosophy.

© Makiko Kobayashi

2004



Library and
Archives Canada

Bibliothèque et
Archives Canada

Published Heritage
Branch

Direction du
Patrimoine de l'édition

395 Wellington Street
Ottawa ON K1A 0N4
Canada

395, rue Wellington
Ottawa ON K1A 0N4
Canada

Your file *Votre référence*

ISBN: 0-494-06314-9

Our file *Notre référence*

ISBN: 0-494-06314-9

NOTICE:

The author has granted a non-exclusive license allowing Library and Archives Canada to reproduce, publish, archive, preserve, conserve, communicate to the public by telecommunication or on the Internet, loan, distribute and sell theses worldwide, for commercial or non-commercial purposes, in microform, paper, electronic and/or any other formats.

The author retains copyright ownership and moral rights in this thesis. Neither the thesis nor substantial extracts from it may be printed or otherwise reproduced without the author's permission.

AVIS:

L'auteur a accordé une licence non exclusive permettant à la Bibliothèque et Archives Canada de reproduire, publier, archiver, sauvegarder, conserver, transmettre au public par télécommunication ou par l'Internet, prêter, distribuer et vendre des thèses partout dans le monde, à des fins commerciales ou autres, sur support microforme, papier, électronique et/ou autres formats.

L'auteur conserve la propriété du droit d'auteur et des droits moraux qui protègent cette thèse. Ni la thèse ni des extraits substantiels de celle-ci ne doivent être imprimés ou autrement reproduits sans son autorisation.

In compliance with the Canadian Privacy Act some supporting forms may have been removed from this thesis.

Conformément à la loi canadienne sur la protection de la vie privée, quelques formulaires secondaires ont été enlevés de cette thèse.

While these forms may be included in the document page count, their removal does not represent any loss of content from the thesis.

Bien que ces formulaires aient inclus dans la pagination, il n'y aura aucun contenu manquant.


Canada

Abstract

High temperature ultrasonic transducers (HTUTs) have been developed for non-destructive evaluation (NDE) of metals and on-line monitoring of industrial polymer processes at elevated temperatures. Developed HTUTs are two types; one is sol gel sprayed HTUTs and the other is a crystal of high Curie temperature permanently bonded onto a steel substrate by brazing or diffusion bonding. In sol gel method, piezoelectric powders were dispersed into sol gel precursor. Sol gel precursor of Al_2O_3 , PZT or BIT, serves as adhesion material between powders, LT, PZT or BIT and a substrate to be coated. Spray technique was used so that thick films could be fabricated even onto curved or large surfaces. The composite material, BIT/PZT, derived from bismuth titanate (BIT) powders and lead zirconate titanate (PZT) sol gel precursor had presented excellent characteristics, such as high signal-to-noise ratio, broadband frequency, and acceptable signal strength up to more than 450°C . The film properties such as dielectric constant, piezoelectric constant, density and electromechanical coupling coefficient were characterized. Nondestructive testing of extent of sub-surface defect using BIT/PZT film HTUT was given at 440°C .

High temperature immersion type HT ultrasonic probes using BIT/PZT film were also fabricated. They were immersed in molten zinc at 450°C , and able to measure the thickness of the steel sample. Surface and sub-surface imaging with fine resolution were obtained using this HT ultrasonic probe with a focused lens in silicone oil at 200°C .

On-line monitoring of industrial polymer processes had been performed. Sol gel HTUTs had been fabricated on a steel extruder adaptor of a polymer extruder machine, mold inserts of an injection machine and a micro-molding machine, and a barrel of the micro-molding machine. Ultrasonic signals were obtained at the elevated temperatures. The capability for monitoring the barrel wear and screw status during polymer extrusion at 190°C and the filling completion conditions for injection molding at 120°C and micro-molding processes up to 200°C have been shown.

Brazing and diffusion bonding had been tried to establish permanent acoustic bonding between a lithium niobate crystal and a steel substrate. The HTUT fabricated by brazing technique had demonstrated broadband characteristics up to 460°C. The HTUT made by diffusion bonding technique had also demonstrated broadband characteristics up to 350°C. This latter HTUT had 20 dB higher signal strength than that of the sol gel BIT/PZT thick film HTUTs.

Résumé

Des capteurs ultrasoniques à hautes températures (CUHT) ont été développés pour l'évaluation non destructive des métaux et pour le suivi en ligne des procédés industriels de polymères aux températures élevées. Les CUHTs développés sont de deux types: l'un est basé sur la pulvérisation d'un gel de solénoïde contenant des particules piézoélectriques sur un substrat métallique, et l'autre est un cristal piézoélectrique à température de Curie élevée collée de façon permanente sur un substrat en acier soit par la soudure ou par l'adhésion par diffusion. Dans la méthode de gel de solénoïde, des poudres piézoélectriques sont dispersées dans un précurseur de gel de solénoïde. Le précurseur de gel de solénoïde à base d' Al_2O_3 , ou de titanate de zirconate de plomb (PZT), ou de titanate de bismuth (BIT), sert de matériau adhésif entre les particules de la poudre de titanate de lithium (LT), ou de PZT, ou de BIT, et le substrat à enduire. Une technique de pulvérisation a été utilisée de sorte que des films épais aient pu être fabriqués même sur les surfaces incurvées ou grandes. Le matériau composite, BIT/PZT, obtenu par l'utilisation de la poudre BIT et le précurseur de gel de solénoïde à base de PZT ont présenté d'excellentes caractéristiques, telles que le rapport signal-sur-bruit élevé, une large bande passante de fréquence, et le niveau d'intensité acceptable du signal jusqu'à qu'à 450°C ou plus. Les propriétés de film telles que la constante diélectrique, la constante piézoélectrique, la densité et le coefficient d'accouplement électromécanique ont été mesurées. Une évaluation non-destructive du défaut sous-surface d'un échantillon a été effectuée à 440 °C à l'aide d'un CUHT à base du film de BIT/PZT.

Des CUHTs d'immersion employant le film de BIT/PZT ont été également fabriqués. Ils ont été immergés dans le zinc fondu à 450 °C et ont montré la capacité de mesurer l'épaisseur d'un échantillon en acier immergé également dans le zinc fondu. Des images à fine résolution sur la surface vers le haut et celle vers le bas d'une pièce de monnaie des USA ont été obtenues dans une huile de silicone à 200 °C en utilisant un CUHT d'immersion focalisée du même type.

Le suivi en ligne de la mise en forme industrielle des polymères ont été effectués. Des CUHTs à base du film de BIT/PZT ont été fabriqués sur un adaptateur en acier monté sur une extrudeuse de polymère, sur la moule d'insertion d'une machine d'injection, et sur la moule d'insertion et le fourreau d'une machine de micro-moulage. Des signaux ultrasonores ont été obtenus aux températures élevées. Le suivi par l'utilisation ces capteurs de l'usure du fourreau et de l'état de la vis pendant l'extrusion de polymère à 190 °C, ainsi que le suivi des conditions de remplissage de la moule durant l'injection à 120°C et durant le micro-moulage aux températures jusqu'à 200°C ont été montrés.

Des CUHT employant un cristal de niobate de lithium ont été fabriqués et étudiés. La soudure et l'adhésion par diffusion ont été essayées pour créer une liaison permanente entre un cristal de niobate de lithium et un substrat en acier. Le CUHT fabriqué par la technique de soudure a montré une large bande passante de fréquence jusqu'à 460 °C. Le CUHT fait par la technique d'adhésion par diffusion a également montré une large bande passante de fréquence jusqu'à 350°C. Ce dernier a été 20 dB plus puissant que le CUHT à base du film épais de BIT/PZT.

Acknowledgements

I would like to thank my supervisor Dr. C.-K. Jen for his guidance, support and encouragement throughout this study. I appreciate him for what I have learned through him concerning research, optimism and organization about the projects.

I would also like to thank to Industrial Materials Institute (IMI), National Research Council of Canada (NRCC), where the thesis research was performed, for the technical expertise and use of equipment.

My gratitude goes to the members of Characterization and Ultrasonic Sensor Group, Modeling and Diagnostics Section at IMI for their help and friendship. Special thanks go to Mr. C. Corbeil for his kindness, support, suggestions and collaboration of this work, in particular in Chapter 2 and Chapter 4. Many experimental set-ups were provided by him. I would particularly like to acknowledge and thank Dr. Y. Ono for his assistance, help, and collaborations to the experiments in Chapter 4 and Chapter 5 and invaluable comments in reviewing this thesis. I am also indebted to Mr. H. Hébert for implementing most of the data acquisition and signal processing programs used in this research, and helpful discussions with respect to Chapter 6. I would also express my appreciation to Dr. Z. Sun for his collaboration and useful comments in this thesis, particularly in Chapter 5. Many thanks are also devoted Mr. J.-F. Moison, Mr. Y. Zhang, Dr. A. Derdouri, Mr. M. Thibodeau, Mr. Y. Simard and Mr. C.-C. Cheng for their contributions which make my work complete.

My appreciation is given to the people at the Applied Solid State group, at the Applied Physics Department at Queen's University: Prof. M. Sayer, Mr. T.R. Olding, Ms. L. Zou, Dr. A. Houlson and Dr. G. Pang for their collaboration regarding Chapter 2.

I am deeply grateful to Mr. Z. Wang for his suggestions in Chapter 3. I greatly appreciate Prof. I. Shih for providing evaporated and sputtered metal layers; and Mr. A. Bloch for English corrections.

My sincere thanks go to my colleagues, including Dr. D.R. França, Dr. E. Chen, Dr. A-U. Rehman, Mr. H.-L. Liang, Mr. J. Yan, Mr. Mr. D.-H. J. Zhao and Mr. H.-C. Paul for their encouragement during my study.

I wish to thank the years of help and encouragement given by my parents, my sister Naoko, and my friend David. And last, I thank the Lord for giving me perspective and purpose in my thesis research.

Table of Contents

Abstract	i
Résumé	iii
Acknowledgments	v
Table of Contents	vii
List of Figures	x
List of Tables	xvii
List of Symbols	xviii
Chapter 1: Introduction	1
1.1- Background.....	1
1.2- HTUTs for nondestructive testing of metals and real-time industrial material processing monitoring.....	9
1.2.1- Sol gel spray HTUTs.....	9
1.2.2- HTUTs permanently bonded onto metal substrates.....	12
1.3- Thesis content.....	14
Chapter 2: Sol gel spray coating technique	16
2.1- Introduction.....	16
2.2- Fabrication process.....	17
2.2.1- Powder selection.....	18
2.2.2- Sol gel preparation.....	25
2.2.3- Ball milling.....	27
2.2.4- Substrate preparation.....	28
2.2.5- Spray coating.....	30
2.2.6- Heat treatment.....	31
2.2.7- Poling.....	32
2.2.8- Electrode fabrication.....	45
2.3- Summary.....	46
Chapter 3: Sol gel spray composite film properties	47
3.1- Introduction.....	47

3.2-	Piezoelectric film properties.....	48
3.3-	Measurement of sol gel sprayed film properties.....	54
3.3.1-	Dielectric constant.....	54
3.3.2-	Piezoelectric constants d_{33} , g_{33}	56
3.3.3-	Thickness mode electromechanical coupling factor k_t	59
3.4-	Ultrasonic performance of sol gel composite films.....	66
3.4.1-	PZT/PZT.....	66
3.4.2-	PZT/ Al_2O_3	67
3.4.3-	LT/PZT.....	68
3.4.4-	BIT/PZT.....	70
3.5-	Durability test.....	71
3.6-	Summary.....	72
Chapter 4:	Applications of sol gel composite HTUTs for nondestructive evaluation of materials at high temperature	73
4.1-	Introduction.....	73
4.2-	Ultrasonic performance of BIT/PZT films on various surfaces.....	74
4.2.1-	Cylindrical convex surfaces.....	74
4.2.2-	Spherical convex surfaces (ball).....	76
4.2.3-	Cylindrical and spherical concave surfaces.....	78
4.2.4-	Thin metal sheets and foils.....	80
4.3-	Self-support film.....	82
4.4-	NDE of steels at high temperatures.....	83
4.5-	Immersion HT ultrasonic thickness measurement and imaging.....	88
4.5.1-	Immersion HT ultrasonic probe.....	89
4.5.2-	Ultrasonic thickness measurement in molten zinc.....	91
4.5.3-	Ultrasonic imaging in silicone oil at 200°C.....	92
4.6-	Summary.....	101
Chapter 5:	Applications of sol gel composite HTUTs for on-line ultrasonic monitoring of polymer process	102
5.1-	Introduction.....	102
5.2-	Polymer extrusion: Barrel and screw status.....	103

5.3- Polymer injection molding.....	114
5.4- Micro-molding.....	124
5.5- Summary.....	131
Chapter 6: Development of HTUTs using brazing and diffusion bonding techniques	132
6.1- Introduction.....	132
6.2- Brazing HTUTs.....	134
6.3- HTUTs with diffusion bonding.....	142
6.4- Summary.....	154
Chapter 7: Conclusion	155
7.1- Thesis summary.....	155
7.2- Claims of originality.....	159
Appendix A	161
References	166

List of Figures

Figure 1.1: Schematic showing a signal and associated noise.....	5
Figure 2.1: Flowchart of fabrication process by sol gel spray coating technique.....	18
Figure 2.2: Phase diagram of PZT solid solution. P _C : paraelectric cubic, A: antiferroelectric, F _R : ferroelectric, rhombohedral, F _T : ferroelectric, tetragonal.....	20
Figure 2.3: Dielectric constant ϵ and planar electromechanical coupling factor k_p versus composition of PZT [90].....	21
Figure 2.4: Crystal lattice distortion and ion shifts a) PZT above Curie temperature, b) poled PZT below Curie temperature.....	21
Figure 2.5: Crystal lattice of BIT above Curie temperature.....	24
Figure 2.6: Process sequence for PZT sol gel developed by Queen’s University [67].....	26
Figure 2.7: Chemical reaction of metal oxide film to a substrate [66].....	29
Figure 2.8: Setup of sol gel spraying.....	31
Figure 2.9: Spontaneous polarization versus electric field [104].....	33
Figure 2.10: Temperature and current transition during successful traditional poling for LT/PZT.....	34
Figure 2.11: Temperature and current transition during traditional poling with dielectric breakdown for PZT/Al ₂ O ₃	34
Figure 2.12: The experimental setup for corona poling.....	36
Figure 2.13: Corona discharge.....	36
Figure 2.14: Comparison of color change after corona poling of BIT/PZT. The sample numbers correspond to those of Table 2.4.....	39
Figure 2.15: Comparison of color change after corona poling of PZT/PZT. The sample numbers correspond to those of Table 2.5.....	41
Figure 2.16: XRD of PZT/PZT.....	43
Figure 2.17: XRD of BIT/PZT.....	43

Figure 2.18: Comparison of color change before (a) and after (b) corona poling of PZT/Al ₂ O ₃	44
Figure 3.1: Comparison of relative dielectric constant calculations of powder/PZT sol gels from conventional cube model and double cube model including pores, as a function of the relative dielectric constant of powder, with experimental results.....	56
Figure 3.2: A schematic of a Berlincourt meter.....	57
Figure 3.3: A two-layer composite resonator produced by the sol gel spray..... technique, with the definitions of the material parameters and dimension...	60
Figure 3.4: The impedance of a 60 μm BIT/PZT film on a steel substrate composite resonator as a function of frequency.....	64
Figure 3.5: The SPRF of a 60 μm BIT/PZT film on a steel substrate composite resonator as a function of frequency.....	64
Figure 3.6: The k_{eff}^2 of a 60 μm BIT/PZT film on a steel substrate composite resonator as a function of frequency.....	65
Figure 3.7: Signals in time domain of PZT/PZT film.....	66
Figure 3.8: Signal in frequency domain of PZT/PZT film for L ¹ of the device depicted in Figure 3.7.....	67
Figure 3.9: Ultrasonic performance in time and frequency domains of a 100 μm PZT/Al ₂ O ₃ film at room temperature.....	68
Figure 3.10: Ultrasonic performance in time and frequency domains of a 60 μm LT/PZT film deposited on a clad steel buffer rod, at room temperature..	69
Figure 3.11: Ultrasonic performance in time domain of a 60 μm LT/PZT film.. deposited on a clad steel buffer rod, at temperatures from 30°C to 250°C...	69
Figure 3.12: Ultrasonic signals reflected at the bottom (a), and frequency spectrum (b), of an 80 μm BIT/PZT film on a 12 mm thick steel substrate at room temperature and 625°C.....	70
Figure 3.13: Ultrasonic signal of BIT/PZT film in frequency domain at 625°C for L ¹ of the device depicted in Figure 3.12.....	71
Figure 4.1: A 40 μm thick BIT/PZT film deposited onto a cylindrical steel shell	75

Figure 4.2: The ultrasonic performance (a) in time and (b) frequency domain for L^1 at 440°C of the device depicted in Figure 4.1.....	75
Figure 4.3: A 90 μm thick BIT/PZT film deposited onto a spherical steel ball of 19 mm diameter.....	76
Figure 4.4: The ultrasonic performance (a) in time and (b) frequency domain for L^1 at 440°C of the device depicted in Figure 4.3.....	77
Figure 4.5: A 90 μm thick BIT/PZT film deposited onto a cylindrical concave steel surface.....	78
Figure 4.6: A 90 μm thick BIT/PZT film deposited onto a spherical concave steel surface.....	79
Figure 4.7: Thick BIT/PZT film deposited on a (a) 400 μm thick stainless steel, (b) 75 μm thick titanium, (c) 45 μm thick nickel and (d) 145 μm thick copper substrate.....	80
Figure 4.8: Ultrasonic performance of a 60 μm thick BIT/PZT film deposited on a 400 μm thick stainless steel sheet in time domain at 440°C.....	81
Figure 4.9: Self-support BIT/PZT sheet.....	82
Figure 4.10: Self support BIT/PZT spherical shell.....	82
Figure 4.11: Ultrasonic monitoring of an artificial horizontal defect extent at 440°C.....	84
Figure 4.12: Ultrasonic monitoring of an artificial vertical defect extent at 440°C.....	84
Figure 4.13: Schematic of ultrasonic monitoring for large substrate at elevated temperature.....	85
Figure 4.14: Set up of ultrasonic monitoring for a large substrate at elevated temperature.....	86
Figure 4.15: Ultrasonic performance of an 80 μm thick BIT/PZT film deposited on a supporting plate attached to a large substrate in (a) time and (b) frequency domains of L_2 at 520°C.....	87
Figure 4.16: HT ultrasonic probe consisting of a BIT/PZT HTUT fabricated onto a steel buffer rod.....	89
Figure 4.17: HT immersion type ultrasonic probe with a holder.....	90

Figure 4.18: Schematic diagram of ultrasonic thickness measurement in molten zinc at 450°C.....	
Figure 4.19: Ultrasonic signals for thickness measurement in molten zinc at 450°C.....	90
Figure 4.20: HT probe with an ultrasonic lens.....	91
Figure 4.21: Ultrasonic imaging set-up.....	92
Figure 4.22: American one cent coin used for imaging experiments. The tail side had its figures but the head side was polished to be flat.....	93
Figure 4.23: Ultrasonic signals from the rod and the sample (a) in water at room temperature and (b) in silicone oil at 200°C.....	93
Figure 4.24: Ultrasonic signals obtained when a front surface of the sample is at focus of the lens (a) in water at room temperature and (b) in silicone oil at 200°C.....	96
Figure 4.25: Ultrasonic images of a US coin in water at room temperature, obtained by plotting (a) the amplitude and (b) the time delay of the echo.....	97
Figure 4.26: Ultrasonic images of a US coin in silicone oil at 200°C, obtained by plotting (a) the amplitude and (b) the time delay of the echo.....	98
Figure 4.27: Ultrasonic signals obtained when a back surface of the sample was at focus of the lens (a) in water at room temperature and (b) in silicone oil at 200°C.....	98
Figure 4.28: Ultrasonic sub-surface images of US coin in water at room temperature, obtained by plotting (a) the amplitude and (b) the time delay of the echo.....	99
Figure 4.29: Ultrasonic sub-surface images of US coin in silicone oil at 200°C, obtained by plotting (a) the amplitude and (b) the time delay of the echo.....	100
Figure 5.1: (a) A schematic diagram of the ultrasonic waves propagating in the extruder barrel and polymer melt and (b) the example of the echoes.....	100
Figure 5.2: Four LT/PZT UTs deposited on the top surface of an extruder barrel adaptor.....	105
Figure 5.3: LT/PZT UTs on the top surface of an extruder barrel adaptor in a W&P 30-mm twin-screw extruder.....	107
	108

Figure 5.4: Echoes reflected from the extruder barrel adaptor/molten polymer interface.....	108
Figure 5.5: Sol gel sprayed BIT/PZT HTUTs deposited onto the top external surface of an extruder adaptor placed at the pumping zone of the extruder...	109
Figure 5.6: Echoes reflected at the adaptor/molten polymer interface and received by the sol gel sprayed BIT/PZT HTUT shown in the center of Figure 5.5.....	110
Figure 5.7: Evolution of echoes reflected at the adaptor/molten polymer interface (L^1) and from the screw flight (L_{2F} , L_{4F} , and L_{6F} , etc.) at the pumping zone with the sol gel- sprayed BIT/PZT HTUT during the first 40s of data acquisition. Letters A and B denote echoes reflected by the tip of each screw flight within one revolution.....	112
Figure 5.8: A single trace of signal extracted from Figure 5.7 (a) at 0.25 s process time.....	113
Figure 5.9: Cycle of the injection molding process: (i) the filling stage; (ii) the packing, holding and solidification stage; (iii) the mold opening stage; and (iv) the part ejection stage.....	115
Figure 5.10: HTUT sensor inserts with (right) and without (left) electrical connection, used for monitoring the injection molding process.....	116
Figure 5.11: A mobile mold and a large mold insert with four embedded HTUT sensor inserts (small inserts).....	117
Figure 5.12: Cross-sectional view of the mold (mobile and immobile), large mold insert with four HTUT sensor inserts (UTs 1-4), and molded part (polymer melt). L^n and L_{2n} ($n=1,2,3\dots$) represent n-th round trip echoes propagating in the mold insert and the polymer, respectively.....	118
Figure 5.13: Typical signals measured with UT1 during injection molding.....	120

Figure 5.14: (a) Amplitude variations of L^4 and L_2 echoes measured with UT1, and (b) temperature (solid line) and pressure (dotted line) variation measured with a Kistler sensor during injection. Arrows A, B and C indicate the times of flow front arrival at UT1 location, mold opening and part ejection, respectively	121
Figure 5.15: One incomplete (#1) and three complete (#2-4) molded parts under the same molding conditions. Filling rate of part #1 was 99%.....	123
Figure 5.16: Amplitude variation of L_2 echoes measured during injection cycles for parts #1-4 shown in Figure 5.15.....	124
Figure 5.17: A part feed hopper and barrel sections of a Battenfeld Microsystem 50.....	125
Figure 5.18: BIT/PZT UTs fabricated on the barrel of a micro-molding machine.....	126
Figure 5.19: BIT/PZT UTs fabricated on the mold insert of a micro-molding machine.....	127
Figure 5.20: Schematic view of ultrasonic signals propagating in the barrel and the polymer melt.....	127
Figure 5.21: Ultrasonic signals reflected at the barrel/PE melt and PE melt/screw interfaces measured with the UT6 at the heating zone of the barrel.....	128
Figure 5.22: Schematic view of ultrasonic signals propagating in the mold insert and the PE melt.....	129
Figure 5.23: Ultrasonic signals reflected at the mold insert/PE melt interfaces, measured by UT1 above 1 mm-thick PE melt (a), and by UT2 above 0.3 mm-thick PE melt (b).....	129
Figure 5.24: Velocity change of PE in the cavity of the mold insert during solidification.....	130
Figure 6.1: Schematic of a broadband UT with high loss backing material.....	133
Figure 6.2: Schematic of a Broadband UT with a metallic delay line.....	134
Figure 6.3: Schematic of sessile drops and interfacial energies (a) non-wetting (b) wetting.....	136
Figure 6.4: Vacuum furnace for brazing.....	139

Figure 6.5: A cross section of the assembly for vacuum brazing.....	139
Figure 6.6: A sample of a LN HTUT brazed to a delay line.....	140
Figure 6.7: Time domain of ultrasonic signal obtained from the sample seen in Figure 6.6 at 460°C.....	141
Figure 6.8: Frequency domain of ultrasonic signal obtained from the sample seen in Figure 6.6 at 460°C.....	141
Figure 6.9: Mechanism of diffusion in a metallic lattice: (a) exchange of places between two adjacent atoms, (b) motion of interstitial atoms, (c) circular exchange of four atoms, and (d) motion of vacancies.....	143
Figure 6.10: The diffusion bonding unit.....	146
Figure 6.11: An exploded view showing the components before the diffusion bonding process.....	146
Figure 6.12: A diffusion-bonded LN HTUT.....	148
Figure 6.13: Time domain of ultrasonic signals obtained from the sample gold- and aluminium-diffusion bonded at 300°C.....	149
Figure 6.14: Time domain of ultrasonic signals obtained from a sample gold diffusion-bonded at 300°C.....	149
Figure 6.15: Frequency domain of ultrasonic signals corresponding to Fig.6.13	150
Figure 6.16: Frequency domain of ultrasonic signals corresponding to Fig.6.14	150
Figure 6.17: Durability test for a diffusion-bonded LN HTUT under thermal cycles between room temperature and 300°C.....	151
Figure 6.18: Graded alpha technique designed to reduce thermal expansion coefficients.....	152
Figure A.1: Schematic representations for (a) parallel and (b) series models	163
Figure A.2: Schematic representation of 0-3 composite.....	164
Figure A.3: Schematic representation of unit cell models for 0-3 composite material.....	164
Figure A.4: Comparison of relative dielectric constant calculations of powder/PZT sol gels from conventional cube model and double cube model including pores, as a function of the relative dielectric constant of powder, with experimental results (duplication of Figure3.1).....	166

List of Tables

Table 2.1:	Electrical, mechanical, and electromechanical properties of PZT powder provided by Piezo Kinetics Inc.....	22
Table 2.2:	Basic properties of LT and LN.....	23
Table 2.3:	Electrical, mechanical, and electromechanical properties of BIT powders.....	24
Table 2.4:	Comparison of results for poling temperature and applied DC voltage for BIT/PZT corona poling and signal strength of the first reflected signal from the bottom of each substrate with the same thickness.....	37
Table 2.5:	Comparison of results for poling temperature, applied DC voltage, and the distance between the needle and the sample during PZT/PZT corona poling.....	40
Table 3.1:	Measured dielectric constants and dissipation factors.....	55
Table 3.2:	Measured piezoelectric constant d_{33} and g_{33}	58
Table 4.1:	Calculated results of the focusing ability of ultrasound.....	94
Table 6.1:	Characteristics of Braze 630.....	138
Table 6.2:	Thermal expansion coefficients α of typical metals.....	153

List of Symbols

α	thermal expansion coefficient
A	area
AC	alternating current
a_i	impact strength
Al	aluminium
AlN	aluminium nitride
Al ₂ O ₃	alumina (aluminium oxide)
Au	gold
β	dielectric impermeability
B	volume
B_F	volume fraction
BAW	bulk acoustic wave
BIT	bismuth titanate
C	capacitance
c	elastic stiffness
C_0	clamped capacitance
Cr	chromium
Δ	determinant
D	electric displacement
d	piezoelectric constant
DC	direct current
Δf	spacing of parallel resonant frequencies
dr	lateral resolution
ΔT	time delay
δt	wear
dz	focusing depth
ϵ	dielectric constant

E	electric field
e	piezoelectric constant
E_c	coercive field
EMAT	electromagnetic acoustic transducer
ϵ_r	relative dielectric constant
ϵ_0	dielectric constant of free space
F	force
f_a	antiresonance frequency
FFT	fast Fourier transform
f_m	frequency of maximum impedance
f_n	frequency of minimum impedance
f_p	parallel frequency
F_R	ferroelectric rhombohedral structure
f_r	resonance frequency
f_s	series frequency
F_T	ferroelectric tetragonal structure
Γ	correction factor
γ	phase delay
g	piezoelectric constant
η	viscosity
H	hydrogen
h	piezoelectric constant
\hbar	Planck's constant
HDPE	high-density polyethylene
HT	high temperature
HTUT	high temperature ultrasonic transducer
k	electromechanical coupling coefficient
k_{eff}	effective electromechanical coupling coefficient
k_t	thickness mode electromechanical coupling coefficient
λ	wave length
L	longitudinal round trip echo

l	focal length
LDPE	low-density polyethylene
LN	lithium niobate
LT	lithium tantalate
M	metal
MEMS	micro electromechanical systems
m_N	mode order at the center of the first normal region
m_T	mode order at the center of the first transition region
NDE	nondestructive evaluation
O	oxide
Π	pressure
P	polarization
Pb	lead
PC	polycarbonate
PE	polyethylene
PMN	lead magnesium niobate
PT	lead titanate
PZN	lead zirconate niobate
PZT	lead zirconate titanate
PVC	polyvinyl chloride
θ	angle
Q_e	electrical quality factor
Q_e^{-1}	dissipation factor
ρ	density
R	alkyl radical
\underline{R}	Boltzman's constant
r	radius
RF	radio frequency
RS	resonance spectrum
s	elastic compliance
S	strain

SAW	surface acoustic wave
SNR	signal-to-noise ratio
SPRF	spacing of parallel resonant frequency
SS	stainless steel
σ	tensile strength
T	stress
τ	temperature
t	thickness
T_c	Curie temperature
Ti	titanium
U	energy
U_M	factor related to the mechanical energy to deform a volume B
U_N	factor related to the thermal energy imparted to the same volume B
UT	ultrasonic transducer
V	voltage
v	velocity
ω	angular frequency
ξ	particle displacement
XRD	X-ray diffraction
ζ	deformation
Z	impedance
Zr	zirconium
Z_{sb}	normalized acoustic impedance of substrate

Chapter 1

Introduction

1.1- Background

Nondestructive evaluation (NDE) of materials has attracted considerable attention for the last several decades [1,2]. Sensors and actuators may be embedded into or bonded directly onto these materials and structures, so that they can be employed as ultrasonic sensors and actuators effectively. Piezoelectric materials are key candidates for such application, since they can be used as both sensors and actuators. Lead zirconate titanate (PZT) has been often utilized for many piezoelectric and ultrasonic applications, because it has a high electromechanical coupling factor [1,3]. Effective sensors, materials and structures are demanded to improve the performance for aerospace, transportation, construction, and other engineering systems [2,3]. However, most previous sensors have focused on room temperature operations and implementation of them in aerospace and other areas may be limited because of the severe conditions, such as large temperature variations [4]. Furthermore, during industrial operations, such as at nuclear power generation plants [5,6], galvanization plants [7], *etc.*, inspection of hot objects in harsh environments is required to avoid serious accidents such as leakage of hot steam or molten zinc. High spatial resolution and miniaturization of high temperature (HT) sensors are essential in order to develop a convenient inspection system that can operate under such severe conditions.

Furthermore, on-line monitoring is desired for industrial polymer processes because it is important for industries to strengthen their competitiveness in an increasingly globalized world. High quality products with varieties and in low cost become crucial objective for any industries to exist and grow. This leads to the recent developments in advanced polymers and processes, and improved process monitoring and

control of material processing [8-13]. On-line feedback from the monitoring sensors to the control system allows direct supervision of the manufacturing process, and assures the quality of the finished products [8-11,14,15]. Most industrial polymer processes are operated at elevated temperatures up to 350°C. Therefore, the development of cost effective HT sensors for on-line monitoring is of great interest [8,9,14,16,17].

Conventional sensors to monitor and control industrial material processes are mostly limited to thermocouple and pressure sensors. However, both types of sensors have limitations, such as slow response, unsteadiness, and non-repeatability, which often do not satisfy the necessary requirements for an on-line measurement system [18]. For example, melt temperature is measured by thermocouples, which have large thermal mass in order to protect the probe against the abrasion and high pressure, resulting in slow response [8]. Also sensitivity must be taken into account. Commonly pressure sensors have a threshold below which reliable reading may not be obtained. In addition, for polymer injection molding process, polymer melt flow speed and the filling condition are crucial process parameters. Although pressure and temperature sensors can be used to detect these parameters, however, due to the slow response time or low sensitivity, the measured melt arrival and filling time is usually slightly longer than the actual time. This fact means that these two conventional sensors cannot provide accurate measurements [19].

Furthermore, these traditional sensors need to contact with or be located very close to the melt being monitored. Access holes often need to be drilled to the manufacturing machine in most cases. Such drilling may not be acceptable by the manufacturer. Micro-molding process is a mass production technique to manufacture of so called lab-on-a-chip devices [20-22]. This process can mold micro channels with extreme precision, a key to fabricate disposable, miniature diagnostic devices in large quantity. Therefore, this fabrication process is an alternative to replace the present expensive serial fabrication methods associated with silicon substrates, and promises breakthroughs for micro electromechanical systems (MEMS). However, polymers must be selected and modified to meet the requirements of the narrow process windows

involved with their flow, solidification and microstructure development in micron-sized channels. Because of this complexity, on-line and fast response process monitoring is in demand to improve the quality of the product and optimize the process [23]. For this process, the above mentioned temperature and pressure sensors present difficulties with regard not only to on-line monitoring and response time, but also sensor placement, since the machine size for micro-molding is much smaller than that of conventional injection molding. Miniature sensors attached to the barrel and the mold are highly desired.

In addition, there is a demand to monitor the barrel and screw status for polymer extrusion. During polymer or metal extrusion process, barrel wear, screw wear, screw misalignment and these deflections are crucial factors affecting the quality of the product. Wears occur because of various reasons, such as abrasion, corrosion, delamination, *etc.* [24-26]. Wear can be reduced by methods such as proper selection of barrel and screw materials or coatings, but screw and barrel wear is inevitable. Once wear occurs, the clearance between the screw flight and the barrel increases. Even a relatively small increase in clearance can cause a significant loss of production efficiency, because of leakage flow [26-28]. Generally, in order to check the condition of barrels and screws, off-line mechanical measurements are carried out, inducing huge production losses, in particular, for large production extruders. This indicates that sensors capable of monitoring barrel and screw status on-line are in demand for the extrusion industry. The conventional thermocouples and pressure sensors cannot be used for such sensing function.

In order to be useful for NDE of hot objects and on-line monitoring of industrial polymer processes, a monitoring sensor must withstand the required temperatures, often with thermal cycles. For NDE applications, the temperatures for the cooling pipe of nuclear power generation plants and the molten zinc are $< 400^{\circ}\text{C}$ and 450°C , respectively [5,6,7]. Manufacturing processes are usually carried out at elevated temperatures, for example, the nominal temperature at the external mold surface for polymer injection molding is around 50°C [29], while that of the barrel for polymer extrusion could be between 200 and 350°C [30], and that of the die for aluminum and magnesium die-

casting around 350°C [31]. Some applications require much higher temperatures, for example, the temperature of superheated steam is 565°C in aero-engine manufacturing and operation [32]. Further potential applications exist in the automotive sector; sensors are exposed to more than 350°C while measuring automobile exhaust [33]. This clearly indicates that there is a need for HT sensors.

Ultrasonic transducers (UTs) are attractive candidates for on-line process monitoring. Ultrasonic techniques are simple and economical, and can be used nondestructively and non-intrusively. Because of advancements in computer technology industry, fast data acquisition and real-time monitoring has been possible [23,34,35]. It is also well known that one of the main advantages of ultrasound is its ability to propagate in optically opaque materials. It can be used to probe not only the subsurface defects but also the viscoelastic properties of the materials. The material properties, such as viscosity, density, Young's modulus, shear modulus, composition and percentage of fillers in polymers, flow front, solidification, shrinkage, *etc.*, may be probed using reflection coefficients at the interface, e.g. between the steel mold and melt, velocity, attenuation, and scattered signal in the melt through the manufacturing machine [34,35]. Since ultrasound velocity in the melt or steel mold is a function of temperature [23], UTs can be used as temperature sensors. Furthermore, UTs can be used for nondestructive testing of materials, because subsurface defects, voids, *etc.* and their location, size, shape, and distribution may be studied and imaged.

Piezoelectric materials are commonly used in typical UTs because they are low cost, and exhibit high efficiency of generating and receiving ultrasound. As a result, piezoelectric materials have been dominant sources as UTs to generate and receive ultrasound [36]. Several other UTs have been also developed to operate at elevated temperatures, such as electromagnetic acoustic transducer (EMAT) [37-40] and laser ultrasound [41-44]. However, EMATs are generally inefficient in generating and receiving ultrasound so that the signal-to-noise ratio (SNR), defined in this thesis as the ratio of the amplitude of the first echo signal traveling one round trip through the thickness direction, over that of the spurious noise as shown in Figure 1.1 between the

echoes traversing back and forth within the sample, is normally not high enough for practical use such as on-line monitoring of industrial polymer processes. Laser ultrasound can perform fast on-line scanning and probe materials of complex shapes; but currently this technique is expensive, low repetition rate (< 200 Hz), and requires the use of moderate-power lasers to avoid damage [13,34].

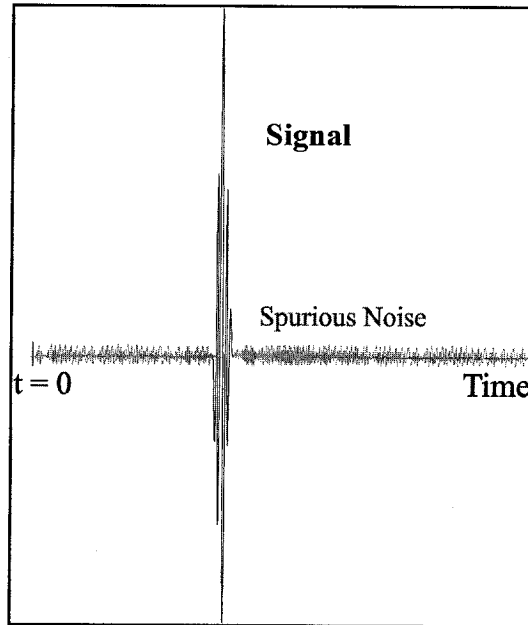


Figure 1.1: Schematic showing a signal and associated noise.

However, development of high temperature ultrasonic transducers (HTUTs) is still a challenging theme, containing many issues to be overcome for real use. One of the major hurdles is the deterioration of the piezoelectricity due to elevated temperatures. The simplest configuration of piezoelectric UTs is a simple disc type and they can be directly attached to the objects for ultrasonic measurements. This arrangement is simple and inexpensive. But if piezoelectric materials are used for high temperature processes, piezoelectric UTs will then have to function at elevated temperatures. Piezoelectricity comes from anti-symmetric structure within unit crystals [36]. For piezoelectric ceramics, strong electric field is applied to produce their piezoelectricity and this operation is called

as poling. At the Curie temperature (T_c), the structure of the unit crystal transits to a structure of higher symmetry; as a result, there is no more piezoelectricity. Once piezoelectricity is lost, it does not recover even below the T_c , unless the materials are subjected to a strong electric field, so that re-poling occurs. In addition, when piezoelectric materials are heated up, their internal kinetic energies increase. As a result, dipoles that are oriented during poling tend to return to random orientation above certain temperature; thus piezoelectricity decreases. This degrading effect is known as “thermally activated aging”. Generally, a recommended maximum operation temperature of UTs is considered as half of the T_c [45]. The most commercially available and high piezoelectric strength piezoelectric ceramic materials are still PZT families, because of their relatively high T_c . The T_c of hard PZTs is around 360°C [36] and it is not sufficient for certain applications. Lithium niobate (LN) single crystals are a well known, high T_c , commercially available piezoelectric material, too. The Curie temperature is around 1150°C [34,45]. According to the assumption of “thermally activated aging”, the maximum recommended operation temperature is approximately 600°C. However, it is also reported that LN is weak in resisting thermal shock [46,47]. Lithium tantalate (LT) has the same unit crystal as that of LN, and the piezoelectric and optical characteristics are almost similar as LN, except for lower T_c such as 620°C [48]. Aluminum nitride (AlN) is another HT piezoelectric material. AlN UT exhibited piezoelectric response up to 1150°C [49]. Unfortunately, not only in the bulk form there is no piezoelectricity, but also during the film fabrication, the selected substrates must be heated up to 1000°C. Because of this high temperature, very few substrates can be used and this makes AlN not practical for the applications mentioned in this thesis. Furthermore it is almost difficult to fabricate a thick enough AlN film to have operation frequency less than 10 MHz for industrial material process monitoring. Since molten polymers and metals have high ultrasonic attenuation, the center frequencies of HTUTs are preferred to be less than 20 MHz. A number of new piezoelectric crystals are reported, such as Langasite ($\text{La}_3\text{Ga}_5\text{SiO}_{14}$), which offered promising piezoelectric behavior up to 900°C. This material is an excellent substrate for surface acoustic wave (SAW) and bulk acoustic wave (BAW) devices [50]. Many companies have started production, so single crystal wafers are commercially available. But this material’s piezoelectricity is too weak to use as a HTUT

for the applications of the interest. Therefore, the choice of piezoelectric materials for HTUTs seems quite limited.

Other hurdles for piezoelectric transducers to operate at high temperature are the couplant between the HTUT and the objects to be tested or monitored, and backing material. Usually liquid couplant exists between the piezoelectric UT and the object to enable efficient ultrasonic transmission. However, the liquid couplant evaporates at elevated temperatures; after certain time, refreshment is required. Therefore it is not ideal for continuous monitoring at elevated temperatures. Dry ceramic powder or refractory adhesive cement can be an alternative HT couplant, and can work at above 300°C [51, 52]. However, the signal strength and SNR become worse because of the porous microstructure of these couplants after drying [53]. As another solid couplant, a thin metal film such as gold or aluminum foil can replace the liquid couplant. In this case, in order to obtain an acceptable ultrasonic transmission, pressure of $>10 \text{ N/mm}^2$ should be applied between the stand-alone UT and the object [54]. For the on-line ultrasonic monitoring, HTUT of broadband frequency spectrum is much preferred. For room temperature UT, backing material is widely used to achieve broadband characteristics. tungsten/epoxy composite has been mainly used as a backing material, because of its high absorbance and good acoustic impedance matching with the piezoelectric ceramics [55]. However, not only most organic material cannot withstand 250°C [56], but also materials and methods cannot survive due to different thermal expansion coefficients of the backing material and metal electrodes for piezoelectric UT. It means that the broadband frequency characteristics will deteriorate during thermal cycling.

Several stand-alone HTUTs are commercially available from Etalon (Lizton, IN), RTD/Panametrics (Waltham, MA), GE/Krautkramer GmbH (Cologne, Germany), RTD (Rotterdam, Netherlands), Ultrat (Boalsburg, PA), Ishikawajima Inspection and Instrumentation Co. Ltd. (Tokyo, Japan), Sigma Transducer Inc. (Kennewick, WA), *etc.* These stand-alone HTUTs can operate at elevated temperatures up to 500°C, but their SNR is not high (normally less than 20 dB) [57]. They can be used to measure the thickness or corroded pipes; however, they are difficult to be applied for on-line

monitoring of the industrial material process, such as polymer extrusion and injection molding, because of their poor SNR. For HT ultrasonic measurements, buffer rods are an easy and effective way to insulate UTs from elevated temperatures. Most commercial HTUTs use buffer rods or delay lines [31,34,57-61]. The combination of buffer rod, room temperature broadband UT, and cooling system, enables us to monitor at elevated temperatures, such as 960°C in liquid aluminum, with good signal strength, high SNR, and broadband [34,59,60]. This design is already being used for on-line monitoring of die casting [31], injection molding [57], and semi-solid metal monitoring [61]. However, the system using buffer rod is bulky because of the cooling system. The size must be taken into account with regard to the placement of the sensors. In addition, the concern of the HT couplant between the HTUT and the buffer rod still exist [57]. If the HTUT can be deposited or glued on the buffer rod, the cooling system could be avoided, or the maximum operating temperature could increase.

1.2- HTUTs for nondestructive testing of metals and real-time industrial material processing monitoring

Development of HTUT for NDE of metals at elevated temperatures and on-line monitoring of industrial polymer processing is highly desired. They are preferred to have maximum operation temperatures between 200-500°C, with broad frequency bandwidth, 2-30 MHz center operation frequency, adequate signal strength, high SNR, no couplant and no cooling system requirement. To develop such HTUTs is one of the main objectives in this thesis. Two directions will be introduced: Sol gel spray HTUTs, and HTUTs permanently bonded onto a metal substrate, such as the delay line or buffer rods.

1.2.1- Sol gel spray HTUTs

The sol gel technique uses chemical thin film fabrication, and it is attractive because of low capital cost and low processing temperature. It has been known for several decades; one of the earliest published works was on silica gel, in 1864 by Graham [62]. Subsequently, oxide coatings were obtained from organic precursors by the sol gel method; organo-metallic precursors of the desired ceramic oxide are mixed and dissolved into an appropriate solvent. The simplest method of preparing the solution is to dissolve metal alkoxides in water/alcohol mixtures. Payne, *et al.* invented a sol gel process for PZT and LN [63]. To improve stability, water-based solutions were pioneered by Yi and Sayer [64], and further developed by Schwartz, *et al.* [65]. The solution is coated onto the substrate by spin, dip, or spray coating, and the coated film is dried to remove the organic material. During the firing process, the organic residues in the film are pyrolyzed and oxidized; thorough crystallization is obtained during annealing. Coating and thermal treatments are multiplied until the film reaches the desired thickness. A perovskite phase, in which PZT exhibits the piezoelectricity, appears above 450°C, even though the PZT ceramics sintering temperature is greater than 1000°C [66]. Each coating adds 0.2 μm [67]; at least 100 μm thickness is required for relatively low MHz center operating frequency, since UTs operate in the thickness mode. This process is time consuming, and

increases capital cost. In addition, the possibility of cracking and peeling increases with the thickness, because of internal stresses during the fabrication process.

A sol gel composite technique was invented by D.A. Barrow, *et al.* to fabricate thick films up to 200 μm [68]; a selected ceramics powder is added to the sol gel solutions. After preparing the composite sol gel solution, the following fabrication process is almost the same as the traditional sol gel method. PZT (ceramic powder)/PZT (sol gel) shows lower dielectric constant and lower piezoelectric charge coefficient than traditional sol gel-derived PZT [67]. Using powder introduces more pores into the film; as a result, the desired thickness for a required frequency decreases because ultrasound velocity is reduced according to porosity. This porosity also increases frequency bandwidth but at the same time, deterioration of piezoelectricity. Furthermore, no couplant is needed because the piezoelectric film is directly attached to the substrate. Such attachments also significantly enhance the frequency bandwidth. In sol gel composite films, the sol gel seems to work as an adhesive material between powder and powder, and powder and substrate; therefore we can say that efficient structures, embedded into or bonded directly onto the host materials, may be realized by this technique, which is suitable for some applications, for example, micro-molding process monitoring or aerospace engineering. Preliminary results of PZT/PZT and LN/LN broadband UTs made by this technique have been demonstrated [69]. Since the sol gel technique is a chemical method, the recipe is not established for many piezoelectric ceramics. Therefore, different combinations of ceramic powder and sol gel solution have been tried [68]. LT/PZT broadband HTUTs have been also demonstrated at 368°C previously [69].

In this thesis, three main advances from previous works have been carried out. First, the coating method is changed from spin to spray coating. In the sol gel technique, HTUTs are fabricated onto the substrate directly; to serve as real-time monitoring HTUTs for industrial material processing, they should be fabricated on the apparatus itself, such as the barrel, die, or insert for polymer processing. In the spin coating method, the substrate must spin at high speed, such as 2000 rpm; therefore, large, heavy and/or

complex shaped substrates are not acceptable. Moreover, it is impossible to fabricate homogeneous films on curved surfaces, such as barrels. By spray coating, the film can be fabricated onto desired substrates, including metal plates, sheets, foils, cylindrical or spherical concave or convex surfaces, and even small balls [70]. This makes sol gel HTUTs more practical for industrial material process monitoring. A drawback of this approach is that porosity may increase, since compressed air is used for spray coating; low pressure is preferable.

The second advancement is that corona discharge poling is used instead of the traditional poling method. Corona discharge is relatively low power electrical discharge, at or near atmospheric pressure. Positive or negative ions are produced by corona discharge, to charge the dielectric film [71]. During corona poling, the piezoelectric film has no top electrode so that there is no dielectric or local breakdown. Therefore corona poling may be a suitable method for poling high T_c materials. Furthermore, large area poling is easier than by traditional poling; thus it is suitable for mass production [72]. As mentioned above, inducing piezoelectricity in ferroelectrics requires that a high electric field is applied to switch the domain wall. Usually PZT is poled in an oil bath, applying a high DC electric field to prevent dielectric breakdown. However, high T_c materials present problems with this method; during the poling, the oil bath is heated up according to the T_c . At high temperatures, the oil is lost by boiling or evaporation, and is no longer useful. Of course poling can be done without an oil bath, but the oil bath helps to prevent dielectric breakdown. With higher temperatures and longer poling time, the possibility of dielectric breakdown increases. Once this occurs, piezoelectricity often deteriorates because of microcracks.

The third main contribution is the change of UT materials. As sol gel materials, PZT and alumina (Al_2O_3) are selected to confirm the influence onto characteristics of the composite material by sol gel phase. In previous sol gel HTUTs, LT was chosen as the piezoelectric powder material, with a T_c of around $620^\circ C$ [69]. If we assume that thermal activated aging is applied to LT, the recommended maximum operation temperature is approximately $300^\circ C$. The piezoelectricity of LT is weaker than LN, and much weaker

than PZT. Thus two different piezoelectric powders are selected, according to the temperature range of the operation. For temperature ranges below 200°C, a soft PZT with T_c of 350°C and high piezoelectricity is selected. Hard PZTs have higher T_c , higher coercive field, lower dielectric constant, and lower piezoelectric charge coefficient than soft PZTs. They are slightly different in chemical composition; at room temperature, soft PZTs are preferable for sensor applications because they have high sensitivity, higher displacement, and lower mechanical quality factor value. Soft PZTs may share some hard PZT characteristics, and *vice versa*. In this thesis a soft PZT with high T_c was selected. For temperature ranges above 250°C, bismuth titanate (BIT, $\text{Bi}_4\text{Ti}_3\text{O}_{12}$), the prototype of a large family of layered ferroelectrics represented by the generic formula $(\text{Bi}_2\text{O}_2)^{2+}(\text{Bi}_2\text{Ti}_3\text{O}_{10})^{2-}$, is selected. This formula indicates that three perovskite-like units of nominal composition BiTiO_3 are separated along the c-axis by $(\text{Bi}_2\text{O}_2)^{2+}$ layers [73], providing T_c of 675°C [74]; a higher operating temperature range comes from high anisotropy, which causes a high coercive field. Its piezoelectric voltage coefficient is suitable for sensor applications. As a result, HTUTs operated up to 500°C are expected using BIT powder.

1.2.2- HTUTs permanently bonded onto metal substrates

In order to increase signal strength, other types of HTUTs is developed using permanent bonding of LN single crystal HTUTs onto metal substrates, such as delay lines or buffer rods. It is difficult to establish good acoustic bonding because any porosity inside the bonding layer can cause signal deterioration by significant increase of ringing effect of UT and many spurious modes [54]. Therefore, an improved bonding is required between HT piezoelectric UTs and buffer rods or substrates. Since bulk piezoelectric UTs are used in such an approach, the piezoelectric strength of the UTs is higher than the thick film UTs made by sol gel method in which porosity exists. Two bonding methods, brazing and diffusion bonding will be investigated.

Brazing involves the well-known technique of high temperature soldering. The brazing material is melted at high temperature, making thin composite layers between the brazing material and the objects to be bonded. Since the objects are not melted, they receive less damage than from welding. Brazing between metal and ceramics is not a new idea [75-77], nor is brazing between metal and piezoelectric crystals [5,78,79]. Generally, successful brazing bonding should provide excellent joints, and acoustic impedance matching should be proper to obtain broadband characteristics without backing material.

Diffusion bonding also provides excellent bonding, with operation temperatures lower than brazing; this approach had been attempted before [5,80-83]. In this method, thin metal or alloy film is fabricated onto both surfaces to be joined; then high pressure and relatively low temperature are applied. By co-diffusion or self-diffusion, bonding is accomplished. In the context of this thesis, indium cannot be used because of its low melting temperature, even though its diffusion coefficient is high and it is utilized in many diffusion bonding cases [80,81]. Therefore, aluminum and/or gold is selected for ease of diffusion bonding, because they are soft metals, with high enough melting temperature for the interests in this thesis. In the case of buffer rods, even monitoring for molten metal, the temperature seems not to exceed aluminum's melting point (660°C). Vacuum conditions are preferable during bonding process to prevent oxidation [82,83]. In reference [5], brazing and diffusion bonding was attempted, and the signal had a long trailing echo indicated narrow frequency bandwidth, thus broadband improvement is needed.

1.3- Thesis content

This thesis focuses on developing HTUTs and the application of these HTUTs for nondestructive testing of metals and real-time monitoring of several industrial material processes at elevated temperatures.

Chapter 2 explains the sol gel spray film fabrication. Detailed fabrication processes, such as piezoelectric powder selection for high temperature use, sol gel preparation, surface treatment of the substrate to increase adhesion, ball-milling, spray coating, thermal treatments, the poling process including attempted optimization of poling parameters, and top electrode fabrication are explained. Poling conditions and film color changes during corona poling are discussed. Thermal cycling results are also presented for the demonstration of the durability of these films as HTUTs.

In Chapter 3, characterization of sol gel sprayed thin film is carried out. Important parameters for UTs such as stiffness compliance, dielectric constant, piezoelectric constant and electromechanical coupling coefficient are introduced. And then the measurement methods of those parameters for composite films on substrates are explained. Resonant frequency method is introduced to measure thickness mode electrical coupling factor k_t , one of the important factors for UT, in addition to density and velocity measurement, are explained. The dielectric constant calculation for sol gel composite films is demonstrated by averaged calculation method with cube model and confirms the effectiveness by comparison with experimental values. The film characteristics and ultrasonic signals in time and frequency domain derived from several films and obtained at room temperature and elevated temperatures are demonstrated.

Chapter 4 demonstrates the use of these thick piezoelectric films for the realization of nondestructive testing of metallic structures at high temperature use. These films may be embedded into or bonded directly onto the host materials so that they can be employed as ultrasonic sensors and actuators effectively. The sol gel spray technique can directly fabricate thick films onto various substrates and shapes, such as steel, stainless

steel, titanium, nickel and copper substrates, with planer, spherical concave and convex, and cylindrically concave and convex surfaces and thin sheets or foils. The ultrasonic performances of several substrates and shapes are demonstrated at elevated temperature. Immersion type BIT/PZT HTUTs are developed and demonstrated for thickness measurements inside the molten zinc at 450°C and ultrasonic front and subsurface imaging in silicone oil at 200°C.

Chapter 5 shows several industrial applications of sol gel composite sprayed HTUTs, such as real time on-line monitoring of polymer extrusion, injection molding and micro-molding. For polymer extrusion, LT/PZT and BIT/PZT HTUTs are fabricated on the surface of a barrel adapter of a polymer extrusion machine at the pumping zone. Real-time monitoring at around 200°C is demonstrated to obtain ultrasonic signals from the barrel and the screw, to monitor barrel wear and screw status. For injection molding, BIT/PZT and PZT/PZT HTUTs are fabricated onto the mold insert of injection molding machine. Real-time monitoring at elevated temperature is carried out. Ultrasonic monitoring of the filling completion is presented. For micro-molding, BIT/PZT HTUTs are fabricated onto the mold insert and the cylindrical barrel of a micro-molding machine, to monitor the entire process. Their capability and real-time monitoring at elevated temperature are discussed.

In Chapter 6, brazing bonding and diffusion bonding are examined for permanent bonding between LN crystal and metal substrates. Signal behavior in time and frequency domains at elevated temperatures is presented. Difficulties and possibilities of these techniques are discussed.

Finally, Chapter 7 presents the summary and claims of originality of the thesis.

Chapter 2

Sol gel spray coating technique

2.1- Introduction

In order to operate a piezoelectric film UT via thickness mode in a low (2-30) MHz range for applications of the interest, film thickness must be thicker than 10 μm . Various methods to fabricate thick piezoelectric films include tape casting [84], screen printing [85,86], jet printing [87] and hydrothermal [88] approaches have been reported. Tape casting can fabricate films over a wide thickness range, from 0.02 to 3.0 mm. However, this technique is not suitable for large or curved substrate surfaces, since 14-35 MPa pressure must be applied [84] to stack and laminate the film on the substrate. In addition, the firing temperature requirement is greater than 1000°C, for example, 1265°C, which would modify the microstructure of steel substrates of the interest. Screen printing and jet printing also need high temperature for example, 1450°C [85] and 900°C [87] during firing process. These techniques are suitable for making films with complicated microstructure, but only on planar surfaces. In addition, there is also a scale-up concern [85,86]. The hydrothermal method is based on material synthesis and crystal growth in water under high temperature and pressure [88]. Selective and homogeneous epitaxial growth of PZT film is possible even on curved surfaces. The processing temperature (140-160°C) is lower than that of sol gel technique. However, films can be fabricated only on titanium (Ti) surfaces, since this approach employs a chemical reaction between the Ti surface and the solution. Thus Ti must be evaporated or sputter-deposited on the substrate, unless the substrate itself is made of Ti. Therefore, this approach is not suitable for large substrates in big apparatus. None of these techniques has been used to fabricate HTUT for nondestructive testing of materials and on-line ultrasonic monitoring of industrial material processes at elevated temperatures as mentioned in Introduction.

In previous works, the sol gel technique to fabricate thin film [62-67] was modified by D. Barrow, *et al.* to increase film thickness to 200 μm [68]. In a modified sol gel composite technique, piezoelectric powders were incorporated with sol gel, serving as adhesion materials among powders, and between powder and substrate. As a fabrication technique, spin coating, dip coating, or spray coating are all possible [68]. Therefore, LT/PZT broadband HTUTs were fabricated directly on stainless steel or aluminum plates by spin coating, and broadband HTUTs were realized without ultrasonic couplant or backing material [70]. This feature is useful for continuous ultrasonic measurements at elevated temperatures. This also suggests that ultrasonic sensors integrated into host materials and structures may be realized.

In this thesis, a sol gel technique with spray coating is selected so that curved surface substrates can be realized by the developed technique. Many industrial machines have curved surfaces, such as barrels for injection molding and micro-molding, and heavy and large parts which cannot be put on the spinner; therefore selecting a spray coating technique is useful for monitoring industrial material processes. Corona poling is selected instead of traditional poling, due to the ease of poling high T_c materials with relatively large areas. Because the developed techniques are simple, they may provide cost-effective HTUTs. In this chapter, the detailed fabrication process of spray coating sol gel composite technique is explained.

2.2- Fabrication process

The sol gel spray coating technique can fabricate thick piezoelectric films on various substrates with different shapes. The detailed fabrication processes such as piezoelectric powder selection, sol gel preparation, ball milling, substrate preparation, spray coating, thermal treatment, poling, and top electrode fabrication are explained below. The schematic of the general fabrication process is shown in Figure 2.1.

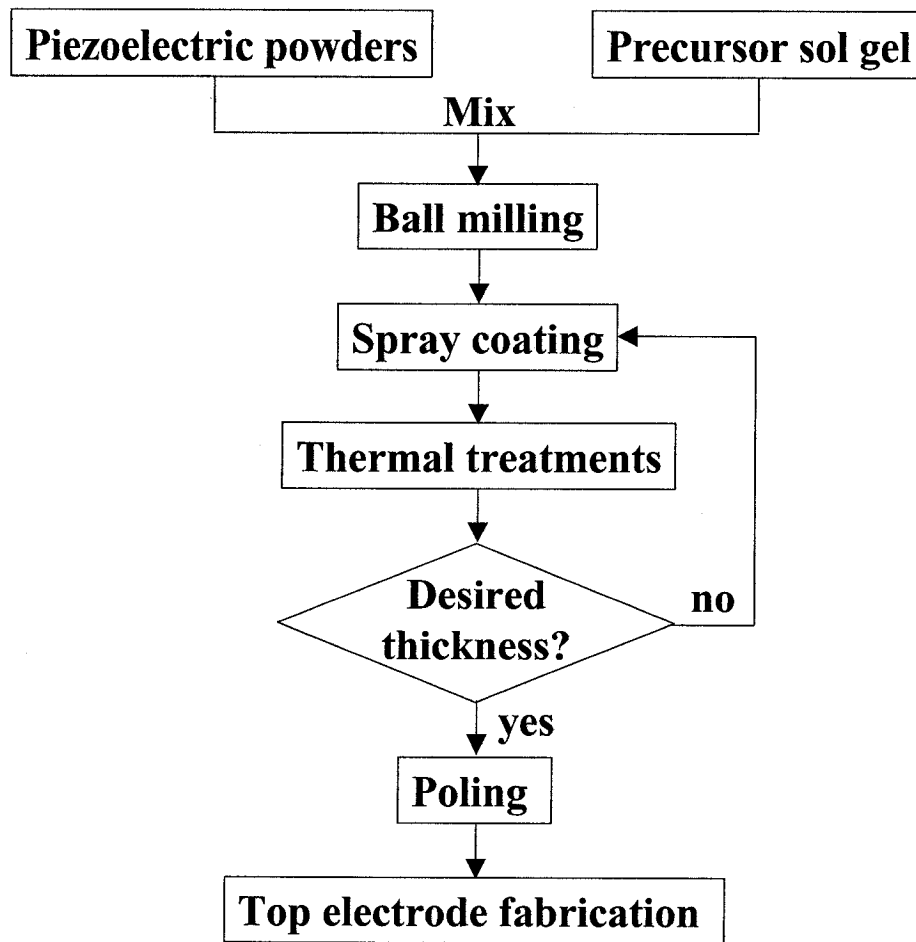


Figure 2.1 Flowchart of fabrication process by sol gel spray coating technique.

2.2.1- Powder selection

In a sol gel composite technique, the volume concentration of piezoelectric powder in the precursor sol gel after annealing is normally between 65-80 %, in order to achieve 10 μm film thickness build-up per spray coating, and acceptable film quality. If the powder concentration is too low, the attainable thickness decreases due to high stress and the objective of modifying the sol gel technique to obtain a thick film may not be satisfied. If the powder concentration is too high, the film will have too many pores, and composite film quality deteriorates [89].

To serve as a thick film HTUT, the used piezoelectric powder must have a high Curie temperature (T_c), since most piezoelectric materials can operate up to half of their T_c due to thermal aging effects. In this thesis, three materials are chosen as piezoelectric powders: PZT, LT, and BIT.

PZT

As mentioned in Chapter 1, PZT [$\text{Pb}(\text{Zr}, \text{Ti})\text{O}_3$ solid solution] was developed in Japan in the early 1950's [90]; even now this material is widely used because of its superior properties, although it includes lead, which is becoming restricted in usage due to environmental contamination concerns. Materials with higher piezoelectric coefficients than PZT, such as lead magnesium niobate / lead titanate (PMN-PT) and lead zirconate niobate / lead titanate (PZN-PT), are composite materials with electrostrictive material, for which strain varies quadratically with electric field rather than linearly as for piezoelectric material. PZN is very sensitive to temperature changes. PT is added to improve temperature stability, but PZT is still superior in temperature stability. PZT has high piezoelectricity and excellent temperature stability below 100°C , and low material cost, so that it is still a dominant material for UTs.

The phase diagram of PZT is shown in Figure 2.2 [90]. At the morphotropic boundary [91] between tetragonal (F_T) and rhombohedral structure (F_R), PZT performance is almost temperature-independent, and its dielectric constant ϵ and electromechanical coupling factor k becomes peak, as shown in Figure 2.3. Therefore, generally PZT UTs use this mol concentration, for high piezoelectricity and excellent temperature stability. Unit cells of PZT are shown in Figure 2.4. PZT has a typical perovskite structure: below T_c , the unit cell is tetragonal or rhombohedral in structure; the anti-symmetry for poled PZT below T_c as shown in Figure 2.4 (b) of Ti or Zr, causes piezoelectricity. Above T_c , the unit cell becomes cubic, with no piezoelectricity. Remarkably, the deterioration of piezoelectricity starts far below T_c , because of thermally activated aging. Pure PZT is rarely utilized. Commercially available PZT powder usually includes some dopants to improve characteristics; the type of dopant divides the mixture into soft and hard PZTs. In soft PZTs, a small amount of a donor dopant is added to the

PZT; soft PZTs are characterized by high piezoelectric and dielectric constants, large electromechanical coupling coefficient, high electrical resistance, low coercive field, and low T_c , below 300°C. In hard PZTs, a small amount of acceptor dopant is added; generally, hard PZTs have characteristics opposite to those of soft PZTs, such as low piezoelectric and dielectric constants, small electromechanical coupling coefficient, low electrical resistance, high coercive field, and high T_c , above 300°C. Therefore hard PZTs may be chosen for HTUT applications, due to the higher T_c . However, exceptions do exist, for example, even in hard PZTs the maximum T_c is around 360°C. Therefore PZT application to industrial material processing is temperature-limited. In addition, some soft PZTs exhibit characteristics of hard PZTs, and *vice versa*. Thus, powders should be chosen carefully, comparing specific characteristics. In this thesis a PZT, PKI-502 from Piezo Kinetics Inc., is selected due to its high T_c , which realizes high operating temperature. Table 2.1 shows the properties of the PZT powder selected in this thesis.

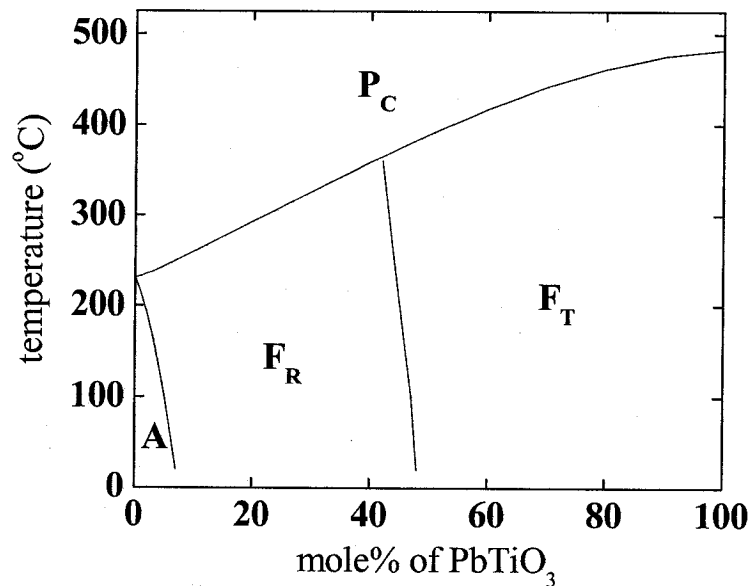


Figure 2.2 Phase diagram of PZT solid solution. P_C: paraelectric cubic, A: antiferroelectric, F_R: ferroelectric, rhombohedral, F_T: ferroelectric, tetragonal.

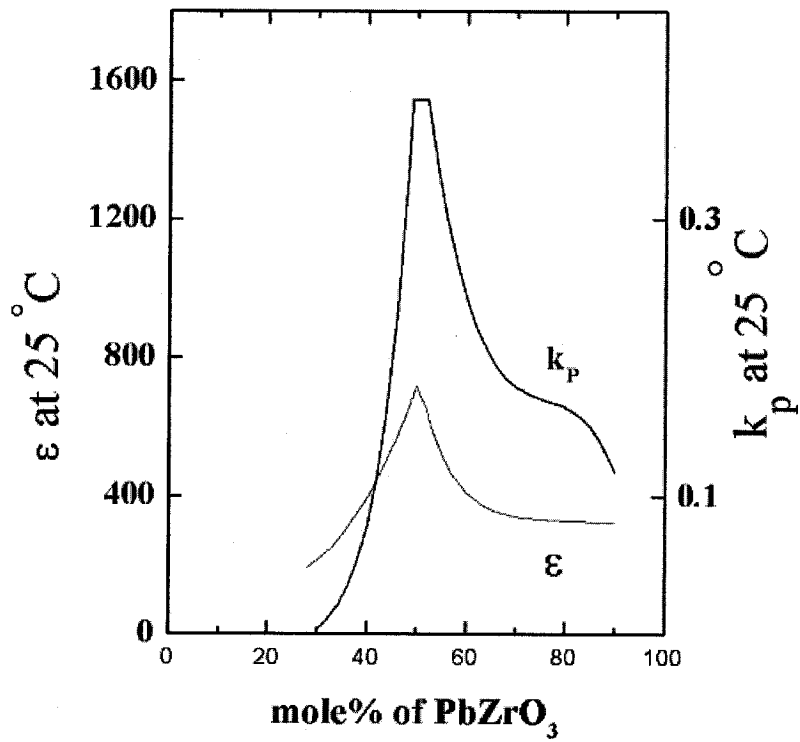


Figure 2.3 Dielectric constant ϵ and planar electromechanical coupling factor k_p versus composition of PZT [90].

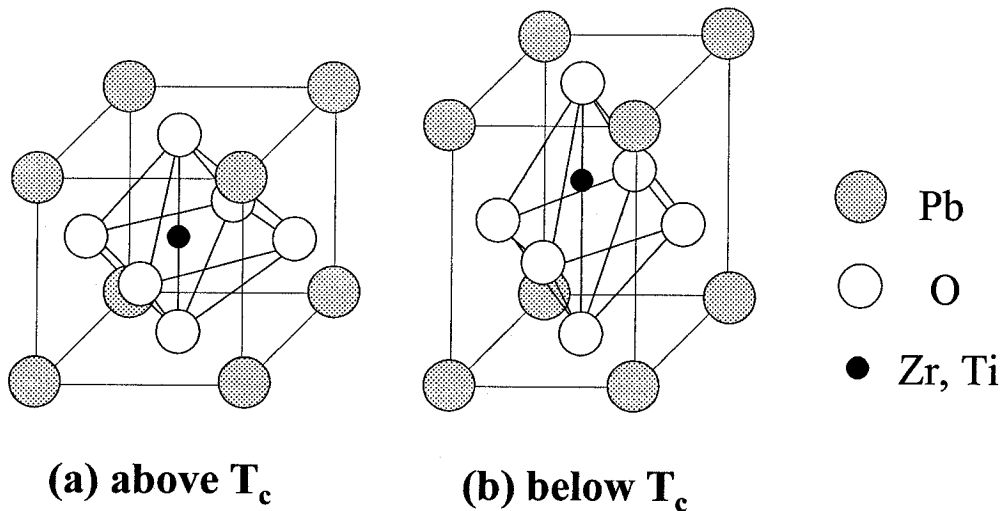


Figure 2.4 Crystal lattice distortion and ion shifts a) PZT above Curie temperature, b) poled PZT below Curie temperature.

Table 2.1 Electrical, mechanical, and electromechanical properties of PZT powder provided by Piezo Kinetics Inc.

Density ($\times 10^3 \text{ kg/m}^3$)	7.7
T_c ($^\circ\text{C}$)	350
Mechanical quality factor Q_M	80
Maximum operating temperature ($^\circ\text{C}$)	150
Dielectric constant at 1 kHz	1800
Planar coupling factor k_p	0.60
Longitudinal coupling factor k_{33}	0.69
Longitudinal charge coefficient d_{31} ($\times 10^{-12} \text{ m/V}$)	-175
Longitudinal charge coefficient d_{33} ($\times 10^{-12} \text{ m/V}$)	400
Longitudinal charge coefficient g_{33} ($\times 10^{-3} \text{ V}\cdot\text{m/N}$)	25.1
Young's modulus ($\times 10^{10} \text{ N/m}^2$)	7.1
Poisson's ratio	0.31
Elastic compliance s_{11}^E ($\times 10^{-12} \text{ m}^2/\text{N}$)	15.4
Elastic compliance s_{33}^E ($\times 10^{-12} \text{ m}^2/\text{N}$)	18.4

LiTaO₃ (LT)

LT and LN exhibit many characteristics, such as electro-optical, piezoelectric, pyroelectric, and non-linear optical properties, and low thermal expansion, used in surface acoustic wave (SAW) and optical devices. LT and LN were developed in the 1960's [92]. LT and LN have unique ilmenite-like corundum structures. The main difference between LT and LN is the values of T_c , about 600 and 1150 $^\circ\text{C}$, respectively. In addition, LT has a lower piezoelectric constant than LN. Since the powders are used in ceramic forms by the sol gel spray technique, poling must proceed at elevated temperatures according to T_c . LT was chosen here because its T_c is 600 $^\circ\text{C}$ at which the steel and aluminum substrates of the interests will not have phase transformation. Poling at the slightly lower temperature is practical for the fabrication on metal substrates of interest. LT powders were purchased from Superconductive Components Inc. General properties of LT and LN are shown in Table 2.2.

Table 2.2 Basic properties of LT and LN

Material	LT	LN
Density ($\times 10^3$ kg/m ³)	7.46	4.64
T _c (°C)	607	1140
Dielectric constant at 1 kHz	44.5	29.5
Longitudinal charge coefficient d_{33} ($\times 10^{-12}$ m/V)	8	19
Longitudinal charge coefficient g_{33} ($\times 10^{-3}$ V·m/N)	20	73
Elastic compliance s_{11}^E ($\times 10^{-12}$ m ² /N)	4.29	4.90
Elastic compliance s_{33}^E ($\times 10^{-12}$ m ² /N)	3.61	4.07

BIT

BIT is the prototype layered ferroelectric discovered in 1949 [93], a typical ferroelectric material with potential for piezoelectric, optical memory, and electro-optic devices because of its relatively low coercive field, high dielectric constant, high T_c of 650 °C, and high mechanical breakdown strength [94-96]. The crystal structure is shown in Figure 2.5. The unit cell consists of three perovskite-like units, nominally composed of BiTiO₃, an oxygen-rich layer, and Bi₂O₂. Above T_c, BIT has a non-polar tetragonal structure. Below T_c, a Ti ion shift causes transformation to a polar structure like PZT, a typical perovskite material [73,74]. Its properties are shown in Table 2.3. Because of the high degree of center anti-symmetry, it does not follow the general assumption that a piezoelectric material should not be used above half of its T_c, to prevent thermal activated aging [45]. Therefore its suitable operating temperature is expected to be 450°C or even higher for temporally operation. BIT powders were purchased from Lorad Chemical Corporation, FL, USA. This thesis had investigated and used this abnormal but novel characteristic and developed BIT as HTUT materials. It becomes one of the major contributions to this thesis research.

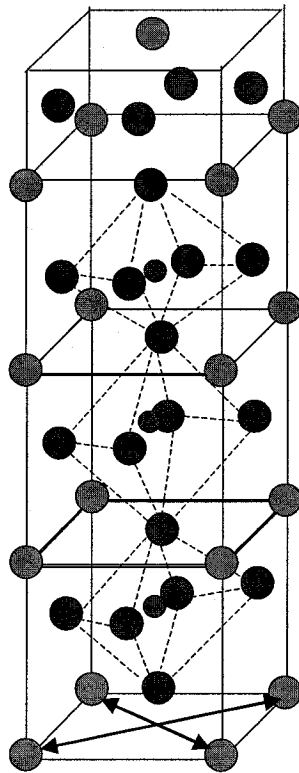


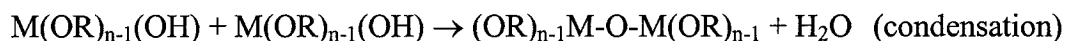
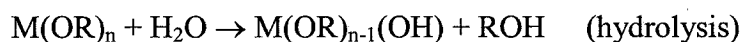
Figure 2.5 Crystal lattice of BIT above Curie temperature.

Table 2.3 Electrical, mechanical, and electromechanical properties of BIT powders.

Density ($\times 10^3 \text{ kg/m}^3$)	6.55
T_C ($^\circ\text{C}$)	650
Mechanical quality factor Q_M	>600
Maximum operating temperature ($^\circ\text{C}$)	550
Dielectric constant at 1 kHz	120
Planar coupling factor k_p	0.03
Longitudinal coupling factor k_{33}	0.09
Longitudinal charge coefficient d_{31} ($\times 10^{-12} \text{ m/V}$)	-2
Longitudinal charge coefficient d_{33} ($\times 10^{-12} \text{ m/V}$)	18
Longitudinal charge coefficient g_{33} ($\times 10^{-3} \text{ V}\cdot\text{m/N}$)	17

2.2.2- Sol gel preparation

The sol gel technique is a chemical fabrication method for thin film fabrication. A solution transforms to a gel by hydrolysis and condensation reactions, expressed as follows:



where R is an alkyl radical and M is a metal. Parameters affecting the gelation and the transition from a solution into a solid include solvent, temperature, pH value, amount of water, mixing order and method, *etc.* [66] In order to maintain film quality, the solution should be stable before thermal processing. Most parameters are established empirically; therefore the recipe for the sol gel is crucial. In this thesis, three kinds of sol gel are used, Al₂O₃, PZT and BIT. However, the Al₂O₃ sol gel recipe is a propriety method belong to Queen's University which cannot be published yet, so PZT and BIT sol gel are explained here.

As mentioned before, Payne, *et al.* invented a sol gel process for PZT [63]. Most PZT sol gel recipes employ lead salt, zirconium and titanium alkoxide precursors. To improve stability, water-based solutions were invented by Yi and Sayer of Queen's University, Kingston, Canada [64], and further developed by Schwartz, *et al.* [65] The preliminary recipe used in this thesis was developed by Queen's University researchers [67], based on the recipe by Schwartz [65]. The process sequence is shown in Figure 2.6 [67]. The main difference between the recipe in [67] and that in [65] is the use of metal alkoxide precursors, zirconium butoxide (80 wt % in 2-butanol) and titanium butoxide, to promote solution stability in [67]. Besides, methanol was utilized as a solvent. Also acetic acid was used to control the hydrolysis and condensation reactions of the metal alkoxide precursors, to improve stability. In this thesis, the procedures to make PZT sol gel followed those given in [67] in general, however, the recipe has been slightly altered such

as the ratio of zirconium butoxide over titanium butoxide to improve electromechanical coupling factor according to Figure 2.3.

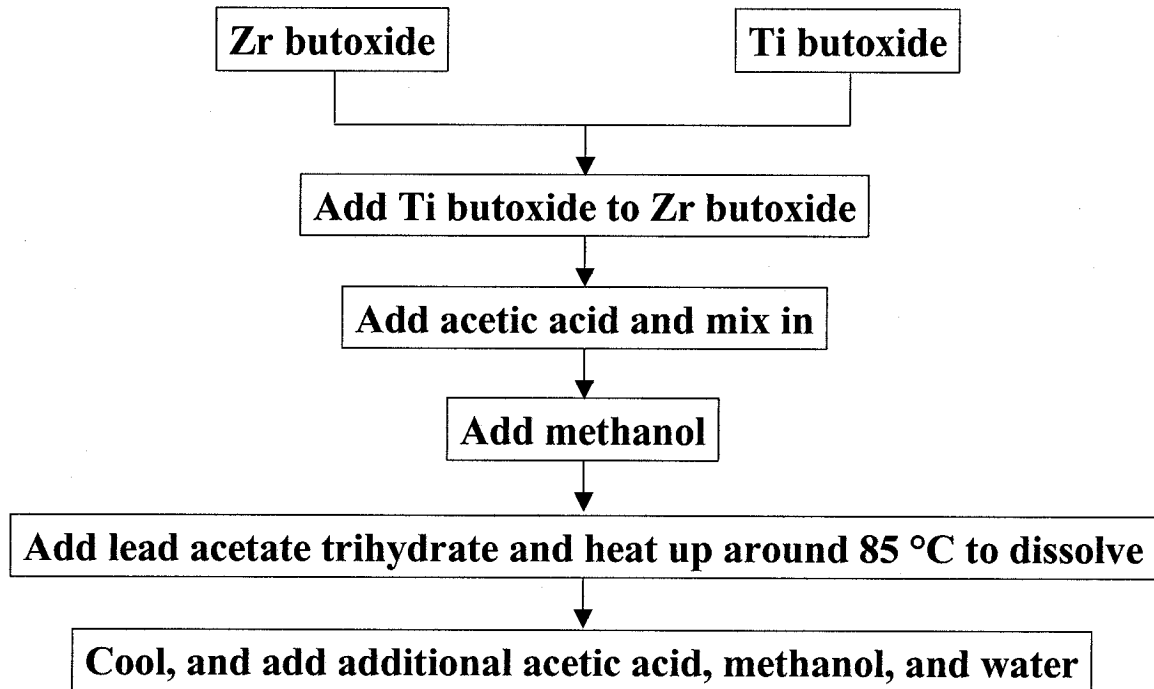


Figure 2.6 Process sequence for PZT sol gel developed by Queen’s University [67].

Sol gel derived BIT films were first reported in 1991 [97]. Since then, there had been several reports concerning BIT thin film by sol gel technique [73,74,95,97-99]. BIT is of interest because it does not contain Pb which is unfriendly to environment. In this thesis, the preliminary recipe was based on reference [74]. Bismuth nitrate pentahydrate, $\text{Bi}(\text{NO}_3)_3 \cdot 5\text{H}_2\text{O}$ was dissolved in acetic acid. Then it was mixed with titanium isopropoxide, $\text{Ti}(\text{OC}_3\text{H}_7)_4$. Finally water was added for hydrolysis. However, the bismuth precursor reacts easily with H_2O to yield white precipitate BiONO_3 hence the solution is unstable and decomposes within a short time [99]. Modification of the recipe is required for improving the stability.

2.2.3- Ball milling

Piezoelectric powders are dispersed uniformly in precursor sol gel to ensure a homogeneous thick composite film. In this thesis, ball milling is used as the mixing method; in previous research, ultrasonic mixing was used [67-69, 89]. However, the film fabrication process of sol gel spray technique requires several days, because of the multiple coatings and thermal treatments. In our experience, ball milling is more preferable for long period usage. In addition, it is difficult to purchase ceramic powders with fine particle size. For example, the particle size of the BIT powder provided by Lorad Chemical Corporation is 200 mesh, meaning that particle size is about 80 μm . This is too large for our purpose, and we have to make the powder finer. Ball milling was used, because it can perform mixing and milling simultaneously. Two main reasons explain why small particle size is preferable: improving both the stability of the composite solution and piezoelectric properties.

The stability rate of the sol gel composite is estimated by Stoke's Law [100],

$$v_p = \frac{2}{9} \frac{r^2}{\eta} g (\rho_{liquid} - \rho_{air}) \quad (2.1)$$

where r is the radius of the powder, v_p is the velocity of the particles through the solution, η is the viscosity of the solution, ρ_{liquid} and ρ_{air} are the density of the liquid and air respectively, and g is the gravitational constant. Assuming that the density of the PZT sol gel is constant, Eq. 2.1 reduces to

$$v_p \approx 2000 \frac{r^2}{\eta} \quad (2.2)$$

The sol gel composite should be stable enough so that the powders can be homogeneously incorporated during spray coating. Therefore the value of v_p should be on the order of 1 $\mu\text{m/s}$ or less, for adequate stability. Assuming that the viscosity of the solution is around 10 cps, r should be less than 1 μm . Since the viscosity of Al_2O_3 sol gel is higher than that of PZT, it can tolerate slightly larger particle size than PZT.

Particle size can influence film properties significantly. Up to a certain limit, smaller grains have higher piezoelectric charge constant d_{33} and higher remnant polarization [101,102]. The main reason may be excessive internal stress in the film due to domain shift or phase transition during poling. In large grain-size specimens, micro cracking occurs during poling under too strong electric fields because not only 180° domain shift but also 90° domain shift may occur [103]. When the grain size is smaller, below the limit point, because of phase transition the piezoelectric properties decrease. Therefore the appropriate particle size is in the range between sub-micron and a few microns, and ball milling is a suitable method to obtain such size.

The appropriate ratio of sol gel to powders, determined by desired film quality and thickness [89], is incorporated and the ball-milling process is carried out. The length of time required for ball milling depends on the desired particle size of the powder; generally speaking, it takes several days.

2.2.4- Substrate preparation

Adhesion between the substrate and the film is important. Since composite ceramic film has a different coefficient of thermal expansion than metal substrates, adhesion must be strong enough so that HTUTs can endure many thermal cycles during monitoring industrial material processes. The mechanism of adhesion is normally composite reactions, and in most cases we do not know the precise details. Adhesion is mainly divided into three mechanisms: mechanical, physical, and chemical bonding. The anchor effect is a typical mechanical bonding. Dominant chemical bonding mechanisms are van der Waals force and hydrogen bonding, between molecules or atoms of the substrate and the film.

Surface treatments are available to enhance adhesion strength. Careful cleaning of the substrate must be taken into account. Substrates of the interest in this thesis are metal. Their surfaces include oil since during manufacturing which is used for lubricating and

cooling. Oil contamination can interrupt the anchor effect, molecular bonding, and chemical reactions, and moreover deteriorates film quality due to incorporation of impurities. However, it is relatively difficult to remove the oil only by chemicals. Acetone is not strong enough to remove the oil completely. Trichloroethylene is an excellent chemical liquid for degreasing, but because of its toxic and long-term residual effects on the environment, its usage is restricted recently. High temperature treatment is simple and effective, but provides further contamination without appropriate cleaning before the process. Sandpaper or sand brushing are effective means to strengthen the anchor effect and van der Waals force. It should be noted that inadequate amounts of sol gel cause air gaps between substrate and film, resulting in deterioration of adhesion. After sandpaper or sand brushing, careful cleaning should be done to avoid contamination through this process. Surface oxidation is effective for the sol gel technique, because the main adhesion mechanism can be explained by chemical bonding, the chemical reactions of M-OH groups on the substrate surface with M-OR groups of sol gel, as shown in Figure 2.7 [66].

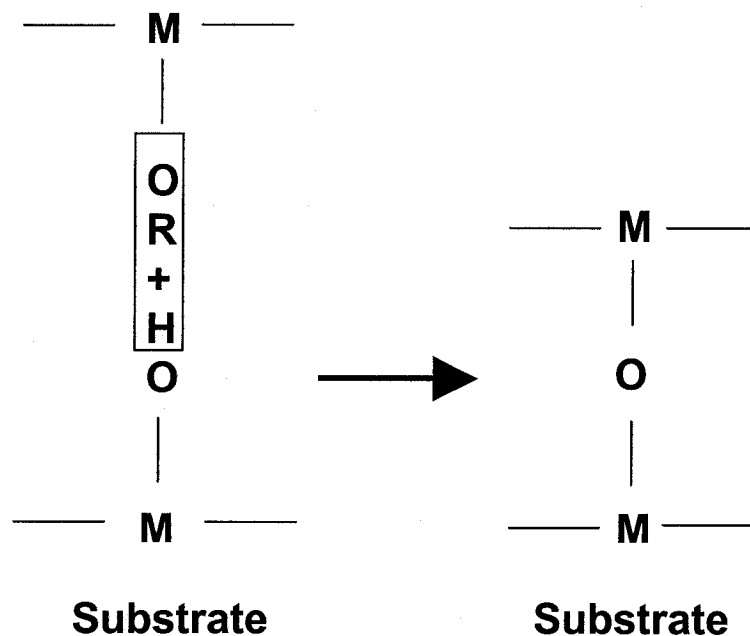


Figure 2.7 Chemical reaction of metal oxide film to a substrate [66].

The detailed substrate preparation process used in this thesis is explained as follows: the substrate is first cleaned by scouring, followed by ultrasonic cleaning with acetone and methanol. Then the substrate is put into the furnace at 650°C for 10 minutes. The oxidized oil layer is removed by polishing with sandpaper. Finally, another scouring and ultrasonic cleaning with acetone and methanol are employed. This cleaning process must be performed just before spray coating.

2.2.5- Spray coating

Spray coating is superior to spin coating in terms of flexibility of substrates in regard to the size, shape and weight. Film fabrication is possible onto a variety of substrate shapes, such as concave or convex cylindrical or spherical surfaces, shown later in Chapter 4. Moreover, it is easy to fabricate films onto substrates difficult to spin, such as large and heavy materials. This change is useful since most apparatus for industrial material processing uses heavy parts with curved surfaces, such as steel barrels of extrusion machines. Spray coating provides more pores in the film than spin coating, resulting in broadband characteristics for UTs, but also reduced piezoelectric strength. In this method, well-mixed composite sol gel is sprayed onto the substrate surface using an air gun, as shown in Figure 2.8. A simple masking method is effective to fabricate films only in selected areas. Even paper tape can be the mask materials. Significant parameters affecting film characteristics include air pressure, distance from the air gun to the substrate, the moving speed of the air gun, coating angle, and coating times. Each spray coating provides 10-15 μm thickness because of the efficiency and internal stress during heat treatment. By multiple coating, film thickness can range to about 40-200 μm .

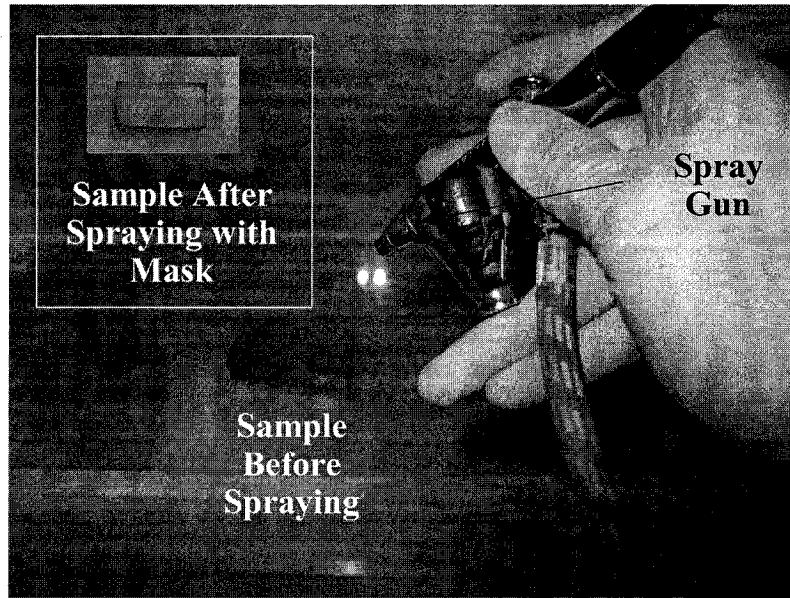


Figure 2.8 Setup of sol gel spraying.

2.2.6- Heat treatment

Heat treatment is crucial for sol gel to obtain high dielectric constants, because the dielectric constant of sol gel affects the piezoelectricity of the composite film, as discussed in Chapter 3. For crystallization, the sol gel approach requires lower sintering temperature than bulk ceramics, and avoids the microstructure change of the substrates. For example, steel undergoes changes its microstructure above 700°C. In this thesis, heat treatment is divided into three steps: drying, firing and annealing. Detailed heat treatment for PZT sol gel is described here. During drying, the sample is heated up to around 90°C to evaporate water and solvent inside the sol gel. Firing is carried out at around 430°C to pyrolyze and oxidize organic residues, and to transform the sol gel to amorphous PZT by polycondensation reactions forming $\equiv\text{M-O-M}\equiv$ linkages. Annealing is done at around 650°C for the film to crystallize [66]. During each step, shrinkage in the sol gel induces internal stress; this is the main reason for cracking and peeling during thermal treatment. The modified sol gel process succeeds in increasing film thickness, since powder does not

shrink so much under sol gel heat treatment conditions, thus relaxing internal stress. Simultaneously, the modified sol gel process produces more pores in the film than the traditional sol gel process without piezoelectric powder; therefore this process is capable of producing low frequency and broadband UTs, but with a reduced piezoelectric strength. However, internal stress remains a subtle problem in producing films thicker than 200 μm . All three steps are conducted after each spray coating, in order to decrease internal stress and improve yield rate, even though complete firing and annealing can be accomplished in one cycle.

2.2.7- Poling

Poling is the process of inducing remanence polarization by applying an electric field exceeding its coercive field to a multidomain ferroelectric material. Spontaneous polarization, P , *versus* electric field, E , during the poling process is illustrated in Figure 2.9 [104]. As E increases, domain wall switching occurs with respect to the electric field direction. When no further domain wall switching occurs, the P *versus* E response usually becomes linear. When E is removed, P remains; this value is defined as remanence polarization, P_R . The coercive field E_c generally becomes minimum value near T_c . In common poling practice, the sample is poled near T_c for a certain time with an applied electric field. However, under high temperature, high electric field, or long poling time conditions, piezoelectricity decreases due to slow crack growth along grain boundaries [103].

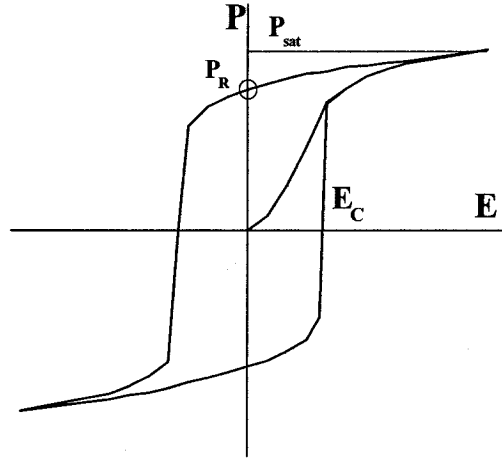


Figure 2.9 Spontaneous polarization *versus* electric field [104].

Usually PZT ceramics are poled by applying a large DC electric field in an oil bath, to prevent breakdown [72]. However, the oil bath can induce contamination, especially to a porous film produced by the spray sol gel technique. It is also not applicable for poling materials with T_c higher than 300°C which is above the boiling temperature of oil. Moreover, since both sides of the piezoelectric film need to have electrodes to form UT, poling may be limited to a small area. Often local breakdown occurs at weak spots, which interrupts effective poling. Poling conditions of around $E = 7\text{-}9 \text{ V}/\mu\text{m}$ at 380°C [29] showed the best result for LT (powder)/PZT (sol gel), but poling at higher E was disturbed by dielectric breakdown, which occurs often even under these conditions. It is difficult to pole PZT/ Al_2O_3 , because the electric field concentrates not into the PZT powder but rather into the lower dielectric constant material, Al_2O_3 , requiring a larger E to pole PZT/ Al_2O_3 [72]. However, only a smaller $E = 3\text{-}5 \text{ V}/\mu\text{m}$ at 160°C , could be applied to PZT/ Al_2O_3 , because of the easy breakdown Al_2O_3 sol gel phase. Once dielectric breakdown happens, it deteriorates the piezoelectricity due to microcracks. The difference between successful and failure poling due to dielectric breakdown is shown in Figures 2.10 and 2.11, obtained by monitoring during the real poling process. When capacitance is charged, current becomes almost zero. Before dielectric breakdown, rapid increase of the current was confirmed. Therefore, during the

traditional poling process, measuring current is a suitable method for evaluating the poling process.

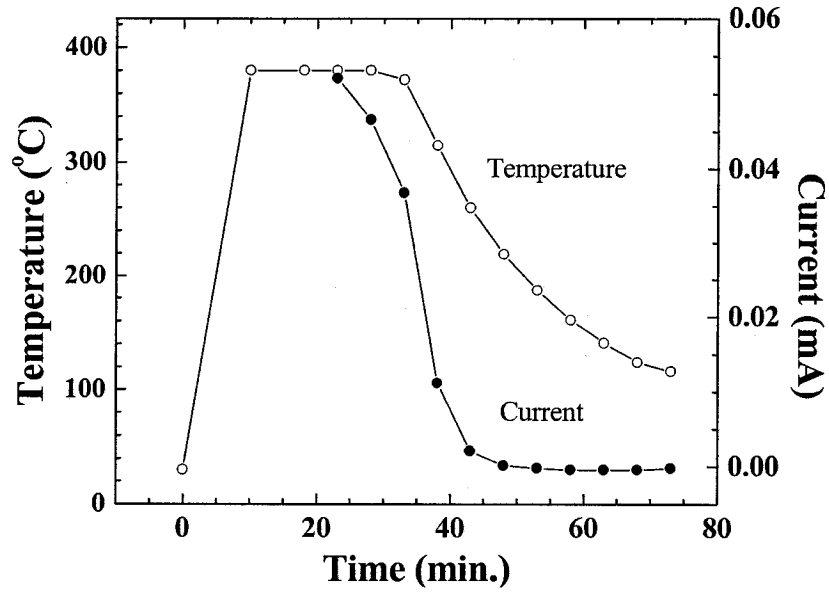


Figure 2.10 Temperature and current transition during successful traditional poling for LT/PZT.

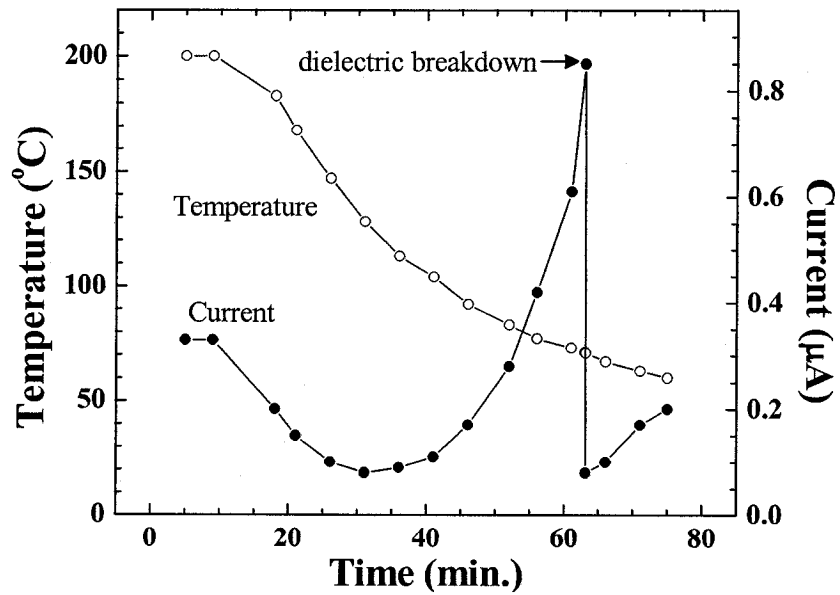


Figure 2.11 Temperature and current transition during traditional poling with dielectric breakdown for PZT/Al₂O₃.

In this thesis, the corona discharge technique was selected [23]. The experimental arrangement for corona poling is shown in Figure 2.12. High DC positive voltage is applied to the needle which acts as a field intensifier, since corona is generated by strong electric fields associated with small diameter wires, needles, or sharp edges on an electrode. Several kinds of corona discharges exist, depending on the polarity of the electric field and the geometry of the electrode. For positive corona in the needle-plane electrode configuration, burst pulse, streamer and glow coronas and spark discharge appear as the applied voltage increases. In our setup, glow corona is observed in almost all cases, as shown in Figure 2.13. Variance in DC and AC components of 0.34 A and 0.02 A, respectively, was observed during corona poling because the streamer is repetitive. The length of the plasma zone of the corona is only a few millimeters, except that streamer corona and spark discharge occur. Outside this region, positive ions produced by electron impacts in the plasma are transported to the grounded electrode by the electric field [71]. The dielectric film is coated on a grounded metal plate, so that the corona discharge from the needle is sprayed onto the top surface of the film and creates an electric field in it. Because one surface of the film has no electrode, there can be no shorting at weak spots. Furthermore, corona poling may be applied to pole large and curved areas.

Corona poling was attempted for PZT/PZT, BIT/PZT, Al₂O₃/PZT, LT/PZT, and BIT/BIT. Optimization of corona poling conditions for each composite film was studied. Parameters for corona poling include temperature, electric field, and the distance between needle and film. Since every sample for each film was fabricated at the same time under the same conditions, we assume that particle size and film composition are almost the same for every sample of the same material. The surface potential of the sample surface can be estimated by comparison technique [105], but in this study applied DC voltage was obtained. Usually the piezoelectric constant d_{31} is used to evaluate the poling state of ferroelectric material [106]. Since the method of measure d_{31} of the thick piezoelectric films is difficult [107] and not available, evaluation of the poling state was done by measuring the signals strength of the first reflected signal from the bottom of each

substrate with the same thickness. The HTUTs are excited by a negative impulse, where its peak value and duration time is about -100 V and 300 ns, respectively. The same excitation conditions were applied to all measurements throughout this thesis.

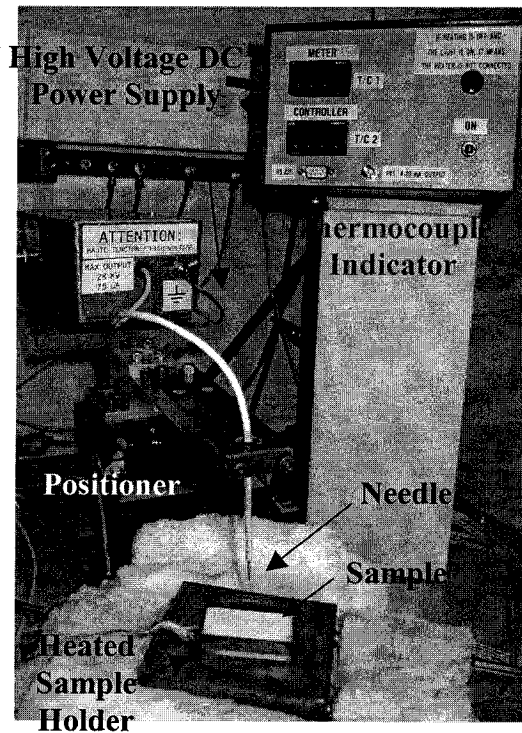


Figure 2.12 The experimental setup for corona poling.

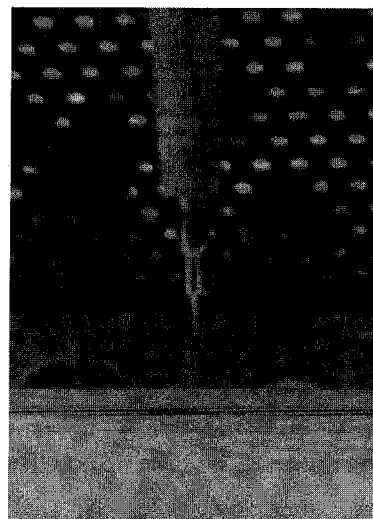


Figure 2.13 Corona discharge.

For instance, nine BIT/PZT composite films of 80 μm thickness were fabricated on mild steel (P20) discs. The distance between the needle and the surface of the sample was fixed at 2 cm, the shortest distance for the set-up to suppress spark discharge, a high electric field for poling is necessary. The experimental results, shown in Table 2.4, demonstrate that optimum conditions for these nine samples are correlated with both temperature and applied electric field. The temperatures for the best poling were 300°C at 18.5 kV, and 225°C at 22.5 kV, which are much lower than the T_c (650°C) of BIT. As temperature increases, internal energy increases, according to the first law of thermodynamics. When the applied voltage increases, supplied energy increases. It is expected that there is an optimal energy for poling, but more experimental points are required.

Table 2.4 Comparison of results for poling temperature and applied DC voltage for BIT/PZT corona poling and signal strength of the first reflected signal from the bottom of each substrate with the same thickness.

Sample No	Applied field (kV)	Temperature (°C)	Signal strength (dB)
a	18.5	225	-10
b	18.5	300	0
c	18.5	350	-5
d	18.5	500	-10
e	18.5	550	-30, peeling
f	22.5	25	-40
g	22.5	175	-15
h	22.5	225	-2
i	22.5	300	-10

Color changes were noticed after corona poling; the degree of color change depends on temperature and the applied electric field. Pictures of the samples are presented in Figures 2.14 (a)-(i). This may suggest that under severe poling conditions, piezoelectricity deteriorates due to not only microcracking, but also to structure transition. This color change does not correspond to signal strength of BIT/PZT, which depends on the poling state of the BIT powder. Color changes disappear when samples are heated up to 250°C after corona poling, even though this temperature is far below the maximum recommended operating temperature of BIT. Therefore it is assumed that this color change resulted from the PZT sol gel. The analysis will be given later in this chapter.

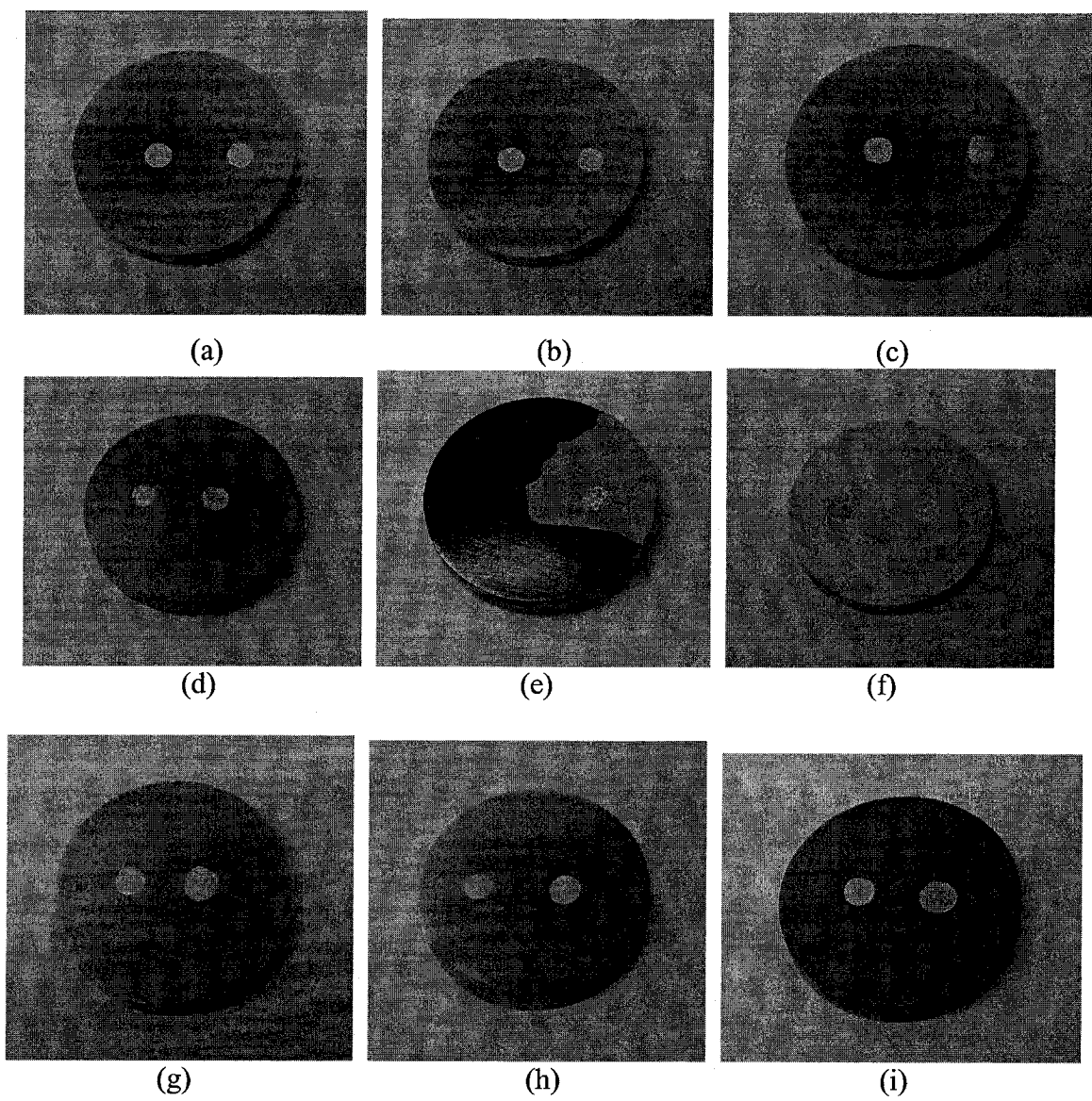


Figure 2.14 Comparison of color change after corona poling of BIT/PZT. The sample numbers correspond to those of Table 2.4.

Seven PZT/PZT composite films of 80 μm thickness on P20 discs were also prepared. Through many trials for PZT/PZT corona poling, good poling conditions concerning voltage, distance and temperature were obtained. Results and photos are shown in Table 2.5 and Figures 2.15 (a)-(g), respectively. Applied DC voltage and distance are not mutually independent, since they are related by the electric potential at the sample surface. Because there is discharge, the relationship between the distance and the potential of the surface of the film is non-linear. Further research will be necessary to obtain the distribution of voltage in a corona discharge. Assuming that the distribution of voltage in a DC and RF glow discharge is similar to that of corona discharge, over short distances there is an almost linear relationship. Optimum conditions for temperature and electric potential were supposed to be the same as those obtained for BIT/PZT. Color changes were not as obvious as with BIT/PZT, because the temperature of poling was lower. However, it can be mentioned that a higher temperature or electric potential causes larger poling area and stronger color change. Further research is needed to investigate these phenomena in more detail. However, similar phenomena appeared with BIT/PZT and PZT/PZT. As mentioned before, PZT sol gel is a highly possible key material for this color change.

Table 2.5 Comparison of results for poling temperature, applied DC voltage, and the distance between the needle and the sample during PZT/PZT corona poling.

Sample No.	Temperature ($^{\circ}\text{C}$)	Applied DV voltage (kV)	Distance (cm)	Signal strength (dB)
a	125	22.5	4	-10
b	175	18.5	4	-20
c	175	22.5	5	-8
d	175	22.5	4	-8
e	175	22.5	3	0
f	175	22.5	2	-6
g	225	22.5	4	-14

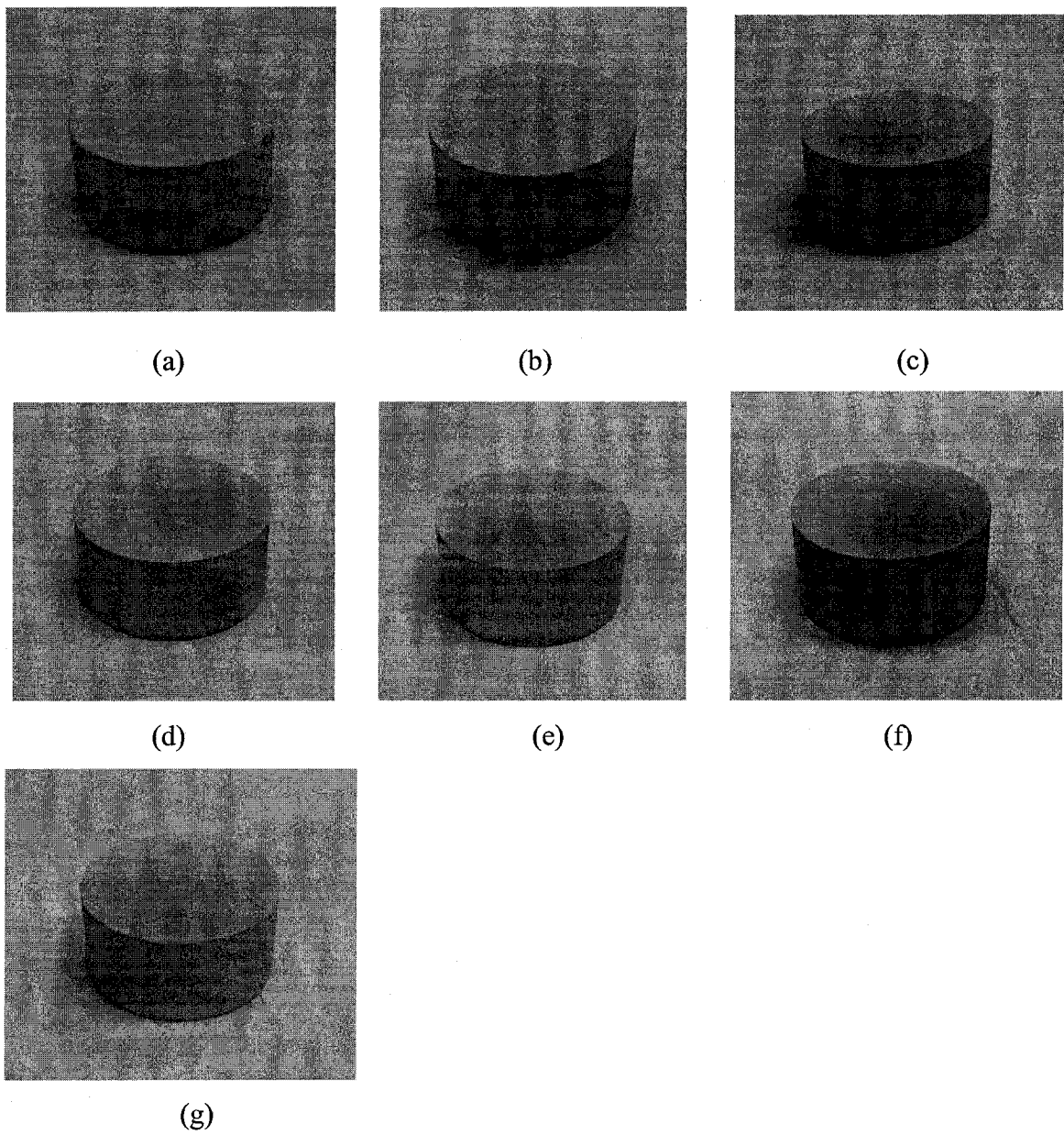


Figure 2.15 Comparison of color change after corona poling of PZT/PZT. The sample numbers correspond to those of Table 2.5.

X-ray diffraction (XRD) analysis was conducted on three PZT/PZT samples with different poling conditions, since the color change is often related to phase transition. PZT/PZT films were fabricated on silicon wafers with Pt under electrodes. The XRD result is shown in Figure 2.16. No significant difference among them was found. There seems to be good agreement between the XRD of PZT/PZT composite [107] and that of bulk PZT, even though the film color difference can be observed with the naked eye. This means even if phase transition exists in the film, it must be so small or so thin that XRD could not detect it. Furthermore the color change may not result from phase transition; by scratching the film, the color change was found only on the surface. Some chemical reaction may occur between the surface of the PZT sol gel and ions; PZT sol gel and PZT powder may not be chemically identical. XRD analysis was also conducted on a BIT/PZT sample and XRD in Figure 2.17 only shows that the crystallization was found for BIT but not PZT because there was no peak around 31° , where there should be the strongest peak for bulk PZT without orientation. It is speculated that the annealing condition used for the PZT sol gel was not sufficient to obtain PZT crystallization. Because the thermal treatments during the fabrication process for PZT/PZT were the same as that of BIT/PZT, PZT sol gel phase of PZT/PZT seems not to be crystallized, neither.

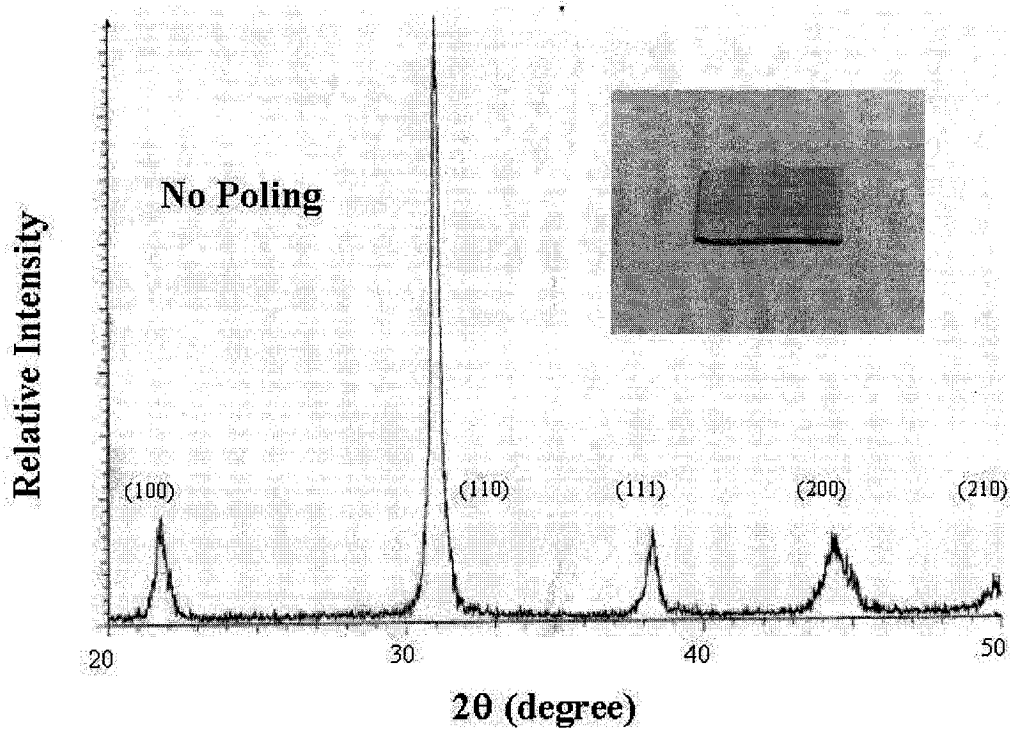


Figure 2.16 XRD of PZT/PZT.

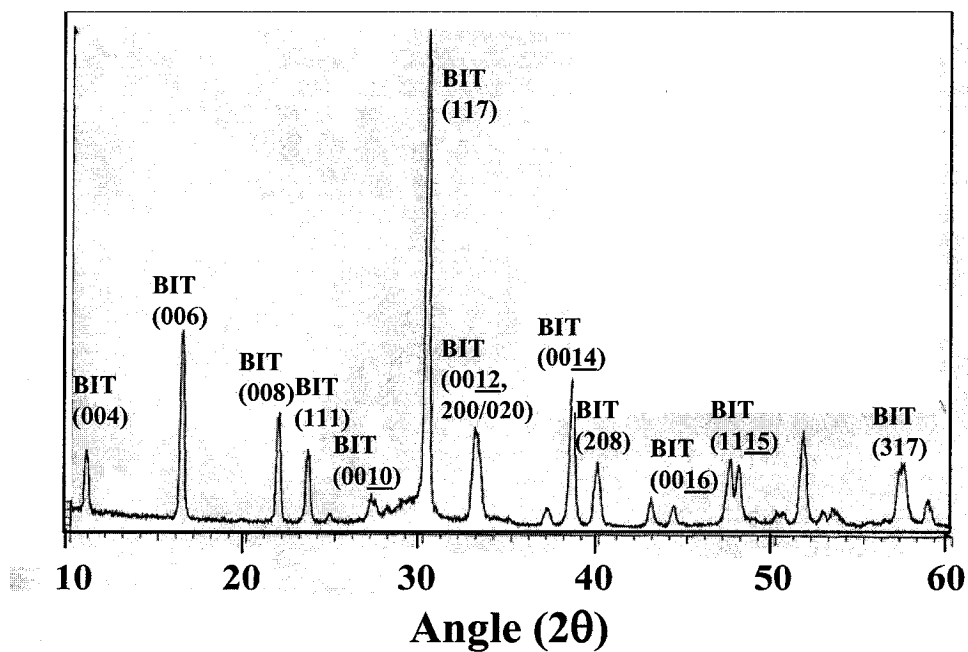


Figure 2.17 XRD of BIT/PZT.

Corona poling for PZT/Al₂O₃ was processed at 175°C, 22.5 kV and 2 cm distance, because the dielectric constant of Al₂O₃ sol gel is higher than that of PZT sol gel, so that a higher electric field is necessary for poling. No visible color change was noticed before and after corona poling in Figure 2.18, (a) and (b), respectively. Therefore it can be mentioned that the PZT sol gel phase is the main contributor to the color change of BIT/PZT and PZT/PZT after corona poling. After corona poling of PZT/Al₂O₃, several small brown dots were observed, corresponding to areas of spark discharge, and indicating that PZT powder changes color under very high voltage.

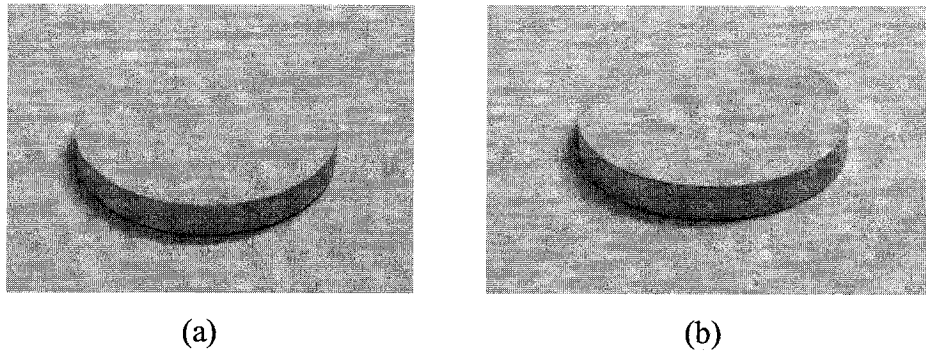


Figure 2.18 Comparison of color change before (a) and after (b) corona poling of PZT/Al₂O₃.

Corona poling for LT/PZT film was also examined. However, very weak piezoelectricity was confirmed when the distance between the needle and the surface of the sample was 1 cm and the voltage was around 22 kV, the maximum available voltage of the apparatus. LT has a higher coercive field than BIT and this is a probable reason for weak piezoelectricity. One centimeter distance is not preferable because many sparks discharged during corona poling deteriorating the piezoelectricity also. Further research could be possible when a new DC voltage supply with higher voltage limits is available.

2.2.8- Electrode fabrication

The top electrode material must be chosen carefully when it is fabricated on the piezoelectric film for HTUT. Aluminum has excellent characteristics as an electrode; however, it starts to oxidize above 450°C. It also introduces an undesirable phase of PZT sol gel, deteriorating the piezoelectricity [108]. Even though gold has excellent electric characteristics and can sustain high temperatures, it has insufficient mechanical strength [109]. Platinum is the best electrode material for high temperature use. Silver paste is also a good candidate because of the ease of fabrication and low cost. Sometimes peeling of silver paste electrode occurs due to organic solvent residues at high temperature, and above 500°C, oxidation tends to occur, causing deterioration of the signal strength of ultrasound. In this thesis, sputtered platinum top electrodes and painted silver paste top electrodes are mainly used.

2.3- Summary

The sol gel spray coating technique is useful to fabricate piezoelectric thick film onto various surfaces; therefore this technique has a potential to realize HTUTs at high temperatures for nondestructive evaluation of hot materials and monitoring industrial material processes. The detailed fabrication process has been described. BIT, PZT or LT powders were prepared and mixed with Al_2O_3 , PZT or BIT sol gel. Ball milling was used for milling the powders into fine size of a few μm diameter and establishing homogeneity of the composite sol gel. After a certain period, that composite sol gel was sprayed onto the substrate. Heat treatments, drying, firing, and annealing removed the organic solvents and residue within the sol gel, and achieved crystallization. Spray coating and heat treatments were repeated until a desirable thickness was obtained. After that, poling and top electrode fabrication followed. With traditional poling, first top electrodes were fabricated, then high DC voltage was applied to the piezoelectric film across the electrodes. Since dielectric breakdown disturbs sufficient poling, corona poling was used. High DC voltage of 18.5-22.5 kV was supplied through the needle during corona discharge process. After corona poling, the top electrodes were fabricated. Because there was no need of top electrode during corona poling, no breakdown was observed. Sputtered platinum or silver paste was used as top electrode materials.

Chapter 3

Sol gel spray composite film properties

3.1- Introduction

In sol gel spray coating, piezoelectric powders are dispersed in an Al_2O_3 , PZT or BIT sol gel homogeneously, and organized into a new composite material. It is important to measure the film properties of new material. The physical properties of interest for piezoelectric films are density, dielectric constant, elastic stiffness, piezoelectric constant and electromechanical coupling coefficient. It is not easy to obtain the precise values of these film properties. For example, the resonance method is recommended by the IEEE standard [110] is not suitable due to multiple resonance frequencies from substrate influence, and because the films produced by sol gel spray coating is mainly fabricated directly onto the substrate. Resonant spectrum (RS) method has been recently investigated [111,112]; in this method, the piezoelectric film with the substrate was considered as a composite resonator, three parameters of which, longitudinal velocity, density, and electromechanical coupling coefficient, might be determined. In the references [111,112], simulated data for PZT/PZT sol gel spin coating was presented, but experimental data was demonstrated only for ZnO film on a quartz substrate, not for PZT/PZT film on a stainless steel substrate.

In this chapter, first the parameters for longitudinal UT, such as dielectric, elastic and piezoelectric constants, and electromechanical coupling coefficient, are explained. Next, the measurement methods used to obtain film properties, including RS method, are explained with experimental data from sol gel spray composite UTs. Ultrasonic performance is demonstrated for each film, such as PZT/PZT, PZT/ Al_2O_3 , LT/PZT, and BIT/PZT, at both room and elevated temperatures. Durability tests for heating cycles

between room temperature and elevated temperature will be also presented for BIT/PZT film with platinum and silver paste top electrode.

3.2- Piezoelectric film properties

Since piezoelectricity couples elastic and dielectric phenomena, properties of piezoelectric materials cannot be discussed without dielectric and elastic constants. The piezoelectric equations are readily derived from thermodynamic potentials but magnetic field and heat interchange may be ignored. The equations may be expressed in matrix form when electric field E and stress T are independent constants [113]:

$$S = s^E T + d_t E \quad (3.1)$$

$$D = dT + \varepsilon^T E \quad (3.2)$$

where S is strain, s is elastic compliance, defined as $s_{ij} = \left(\frac{\partial S_i}{\partial T_j} \right)$, d is piezoelectric

constant, D is electric displacement, and ε is dielectric constant, defined as $\varepsilon_{ij} = \left(\frac{\partial D_i}{\partial E_k} \right)$.

Superscripts E and T denote measurement under conditions of constant electric field and constant stress, respectively. The designation d_t identifies a transposed matrix, indicating that the rows and columns of the d -matrix are interchanged. It is noted that every component of these equations is tensor form, except those are related to electromechanical coupling coefficient k_t , explained in later in this section.

When T and D are independent, the piezoelectric equations are [113]:

$$S = s^D T + g_t D \quad (3.3)$$

$$E = -gT + \beta^T D \quad (3.4)$$

where g is the piezoelectric constant, β is dielectric impermeability, related to the dielectric constant by $\beta_{ij} = \frac{(-1)^{i+j} \Delta_{ij}}{\Delta}$, Δ is the determinant of the ε_{ij} matrix, and Δ_{ij} is the minor obtained by excluding the i th row and j th column. Superscript D denotes measurement under conditions of constant electric displacement.

When S and E are independent, the piezoelectric equations are [113]:

$$T = c^E S + e_t E \quad (3.5)$$

$$D = eS + \varepsilon^S E \quad (3.6)$$

where e is the piezoelectric constant, c is elastic stiffness, related to elastic compliance by $c_{mk} = \frac{(-1)^{m+k} \Delta_{mk}}{\Delta}$, Δ is the determinant of the c_{mk} matrix, and Δ_{mk} is the minor obtained by excluding the m th row and k th column. Superscript S denotes measurement under conditions of constant strain.

When S and D are independent, the piezoelectric equations are [113]:

$$T = c^D S + h_t D \quad (3.7)$$

$$E = -hS + \beta^S D \quad (3.8)$$

where h is the piezoelectric constant. The four piezoelectric constants are interrelated. The definitions of the piezoelectric constants follow from Eq. 3.1-3.8 [113]:

$$\begin{aligned}
d &= \left(\frac{\partial S}{\partial E} \right)_T = \left(\frac{\partial D}{\partial T} \right)_E \\
g &= \left(\frac{-\partial E}{\partial T} \right)_D = \left(\frac{\partial S}{\partial D} \right)_T \\
e &= \left(\frac{-\partial T}{\partial E} \right)_S = \left(\frac{\partial D}{\partial S} \right)_E \\
h &= \left(\frac{-\partial T}{\partial D} \right)_S = \left(\frac{-\partial E}{\partial S} \right)_D
\end{aligned}$$

In most cases, the set of Eq. 3.1-3.2 is most useful, because electric field E and stress T are convenient independent factors. This is the reason the most common piezoelectric constant is the d -constant. However, in the case of application to longitudinal thickness mode of piezoelectric ceramics, such that $S_1 = S_2 = 0, S_3 \neq 0; T_1 = T_2 \neq 0, T_3 \neq 0$, the sets of Eq. 3.1-3.2 and Eq. 3.3-3.4 are not appropriate because this is a stress system. Therefore the sets of Eq. 3.5-3.6 or Eq. 3.7-3.8 are used for thickness mode.

Electromechanical coupling factors of piezoelectric materials is defined as the ratio of the mutual elastic and dielectric energy densities to the geometric mean of the elastic and dielectric self-energy densities. Neglecting thermal and magnetic terms, the internal energy U is given by [113]:

$$U = \frac{1}{2} S_i T_i + \frac{1}{2} D_m E_m, \quad i = 1 \text{ to } 6, m = 1 \text{ to } 3 \quad (3.9)$$

Using the set, Eq. 3.7-3.8, Eq. 3.9 can be written [113]:

$$\begin{aligned}
U &= \frac{1}{2} S_i c_{ij}^D S_j - \frac{1}{2} S_i h_{mi} D_m - \frac{1}{2} D_m h_{mi} S_i + \frac{1}{2} D_m \beta_{mk}^s D_k \\
&= U_{elas} + 2U_{mutual} + U_{dielec}
\end{aligned} \quad (3.10)$$

where $i, j = 1$ to 6 , $m, k = 1$ to 3 , U_{mutual} is mutual energy, U_{elas} is elastic energy, and U_{dielec} is dielectric energy. From this equation, the coupling factor follows [113]:

$$k = \frac{U_{mutal}}{\sqrt{U_{elas} U_{dielec}}} \quad (3.11)$$

Eq. 3.10 is complicated in the general case; when the number of independent parameters is reduced by symmetry and most stresses are zero, it becomes simpler.

Consider a transducer plate of thickness t with electroded major faces of area $l \cdot w$, l and w are the length and the width of the plate, respectively, and normal to the x_3 direction. If the transducer area is large compared to its thickness, the plate can be considered to be laterally clamped, *i.e.* $S_1 = S_2 = S_4 = S_5 = S_6 = 0$. And if it is assumed that there is no electric flux leakage, since a piezoelectric plate can be considered as an insulator, $D_1 = D_2 = 0$ and $\partial D_3 / \partial x_3 = 0$. These suggest that D and S be chosen as independent variables. Therefore the set of Eq. 3.7-3.8 is chosen for longitudinal transducers, and piezoelectric equations are given as [113]:

$$T_3 = c_{33}^D S_3 - h_{33} D_3 \quad (3.12)$$

$$E_3 = -h_{33} S_3 + \beta_{33}^S D_3 \quad (3.13)$$

From this set, thickness mode electromechanical coupling factor k_t is derived as

$$k_t = \frac{h_{33}}{\sqrt{c_{33}^D \beta_{33}^S}} = h_{33} \sqrt{\frac{\epsilon_3^S}{c_{33}^D}} \quad (3.14)$$

However, generally speaking, to obtain the values of h_{33} and c_{33}^D directly is difficult. Therefore, the resonance method is recommended by the IEEE standard [93] to obtain k_t . The wave equation for this case is [113]:

$$\frac{\partial^2 \xi_3}{\partial t^2} = \frac{c_{33}^D}{\rho} \frac{\partial^2 \xi_3}{\partial x_3^2} \quad (3.15)$$

where ξ_3 and ρ are the particle displacement and density, respectively. By solving Eq. 3.15 with boundary conditions, $T_3 = 0$ at $x_3 = 0$ and t , using Eq. 3.12, ξ_3 is given by [113]

$$\xi_3 = \frac{v^D h_{33} D_3}{\omega c_{33}^D} \left[\sin \frac{\omega x_3}{v^D} - \tan \frac{\omega t}{2v^D} \cos \frac{\omega x_3}{v^D} \right] \quad (3.16)$$

where $v^D = (c_{33}^D / \rho)^{1/2}$, and ω is angle frequency. By substituting Eq. 3.16 into Eq. 3.13, the electrical impedance can be obtained [113]:

$$Z = \frac{\int_0^t E_3 dx_3}{j\omega A D_3} = \frac{1}{j\omega C_0} \left[1 - k_t^2 \frac{\tan(\omega t / 2v^D)}{\omega t / 2v^D} \right] \quad (3.17)$$

where $C_0 = A \varepsilon_3^S / t$ is the clamped capacitance of the transducer, A are the area of the transducer, respectively. There are six characteristic frequencies for piezoelectric resonators: antiresonance frequency (zero reactance) f_a , resonance frequency (zero susceptance) f_r , frequency of maximum impedance f_m , frequency of minimum impedance f_n , parallel frequency (frequency of maximum resistance) f_p , and series frequency (frequency of maximum conductance) f_s . Measurement normally consists of determining the impedance of the piezoelectric resonator as a function of frequency, since we can assume that $f_m = f_p = f_a$ and $f_n = f_s = f_r$ for lossless materials. Therefore, the parallel resonant frequency f_p and thickness mode electromechanical coupling factor k_t are determined from Eq. 3.17 [113]:

$$f_p = \frac{v^D}{2t} \quad (3.18)$$

$$k_t^2 = \frac{\pi}{2} \frac{f_m}{f_n} \tan\left(\frac{\pi}{2} \frac{f_n - f_m}{f_n}\right) \quad (3.19)$$

When k_t^2 is small, Eq. 3.18 approximates to

$$k_t^2 = \frac{\pi^2}{4} \frac{f_m}{f_n} \cdot \frac{f_n - f_m}{f_n} \quad (3.20)$$

The electromechanical coupling factor is more important in characterizing a piezoelectric material than the set of elastic, dielectric, and piezoelectric constants, because it is more convenient for power transaction; also, direct comparison may be possible between piezoelectric materials with different dielectric and/or elastic constants. However, because of superposed spurious responses, it is difficult to identify the frequency of minimum impedance f_n and the frequency of maximum impedance f_m . A practical measurement method for UT with a substrate is introduced in the next section.

3.3- Measurement of sol gel sprayed film properties

3.3.1- Dielectric constant

Dielectric constant (permittivity) is defined as the incremental change in electric displacement per unit electric field, when the magnitude of the measuring field is very small compared to the coercive electric field. The value of the dielectric constant may depend on the polarization degree, electric field, mechanical stress, thermal history, and measurement frequency of the measuring field [104]. Therefore, measurement is usually made at 1 kHz with well under 1 V/mm [90]. In this thesis the relative dielectric constant, the ratio of the dielectric constant of the material to that of free space, is obtained by measuring capacitance. The dielectric constant is written as

$$\varepsilon^* = \varepsilon' + j\varepsilon'' \quad (3.21)$$

and the relative dielectric constant ε_r and dissipation factor Q_e^{-1} are equal to $\varepsilon'/\varepsilon_0$ and $\varepsilon''/\varepsilon'$, respectively. ε_0 is the dielectric constant of free space. The dissipation factor is the inverse of electrical quality factor Q_e . If it is assumed that the impedance of the sol gel composite film is composed only of capacitance, it can be obtained as

$$\begin{aligned} Z &= \frac{1}{j\omega C_0^*} \\ &= \frac{1}{j\omega \frac{A}{t} \varepsilon^*} \\ &= \frac{1}{j\omega \frac{A}{t} \varepsilon' \left(1 + j \frac{\varepsilon''}{\varepsilon'}\right)} \\ &= \frac{1}{j\omega C_0 - \omega C_0 Q_e^{-1}} \\ &= -\omega C_0 \left(j + \frac{Q_e^{-1}}{1 + Q_e^{-2}} \right) \end{aligned}$$

Therefore, in order to obtain the exact dielectric constant, measuring the clamped capacitance C_0 and dissipation factor Q_e^{-1} is required. However, in the case of sol gel composite films, because of the small values of dissipation factor Q_e^{-1} , ignoring the Q_e^{-1} effect produces no significant difference.

Capacitance and dissipation factor measurements were made using a Hewlett Packard HP 4284 LCR meter and 4192A LF Impedance Analyzer at 1 kHz with 1 mV/ μm . The relative dielectric constant ϵ_r can be obtained as

$$\epsilon_r = \frac{C_0 t}{\epsilon_0 A} \quad (3.22)$$

Table 3.1 presents values of the relative dielectric constant ϵ_r and dissipation factor Q_e^{-1} of each film, PZT/ Al_2O_3 , PZT/PZT, LT/PZT, BIT/PZT, and BIT/BIT. The errors were obtained empirically. The dielectric constant of composite materials corresponds to those of powder and sol gel. In Appendix A, double cube model including three phases, powder, sol gel, and porosity is developed. One of the merits of this model is to predict the dielectric constants of sol gel sprayed composite films and only the results were presented here as Figure 3.1.

Table 3.1 Measured dielectric constants and dissipation factors.

	relative dielectric constant ϵ_r	dissipation factor Q_e^{-1}
PZT/ Al_2O_3	30 ± 10	0.006 ± 0.002
PZT/PZT	320 ± 20	0.026 ± 0.002
LT/PZT	50 ± 10	0.013 ± 0.002
BIT/PZT	80 ± 10	0.008 ± 0.002
BIT/BIT	40 ± 10	0.018 ± 0.002

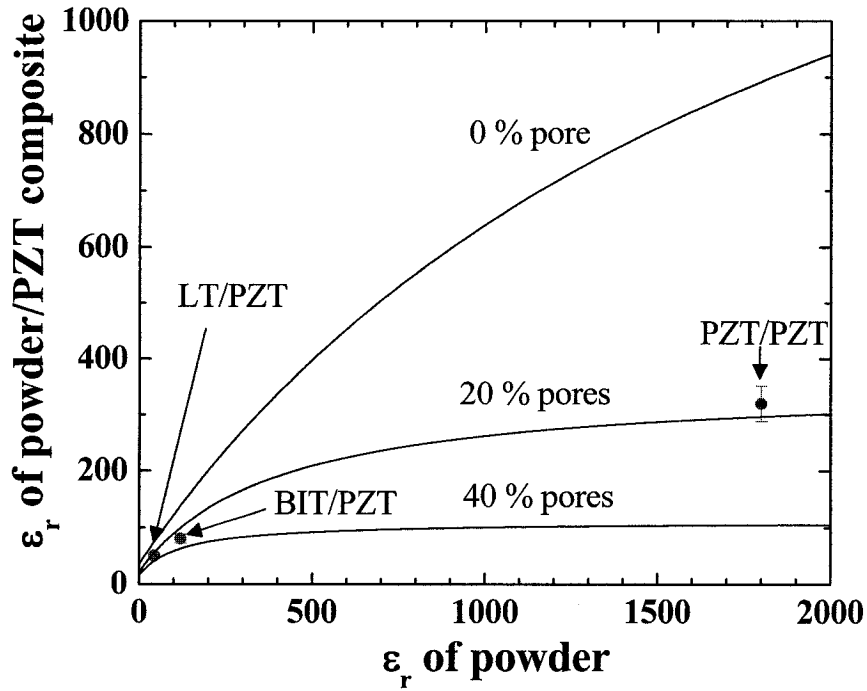


Figure 3.1 Comparison of relative dielectric constant calculations of powder/PZT sol gels from conventional cube model and double cube model including pores, as a function of the relative dielectric constant of powder, with experimental results.

3.3.2- Piezoelectric constants d_{33} , g_{33}

d_{33} is associated with strain along the z-axis in response to an applied electric field along the z-axis. Thus a large piezoelectric constant d_{33} is desirable for an actuator. Here the piezoelectric constant d_{33} was determined by static tests, such as with a Berlincourt meter, illustrated in Figure 3.2. The standard piezoelectric material, whose capacitance and d_{33} are already known, is placed in series with the piezoelectric sample, and a known force F_3 is applied to both materials, the standard material and the sample. The produced potentials of both materials, V_1 and V_2 , are measured. If we assume that the force across both the standard and the sample is the same, the following equation is obtained [89]:

$$d_{33}^2 = \frac{d_{33}^1 C_2 V_2}{C_1 V_1} \quad (3.23)$$

where subscripts and superscripts 1 and 2 refer to the standard and the sample respectively. Since C_1 and d_{33}^1 are known, C_2 can be obtained easily and V_1 and V_2 are measured by the Berlincourt meter, d_{33}^2 can be calculated by Eq. [3.23].

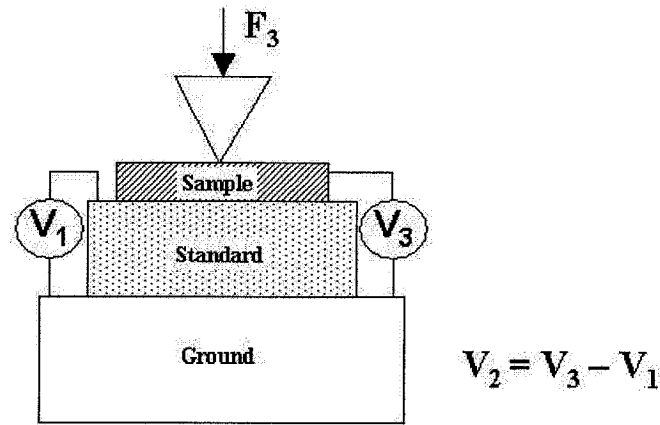


Figure 3.2 A schematic of a Berlincourt meter.

In another method to measure d_{33} , optical method has been developed. Recently optical systems have advanced to realize high position resolution. A heterodyne interferometer can measure displacement using two optical beams of equal intensity but slightly different frequencies. By measuring the beat, the position difference can be obtained with fine resolution within laser wavelength. d_{33} can be calculated by the following equation as [89]:

$$d_{33} = \frac{S_3}{V} \quad (3.24)$$

where S_3 is the developed strain along the z axis, and V is the applied voltage. The Berlincourt meter is simple, but less accurate than the optical method. In addition, in real use for UTs, the applied voltage is relatively high, perhaps 100-300 V; this would further

disadvantage for Berlincourt meter, since the electric potential is much lower than that during measurement.

Table 3.2 presents values of the piezoelectric constants d_{33} of and g_{33} of PZT/Al₂O₃, PZT/PZT, and LT/PZT. The d_{33} of PZT/Al₂O₃ was obtained by a Berlincourt meter, and those of PZT/PZT and LT/PZT by a Zygo laser interferometer system (Middlefield, CT, USA). The values of d_{33} are much lower than those of bulk PZT (PZT: 400, LT: 8), because the sol gel composite film has a low dielectric constant. Piezoelectric constant g_{33} is related to d_{33} as [110]:

$$g_{33} = \frac{d_{33}}{\epsilon_3^T} \quad (3.25)$$

Piezoelectric constant g_{33} represents the developed electric field in the thickness direction that responds to applied mechanical stress in the same direction as the electric field, so that it may be a better indicator of transducer performance.

Table 3.2 Measured piezoelectric constant d_{33} and g_{33} .

	d_{33} (10 ⁻¹² m/V)	g_{33} (10 ⁻³ V·m/N)
PZT/Al ₂ O ₃	0.03	0.11
PZT/PZT	180	64
LT/PZT	60	136

Because the Berlincourt meter and Zygo laser interferometer system are not available after BIT/PZT films have been developed, no data of d_{33} and g_{33} are given here.

3.3.3- Thickness mode electromechanical coupling factor k_t

As mentioned before, in characterizing a piezoelectric material the electromechanical coupling factor is one of the important properties, defined as the square root of the ratio of the accumulated mechanical energy in response to an electrical input or *vice versa*. The thickness mode is excited for longitudinal UTs. The resonance method is recommended by the IEEE standard [110] to obtain the value of k_t . However, this method is not suitable for the film produced on the substrate by the sol gel spray technique, since the substrate effect cannot be ignored, and the piezoelectric film and the substrate compose a composite resonator, resulting in multiple resonances. In addition, film characteristics depend on the substrate, so that it may not be useful to obtain values without the substrate. Several attempts to extract k_t by curve-fitting techniques have been demonstrated for composite resonators [114,115]. However, curve-fitting methods often require many initial variables such as c_{33}^D , which are unknown, and sometimes the values of the variables are critical for the final results.

Recently, a resonant spectrum (RS) method has been reported to extract k_t [111,112]. In this technique, three parameters of piezoelectric films, electromechanical coupling factor k_t , density ρ , and c_{33}^D , can be obtained from the spacing of the parallel resonant frequencies (SPRF) and the parameters of the substrate and electrodes for the composite resonator. In a previous paper, extracting k_t for sol gel composite films was tried only by simulation [111,112]. In this thesis, empirical measurement of the k_t is attempted by RS method, based on a two-layer composite resonator [111], as shown in Figure 3.3. The electromechanical coupling factor k_t of the composite resonator can be determined by these parameters, longitudinal velocity v , density ρ , and thickness t . The subscript sb indicates those of the substrate. The effect of top electrodes was ignored because center frequency of the sol gel film was not so high, around 10 MHz [112].

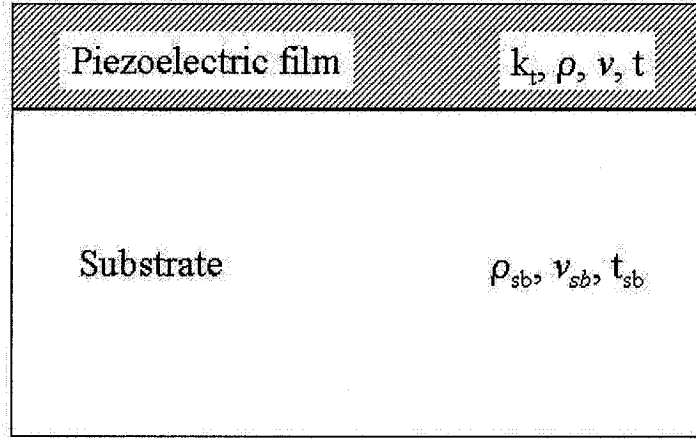


Figure 3.3 A two-layer composite resonator produced by the sol gel spray technique, with the definitions of the material parameters and dimensions.

The input impedance of the composite resonator that can be obtained from Sittig's model [116] is

$$Z_{in} = \frac{1}{j\omega C_0} \cdot \left[1 - \frac{k_t^2}{\gamma} \cdot \frac{2 \tan(\gamma/2) + z_{sb} \cdot \tan \gamma_{sb}}{(1 + z_{sb} \cdot \tan \gamma_{sb} / \tan \gamma)} \right] \quad (3.26)$$

where $C_0 = \epsilon_3^s A / t$ is the static capacitance, $\gamma = 2\pi f \cdot t / \nu$, $\gamma_{sb} = 2\pi f \cdot t_{sb} / \nu_{sb}$ is the phase delay of the longitudinal wave in the film and substrate, respectively, z_{sb} is the acoustic impedance of the substrate normalized to $Z_0 = \rho \nu$, the acoustic impedance of the piezoelectric layer, and A is the area of electrodes. The impedance response has a global hyperbolic decrease resulting from C_0 , and a series of resonant peaks related to k_t . The parallel and series resonance frequency equations can be derived from Eq. 3.22, if we assume that the materials are lossless and that $f_m = f_p$ and $f_n = f_s$. Therefore, if we ignore the imaginary parts of the material parameters, parallel frequency f_p and series frequency f_s can be derived by setting $|Z_{in}|$ to infinity or 0, respectively.

$$\tan \gamma + z_{sb} \tan \gamma_{sb} = 0 \quad (3.27)$$

$$\tan \gamma + z_{sb} \tan \gamma_{sb} = \frac{k_t^2}{\gamma} \cdot [2 \tan(\gamma/2) + z_{sb} \tan \gamma_{sb}] \cdot \tan \gamma \quad (3.28)$$

Since the composite resonator is assumed to be lossless, k_t can be obtained from Eq. 3.23 as follows [111]:

$$k_t^2 = \gamma \cdot \frac{\tan \gamma + z_{sb} \tan \gamma_{sb}}{[2 \tan(\gamma/2) + z_{sb} \tan \gamma_{sb}] \cdot \tan \gamma} \quad (3.29)$$

where $f = f_s(m_N)$ and m_N is the mode order at the center of the first normal region i.e. $\tan \gamma = 0$. It is not recommended to extract k_t from Eq. 3.29 directly, because real composite resonators include loss components in both layers, the piezoelectric film and the substrate, which might amplify errors. Therefore special modes must be involved to suppress further errors.

For a multimode composite resonator, the thickness of the substrate is much larger than that of the piezoelectric film, and the SPRF is not uniform but distributed periodically. The period may be obtained by taking $\tan \gamma = 0$ or $\tan \gamma \rightarrow \infty$. Regions where $\tan \gamma = 0$, meaning that γ is an integer multiple of π , are referred to as normal regions. Regions where $\tan \gamma = \infty$, meaning that γ is a half-integer multiple of π , are referred to as transition regions. k_t can be derived by knowing the thickness, density, and velocity of both layers, piezoelectric film and substrate, and evaluating the value of the effective coupling factor for the m th resonance mode $k_{eff}^2(m)$, given by [111,112]

$$k_{eff}^2(m) \approx \frac{\pi^2}{4} \frac{f_s(m)}{f_p(m)} \left(1 - \frac{f_s(m)}{f_p(m)} \right) \quad (3.30)$$

$f_p(m)$ and $f_s(m)$ are the m th parallel and series resonant frequencies, respectively. The maximum value of $k_{eff}^2(m)$ should be used for optimal accuracy [111,112]. When the

acoustic impedance of the substrate is larger than that of the piezoelectric film, $k_{eff}(m)$ is located within the first transition region. Because most sol gel spray technique films are fabricated on hard metal substrates, using the first transition region to calculate k_t is more accurate than using the first normal region. In addition, the impedance and phase were measured with an HP 4192A LF impedance analyzer from 0.5 MHz to 13 MHz; below 13 MHz only the first minimum SPRF, *i.e.* first transition region, was observed. Therefore only the equations for the transition region are explained.

At the center of the first transition region, the m_{T+1} order resonant mode corresponds to

$$\begin{aligned}\gamma &\approx \pi/2 + \chi \\ \gamma_{sb} &\approx (m_T + 1/2)\pi + \delta\end{aligned}$$

where $m_T + 1$ is the mode order of the bare substrate plate near the center of the first transition region, expressed as [111]

$$m_T = \text{round}[\{(vt_{sb}/v_{sb}t)-1\}/2] \quad (3.31)$$

And χ and δ are small quantities. After some algebraic manipulation, we obtain the spacing of parallel resonant frequencies at the first transition region Δf_T and the electromechanical coupling factor k_t [111]:

$$\Delta f_T = \Delta f_0 \left(1 + \frac{\rho_{sb} v_{sb}^2}{\rho v^2} \frac{t}{t_{sb}} \right)^{-1} \quad (3.32)$$

$$k_t^2 = \left(1 + \frac{\rho v^2}{\rho_{sb} v_{sb}^2} \frac{t_{sb}}{t} \right) \cdot \frac{1}{\Gamma} \cdot k_{eff}^2(m_T) \quad (3.33)$$

where $\Delta f_0 = v_{sb}/2t_{sb}$ is spacing of the parallel resonance frequency of a bare substrate.

$$\begin{aligned}\Gamma &= 1 + 2 \cdot \frac{\rho v}{\rho_{sb} v_{sb}} \cdot (1 + \chi) \cdot \delta \\ &= 1 - 2\rho v \left(1 + \frac{2\pi f_s(m_T)t}{v} - \frac{\pi}{2} \left(\frac{2\pi f_s(m_T)t}{\rho_{sb} v_{sb}^2} - \frac{(m_T + 1/2)\pi}{\rho_{sb} v_{sb}} \right) \right)\end{aligned}\quad (3.34)$$

is a correction factor [111,112]. It should be noted that when $(vt_{sb}/v_{sb}t)$ is an odd integer or sufficiently large, the correction factor is near one, but when is $(vt_{sb}/v_{sb}t)$ neither an odd integer nor very large (50, for example), the correction factor is not near unity [111,112].

Extracting the electromechanical coupling factor k_t was attempted for a 60 μm BIT/PZT film deposited on a steel block. The amplitude and phase of the impedance were measured with a system based on a Hewlett Packard 4192A LF impedance analyzer as a function of frequency between 1 and 13 MHz, since 13 MHz is the highest frequency for this system. Figure 3.4 shows the experimental impedance results. The amplitude curve clearly shows a hyperbolic decrease due to static capacitance. The peaks of the phase result from multiple resonances. The peaks of the amplitude are not so clear, indicating the high loss inside the film due to pores [112]. The parameters of this composite resonator follow:

$$\begin{aligned}t &= 60 \text{ } (\mu\text{m}) \\ \rho &\approx 4000 \text{ (measured approximately, g/cm}^3\text{)} \\ t_{sb} &= 12500 \text{ } (\mu\text{m}) \\ \rho_{sb} &= 7840 \text{ (g/cm}^3\text{)} \\ v_{sb} &= 5874 \text{ (m/s)}\end{aligned}\quad (3.35)$$

The distribution of SPRF and k_{eff}^2 (m) are shown in Figures 3.5 and 3.6, respectively.

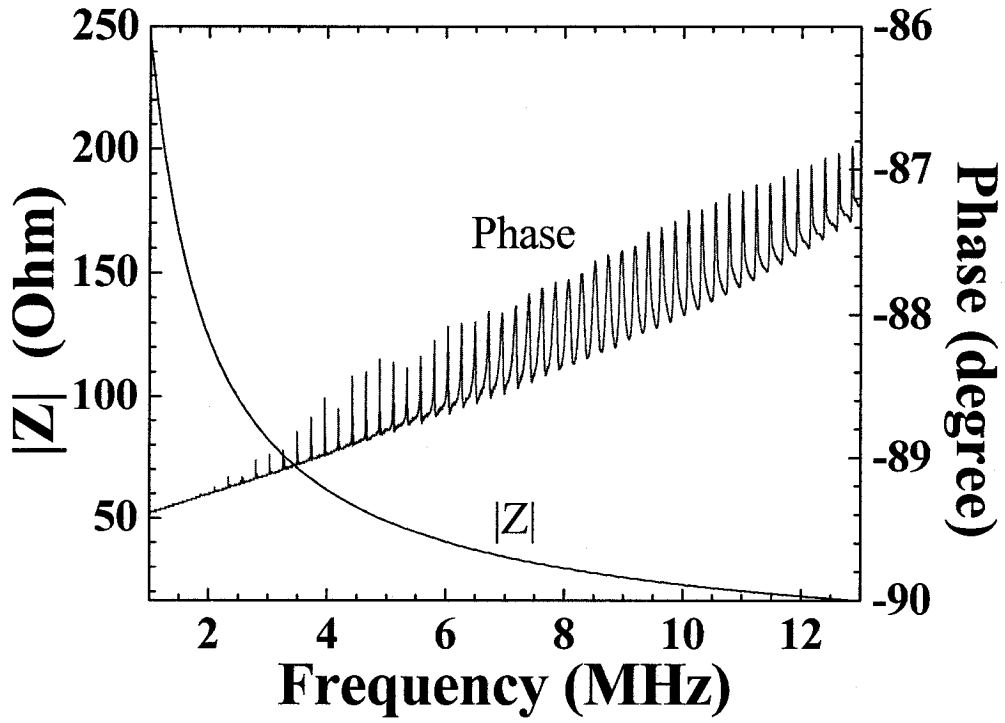


Figure 3.4 The impedance of a 60 μm BIT/PZT film on a steel substrate composite resonator as a function of frequency.

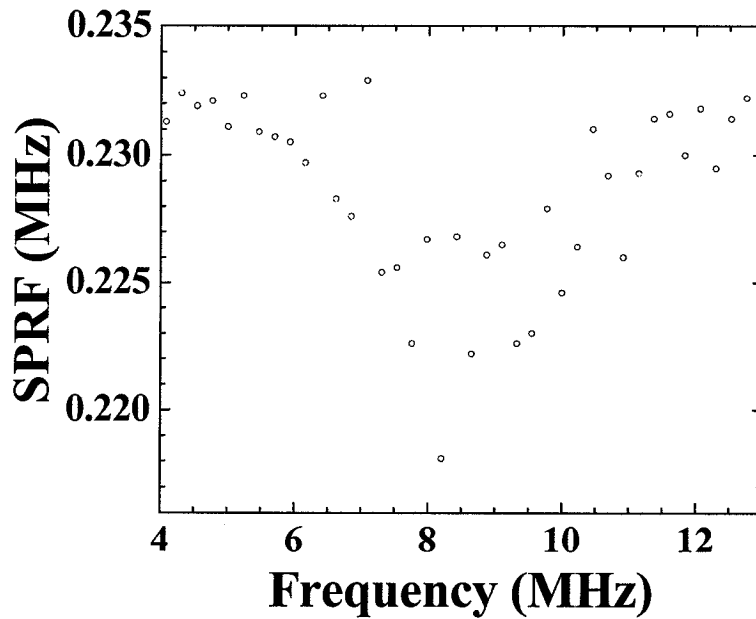


Figure 3.5 The SPRF of a 60 μm BIT/PZT film on a steel substrate composite resonator as a function of frequency.

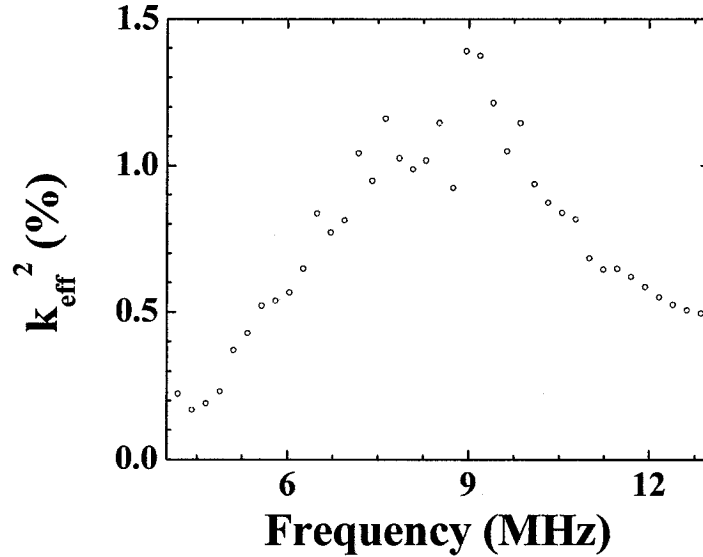


Figure 3.6 The k_{eff}^2 of a 60 μm BIT/PZT film on a steel substrate composite resonator as a function of frequency.

Down peak and peak around 9 MHz may be confirmed from Figures 3.5 and 3.6. The data for k_{eff}^2 are smoother and less dispersed than those for SPRF, agreeing with previous papers [111,112], that indicates the possibility of the measurement of k_t . However, there are difficulties to obtain the precise value of k_t of PZT/PZT by these results. First, the measurable frequency of the impedance analyzer used in this thesis was limited up to 13MHz therefore the center of normal region, i.e. the first maximum of the SPRF, Δf_N could not be obtained. In general RS method, from Δf_N the density ρ was obtained, and from Δf_T and ρ , v was calculated, then finally k_t was obtained. In this thesis, instead of Δf_N , first v was obtained from Eq. 3.32. It is noted that round function was used in Eq. 3.32 and it caused ambiguity. And also distributions of SPRF and k_{eff} become dispersive near the peak, because around the resonant frequency, the composite resonator becomes very sensitive and unstable, especially if the substrate material is not uniform as quartz or sapphire. Changing substrate material and dimensions, top electrode configuration, and measurement should be able to avoid reduce the uncertainty.

Although k_t is one of the important factors to evaluate the piezoelectric strength of the HTUT, signal strength and SNR were used in this thesis because they are practical and k_t measurement is not accurate enough for porosity of thick sol gel film.

3.4- Ultrasonic performance of sol gel composite films

3.4.1- PZT/PZT

Figures 3.7 and 3.8 show typical examples of ultrasonic performance of PZT/PZT composite film fabricated on steel substrate having a thickness of 12 mm at both room temperature and 220°C. Several round trip echoes from the bottom of the substrates are confirmed. The signal strength is 9 dB weaker at 220°C than at room temperature. Signal-to-noise ratio (SNR) is about 30 dB. The center frequency is 4.5 MHz, with a 6 dB bandwidth of 5 MHz. It is noted that PZT/PZT composite film shows higher ultrasonic signal strength at temperatures up to 220°C than PZT/Al₂O₃, LT/PZT or BIT/PZT.

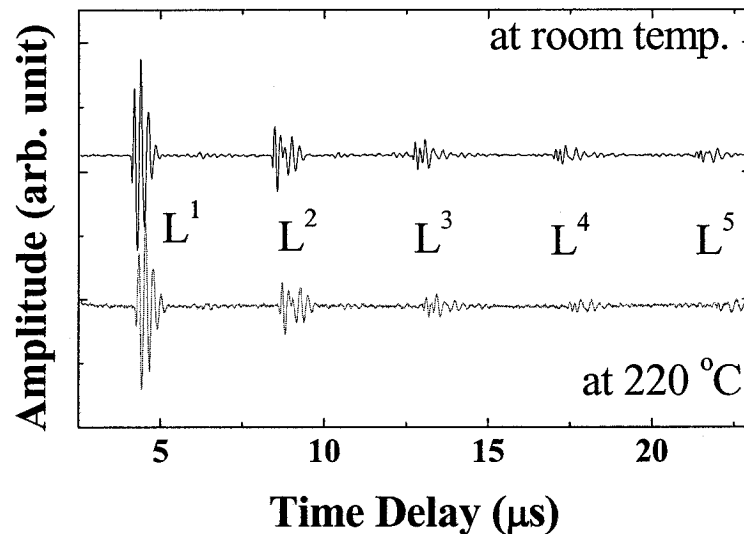


Figure 3.7 Signals in time domain of PZT/PZT film.

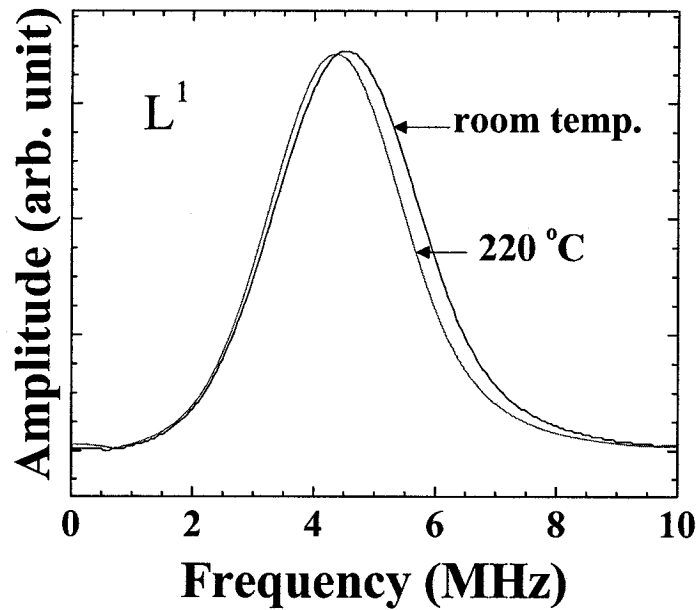


Figure 3.8 Signal in frequency domain of PZT/PZT film for L^1 of the device depicted in Figure 3.7.

3.4.2- PZT/ Al_2O_3

Figure 3.9 shows the ultrasonic performance of a 100 μm PZT/ Al_2O_3 film deposited on a steel substrate at room temperature. This UT provides a center frequency of 3.0 MHz and a 1.3 MHz bandwidth, with SNR of about 25 dB. However, because of the low dielectric constant of Al_2O_3 sol gel, the signal strength is weaker by about 40 dB than PZT/PZT. Al_2O_3 was used for the suppression of the crack and/or peeling but the temperature stability of piezoelectricity shows no improvement from PZT/PZT because the piezoelectricity totally depends on the PZT piezoelectric powder.

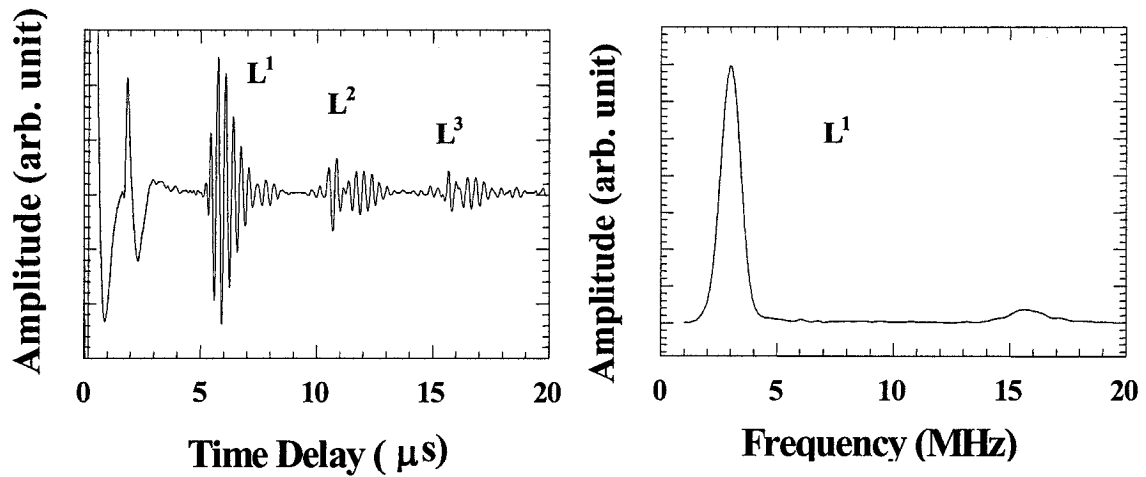


Figure 3.9 Ultrasonic performance in time and frequency domains of a 100 μm PZT/ Al_2O_3 film at room temperature.

3.4.3- LT/PZT

A 60 μm LT/PZT film was deposited on a 51 mm long clad steel buffer rod, which consists of a 10 mm diameter steel core and 1 mm stainless steel cladding. Figure 3.10 shows the round trip echoes, L^1 , L^2 , and L^3 reflected from the end of the clad buffer rod at room temperature. This film UT has a center frequency of 7 MHz and a 2.5 MHz 6 dB bandwidth, with an SNR of about 25 dB. The signal strength at room temperature is about 30 dB weaker than that of PZT/PZT. Since LT has a relatively high Curie temperature of 625°C, an LT/PZT UT can operate at higher temperatures than PZT/PZT, at least up to 368°C [45]. Figure 3.11 provides its ultrasonic performance in time domain from 30°C to 250°C. The difference of signal strength between 30 and 250°C is less than 2 dB

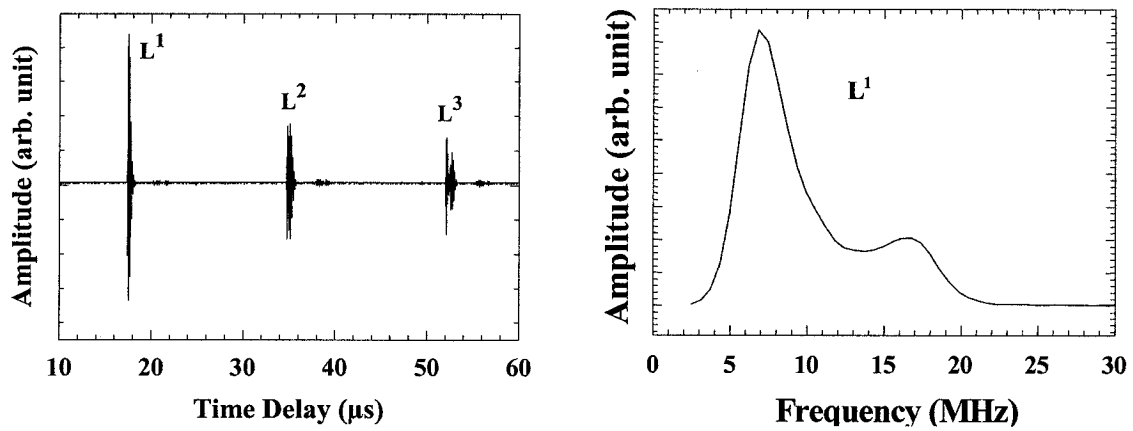


Figure 3.10 Ultrasonic performance in time and frequency domains of a 60 μm LT/PZT film deposited on a clad steel buffer rod, at room temperature.

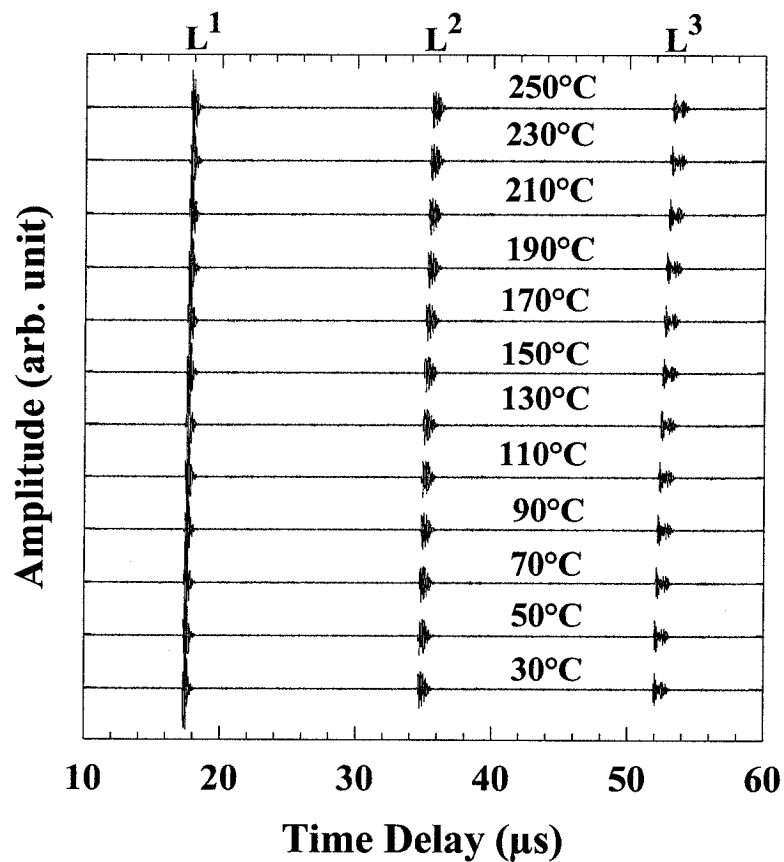


Figure 3.11 Ultrasonic performance in time domain of a 60 μm LT/PZT film deposited on a clad steel buffer rod, at temperatures from 30°C to 250°C.

3.4.4- BIT/PZT

Figure 3.12 shows typical results of longitudinal wave ultrasonic signals reflected at the bottom of a 12 mm thick steel substrate with BIT/PZT sol gel film at room temperature and 625°C in time domain; Figure 3.13 shows the signal in frequency domain. This film UT provides a center frequency of 13 MHz and a 13 MHz 6 dB bandwidth, with an SNR of about 30 dB. The signal strength at room temperature is about 25 dB weaker than that of PZT/PZT. Since BIT has a relatively high Curie temperature, BIT/PZT UT can work at higher temperatures than PZT/PZT, and even than LT/PZT. However, 625°C was chosen to investigate the highest temperature that BIT/PZT can survive for several days' operation.

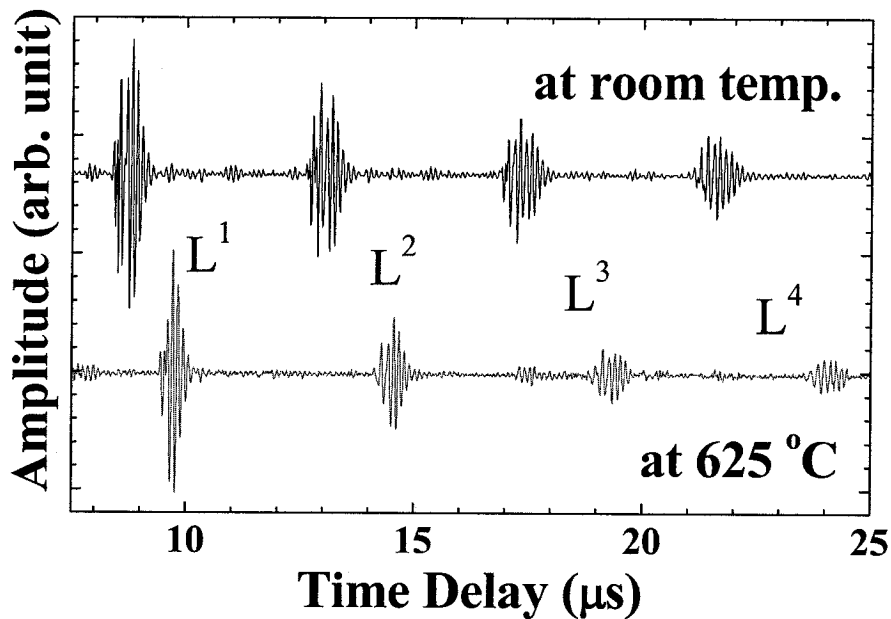


Figure 3.12 Ultrasonic signals reflected at the bottom (a), and frequency spectrum (b), of an 80 μm BIT/PZT film on a 12 mm thick steel substrate at room temperature and 625°C.

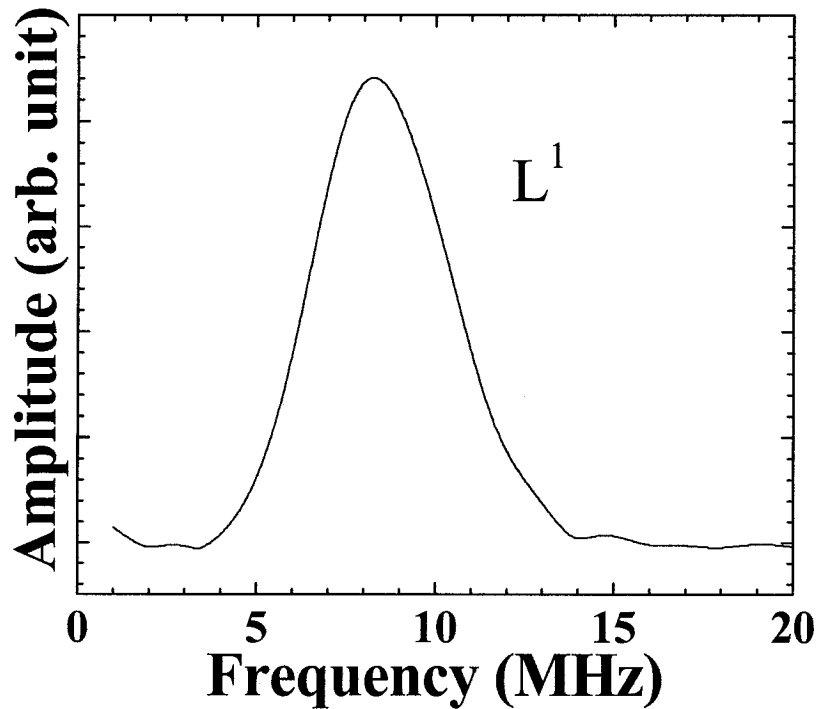


Figure 3.13 Ultrasonic signal of BIT/PZT film in frequency domain at 625°C for L^1 of the device depicted in Figure 3.12.

3.4.5- Durability test

In order to test the durability, the HT probe was undertaken the thermal cycles between room temperature and elevated temperatures using a furnace. During each thermal cycle it took about one hour to heat the probe from room temperature to elevated temperatures, and then to cool it to room temperature. The durability test of the probe with the silver paste top electrode up to a furnace temperature of 250°C verified that strength of the signal reflected from the probing end gradually decreased about 4 dB in 100 cycles but there was no further deterioration of the signal observed after 100 cycles up to 180 cycles. The test was terminated in 180 cycles. In the test of the probe with the platinum top electrode from room temperature up to 500°C, the signal strength gradually decreased with -0.05dB/cycle in 140 cycles. It may be due to the following reasons:

damage of the electrode due to mechanical contact with improper force; deterioration of piezoelectricity of the BIT/PZT film because of depoling at elevated temperatures; detachment of the top electrode from the ceramics film because of difference of thermal expansion coefficient between the platinum and ceramics; detachment of the ceramics film from the steel substrate because of difference of thermal expansion coefficient between the ceramics and the steel substrate.

3.5- Summary

The important properties of piezoelectric films are electromechanical coupling coefficient, dielectric constant, piezoelectric constant, and density. The measurements of each film characteristics, PZT/PZT, PZT/Al₂O₃, LT/PZT, and BIT/PZT, were investigated. The electromechanical coupling factor is one of the important parameters, but it is difficult to perform an accurate measurement due to the film porosity. From experimental data, at low temperature, PZT/PZT shows the best piezoelectricity, while at high temperature, BIT/PZT is the best material for HTUT. The ultrasonic performance of BIT/PZT HTUTs have been confirmed at temperatures to higher than 450°C and durability tests were held for thermal cycles.

Chapter 4

Applications of sol gel composite HTUTs for nondestructive evaluation of materials at high temperature

4.1- Introduction

There is a demand of NDE of metals at HT applications such as galvanization plant or nuclear power generation plant. As mentioned in the previous chapter, the sol gel spray technique is useful for fabricating sensors onto metals, since the piezoelectric films made by this method can be directly coated onto the host metallic structure, at desirable places to perform the nondestructive evaluation [70]. BIT/PZT was selected because this material can withstand higher temperatures than PZT/PZT, PZT/Al₂O₃, and LT/PZT as mentioned before. Since host metals may have different shapes, here BIT/PZT films fabricated directly onto various shaped surfaces are demonstrated. Their performance as piezoelectric UTs will be presented as well. Flat and curved self-support films by sol gel spray coating are also presented. In order to demonstrate their ultrasonic sensing capability, the NDE of metals at the elevated temperatures will be illustrated as well.

For one application of the interest, immersion type HT probe is desired for the mapping the wall thickness of the steel container at galvanization plant. In previous work, ultrasonic measurements and imaging in molten zinc were performed using long steel buffer rods [117]. The room temperature UT was outside of the molten zinc and cooled by compressed air. However, such a long buffer rod and cooling system may not be convenient because of size constraints. Since sol gel type HTUTs can operate up to 450°C with high SNR, an immersion HTUT probe in compact size is feasible. Therefore,

thickness measurement of a steel plate in the molten zinc at 450°C and surface and sub-surface imaging in silicone oil at 200°C using these immersion HTUT probes [118] will be investigated.

4.2- Ultrasonic performance of BIT/PZT films on various surfaces

In this section, BIT/PZT films are fabricated by the sol gel spray technique onto various surfaces of metals, such as cylindrical and spherical convex surfaces, cylindrical and spherical concave surfaces, and thin sheets and foils. Their ultrasonic performances at elevated temperatures are also investigated.

4.2.1- Cylindrical convex surfaces

Figure 4.1 shows a 40 μm thick BIT/PZT film deposited onto a cylindrical steel shell with an outer diameter of 25.4 mm. Figure 4.2 (a) shows the ultrasonic signals at 440°C, in time domain where L^n is the n th round trip echo in the cylindrical steel wall with a thickness of 6.35 mm. The frequency spectrum of L^1 signal is given in Figure 4.2 (b). The center frequency, 6dB bandwidth and SNR are 12 MHz, 9 MHz and 26 dB, respectively. Since many parts in various engineering materials and structures may have this kind of shape, such as the barrel of a micro-molding machine, the sol gel spray coating technique provides the availability of piezoelectric and ultrasonic sensors to these materials and structures.

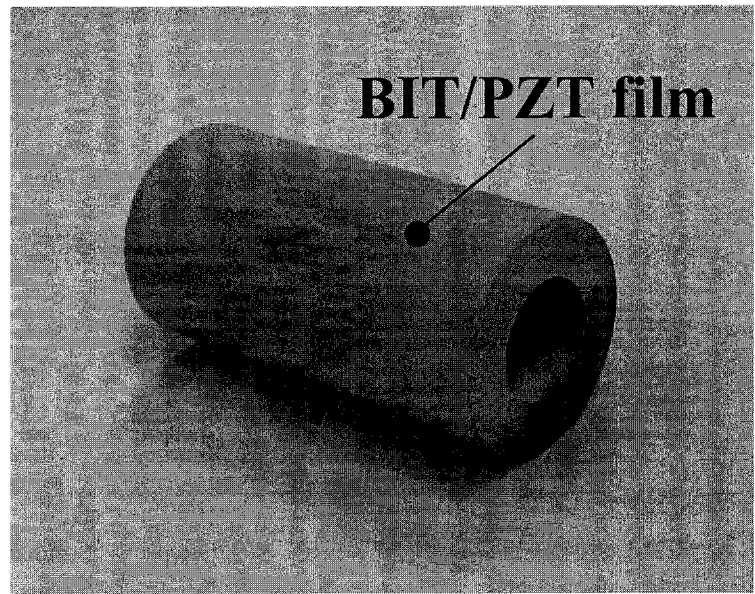


Figure 4.1 A 40 μm thick BIT/PZT film deposited onto a cylindrical steel shell.

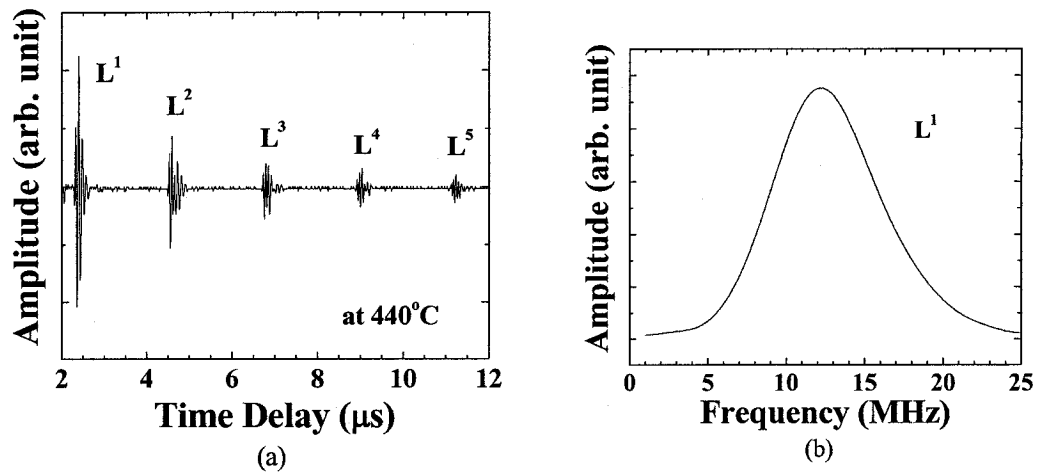


Figure 4.2 The ultrasonic performance (a) in time and (b) frequency domain for L^1 at 440°C of the device depicted in Figure 4.1.

4.2.2- Spherical convex surfaces (ball)

Figure 4.3 shows a 90 μm thick BIT/PZT film deposited onto a spherical steel ball with a diameter of 19 mm. Figure 4.4 (a) shows the ultrasonic signals at 440°C in time domain where L^n is the n th round trip echo across the diameter of the ball. The frequency spectrum of L^1 signal is given in Figure 4.4 (b). The center frequency, 6dB bandwidth and SNR are 9.5 MHz, 4MHz and 40 dB, respectively. An interesting application for a piezoelectric film on a ball was reported recently: when a 45 MHz surface acoustic wave (SAW) sensor is fabricated onto a quartz ball with a diameter of 10 mm, it has a long propagation length of 1.3 m without much diffraction loss [119]; a hydrogen gas sensor was proposed [120]. Adapting a sol gel film to spray coating onto a ball to form SAW sensors would require considerable effort; here we show only the capability of fabricating the piezoelectric film on such surfaces.

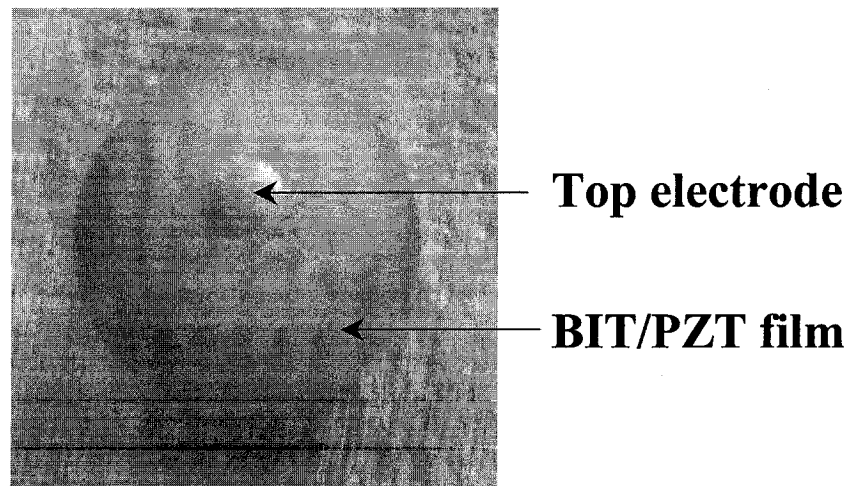
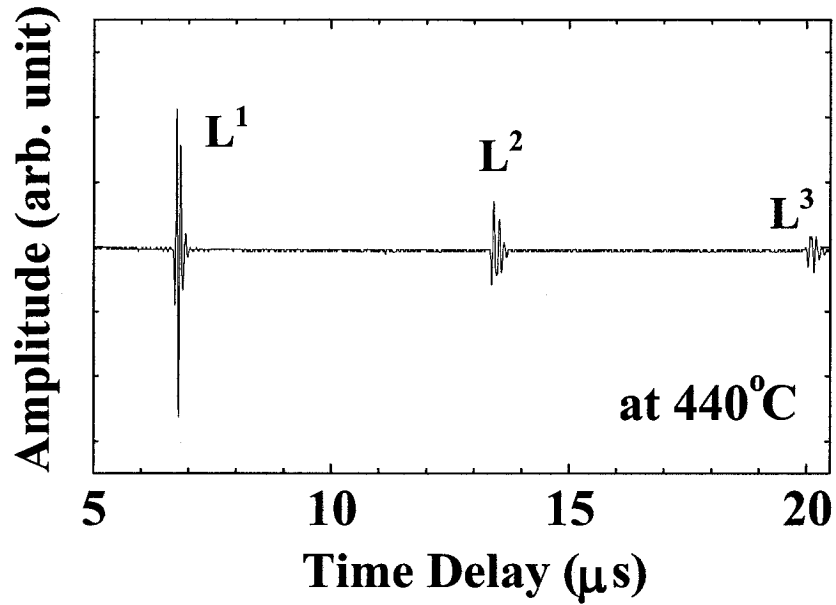
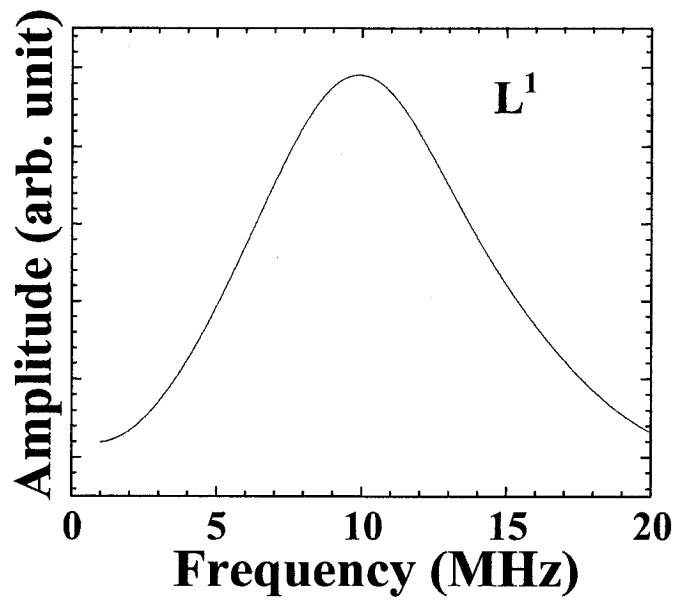


Figure 4.3 A 90 μm thick BIT/PZT film deposited onto a spherical steel ball of 19 mm diameter.



(a)



(b)

Figure 4.4 The ultrasonic performance (a) in time and (b) frequency domain for L^1 at 440°C of the device depicted in Figure 4.3.

4.2.3- Cylindrical and spherical concave surfaces

Figures 4.5 and 4.6 show a 90 μm thick BIT/PZT film deposited onto cylindrical and spherical concave steel surfaces, respectively. For the dimensions of cylindrical concave, the diameter of inner cycle and outer cycle was 20 mm and 26 mm, respectively, and the center angle was 170°. For the dimensions of spherical concave, the curvature and aperture diameter was 19 mm and 19 mm, respectively, and the length was 36 mm. Such structures should be useful for line-focus beam for quantitative measurements and point-focus beam for acoustic imaging [117,121,122] at high temperatures. Ultrasonic performances of these films were almost same as that shown in Figure 4.4 (b).

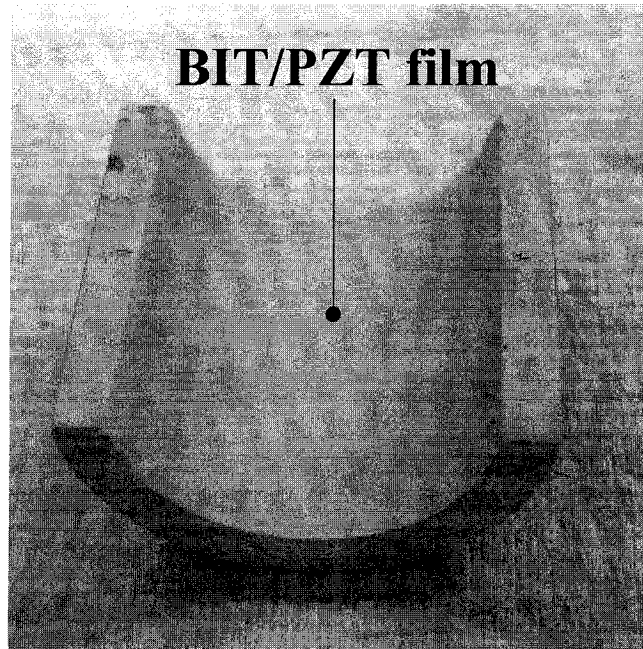


Figure 4.5 A 90 μm thick BIT/PZT film deposited onto a cylindrical concave steel surface.

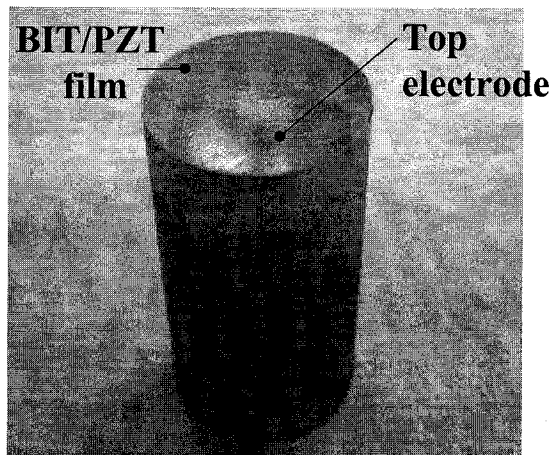
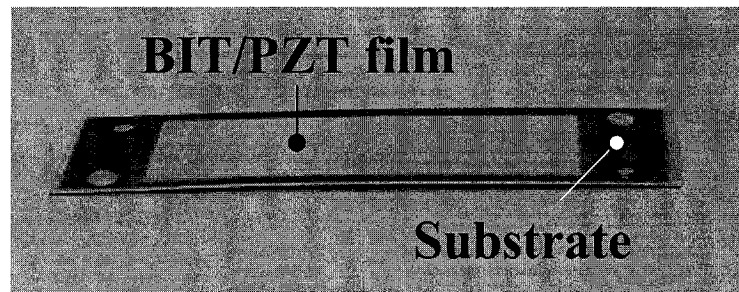


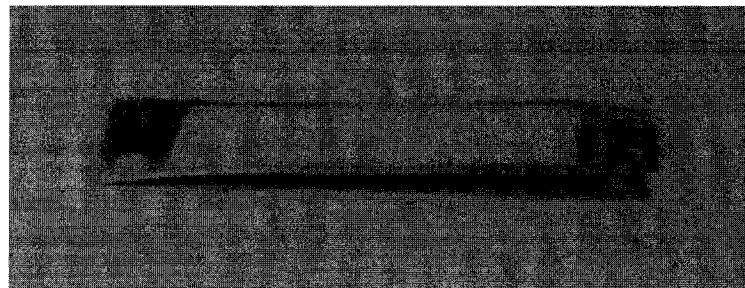
Figure 4.6 A 90 μm thick BIT/PZT film deposited onto a spherical concave steel surface.

4.2.4- Thin metal sheets and foils

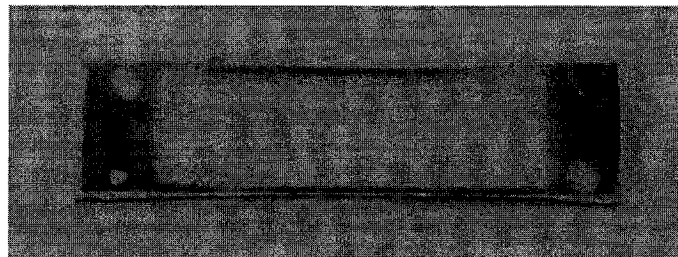
60 μm thick BIT/PZT films were also deposited onto 400 μm thick stainless steel, 75 μm thick titanium, 45 μm thick nickel, and 145 μm thick copper foil substrates, as shown in Figures 4.7 (a), (b), (c) and (d), respectively. Due to the thinness of the substrates and high annealing temperature of BIT/PZT film (650°C), the titanium, nickel and copper films distort somewhat. Structures composed of a thin metal layer and a piezoelectric layer are called unimorphs; the difference in strain between the metal and piezoelectric films induces lengthwise bending when a voltage is applied across the thickness of the piezoelectric layer. Because unimorph structures can produce large displacement with small electrical power, they are suitable for actuator applications [123]. Figures 4.8 shows the ultrasonic performance of the device depicted in Figure 4.7 (a), a 60 μm BIT/PZT film on a 400 μm stainless steel substrate, in time domain at 440°C. Since the substrate is thin, ultrasonic echoes are overlapped. Because of ringing effect, no distinct echo could not be obtained. The center frequency of this film is predicted about 10 MHz. The other films shown in Figure 4.7 have also been tested, but results are similar to Figure 4.8 but not shown here.



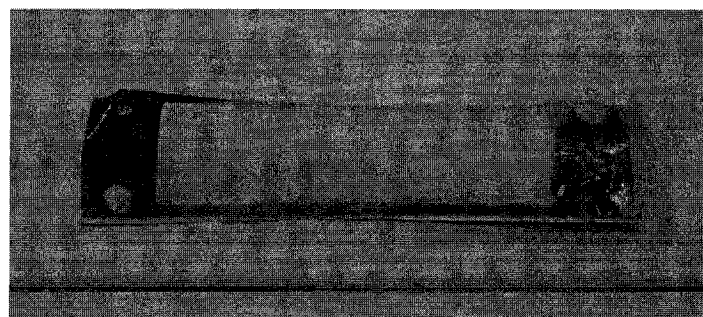
(a)



(b)



(c)



(d)

Figure 4.7 Thick BIT/PZT film deposited on a (a) 400 μm thick stainless steel, (b) 75 μm thick titanium, (c) 45 μm thick nickel and (d) 145 μm thick copper substrate.

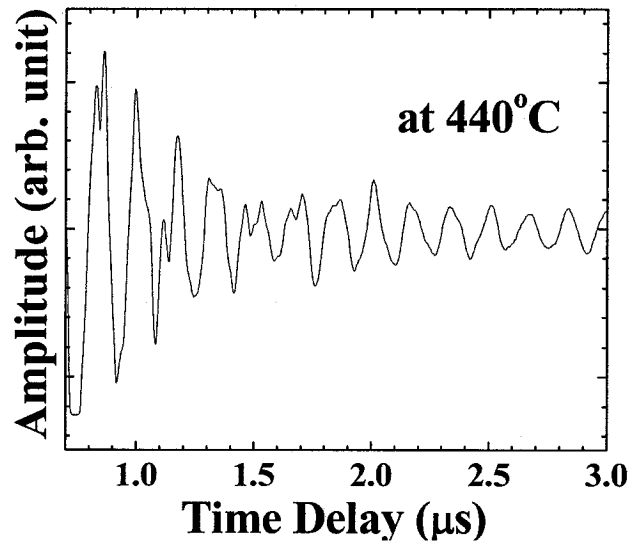


Figure 4.8 Ultrasonic performance of a 60 μm thick BIT/PZT film deposited on a 400 μm thick stainless steel sheet in time domain at 440°C.

4.3- Self-support film

Thin piezoelectric sheet and shells may be of interest for surface bonding or interior embedding for the ultrasonic sensor applications. During the fabrication processes described in Chapter 2, the film may be detached from the substrates if the adhesion between the film and the substrate is too weak to compensate the difference of thermal expansion ratio between them during the thermal treatment. Figures 4.9 and 4.10 show the self-support BIT/PZT films with a flat and spherical convex shape, respectively. The thickness of these films is about 50 μm . To fabricate such self-support films at interface, fine polishing of the substrate surface, thick spray coating and long heat treatment duration were introduced so that no adhesion at interface between film and substrate was formed.

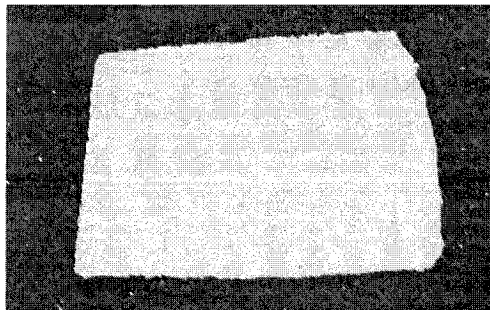


Figure 4.9 Self-support BIT/PZT sheet.

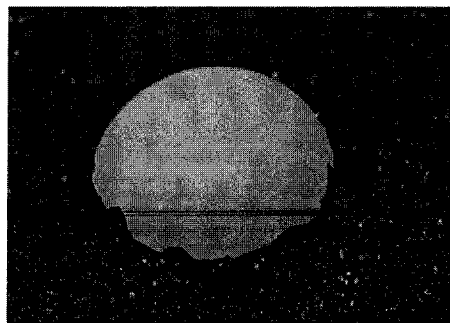


Figure 4.10 Self support BIT/PZT spherical shell.

4.4- NDE of steels at high temperatures

It is well known that ultrasonic sensors are applicable for real-time nondestructive evaluation (NDE) and structural health monitoring. Broadband low MHz UTs are desirable for ultrasonic inspection of defects or voids. In this section, 200 μm BIT/PZT films deposited onto a 12.7 mm thick steel plate for the detection of the extent of artificial horizontal and vertical defects at 440°C will be demonstrated.

Figure 4.11 shows ultrasonic monitoring of an artificial horizontal defect at 440°C. The defect was a side-drilled hole of 1.5 mm diameter. The four traces from top to bottom indicate that the lengths of this artificial horizontal defect are 0, 2, 4, and 6 mm, respectively, under the ultrasonic-exposed area defined by the 11 mm top electrode diameter. The large signal at the end of the trace is the reflected echo from the bottom of the steel substrate. Figure 4.11 reveals that longer horizontal defects produce larger reflected echoes, since the area of the horizontal defect increases. This indicates that the size of the defect in the materials can be estimated at 440°C by BIT/PZT HTUT fabricated by the sol gel spray technique.

Figure 4.12 shows ultrasonic monitoring of an artificial vertical defect at 440°C. The defect was a drilled flat hole of 1.0 mm diameter. The four traces from top to bottom indicate that the lengths of this artificial vertical defect measured from the bottom of the substrate are 0, 1, 2, and 3 mm, respectively, under the ultrasonic-exposed area defined by the 5 mm top electrode diameter. The large signal at the end of the trace is the reflected echo from the bottom of the steel substrate. Figure 4.12 demonstrates that ultrasonic monitoring of the extent of a defect can be performed at 440°C, and the time delay of the signal reflected from the defect reveals the position of the tip of a drilled flat hole. Therefore Figure 4.11 and Figure 4.12 indicate that monitoring of the location of defects in the materials is possible at 440°C by a BIT/PZT HTUT.

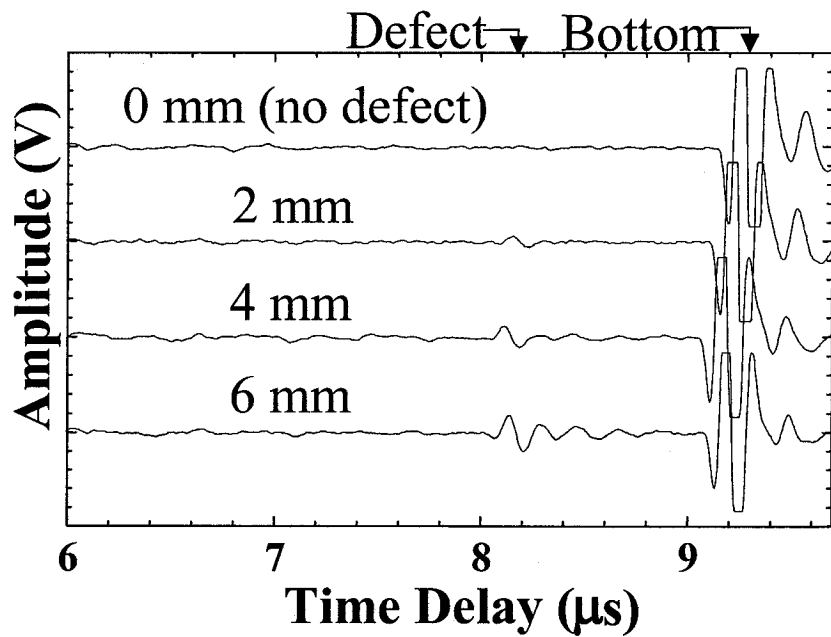


Figure 4.11 Ultrasonic monitoring of an artificial horizontal defect extent at 440°C.

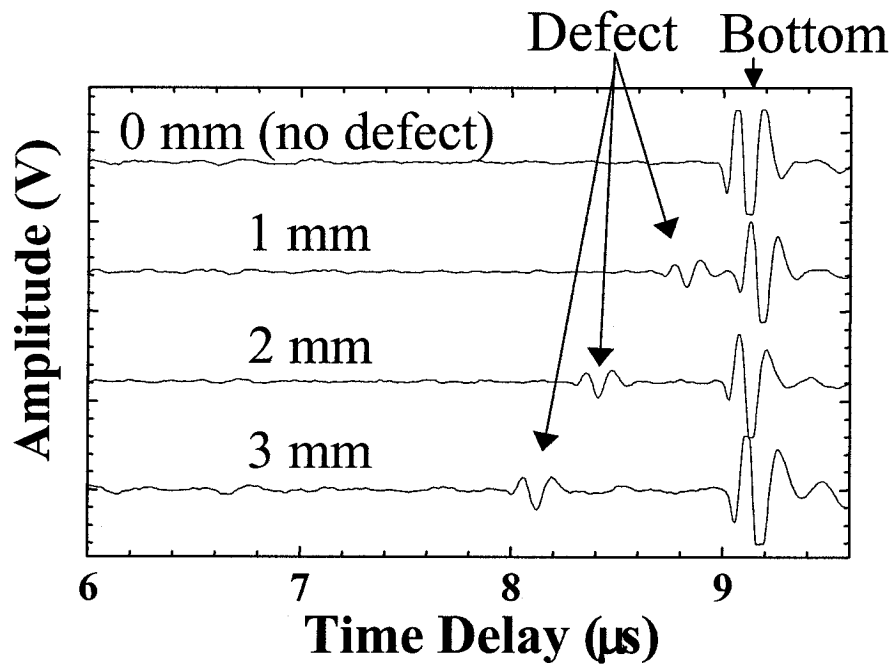


Figure 4.12 Ultrasonic monitoring of an artificial vertical defect extent at 440°C.

Ultrasonic sensors may be useful for aerospace and other engineering systems. Sometimes host structures are large. It has demonstrated previously that the sol gel spray

technique enables the film to be bonded directly to metal substrates; however, there is a size limitation. The most significant concern is the size of the furnace for the film fabrication. In this technique, annealing the film at around 650°C is used to crystallize the sol gel phase, since the high dielectric constant of the sol gel phase is preferred for obtaining high piezoelectricity, as mentioned in Chapter 3. The chamber dimensions of the furnace presently used are 35.56 cm in width, 25.40 cm in height, and 31.75 cm in depth. If the host structure is larger than this size, at present it would be difficult to fabricate a functioning BIT/PZT film on it. In this section, scale-up arrangements are considered for ultrasonic monitoring of substrates which are larger than the dimensions of the furnace described above.

The schematic of the arrangement for ultrasonic monitoring of a large substrate is shown in Figure 4.13. The sensor is first fabricated onto a supporting plate of 5.1 cm long, 2.5 cm width, and 1.2 cm thick, which is small enough for heat treatments in the furnace. Then the plate is attached to a larger substrate with screws and the attachment cover plate with high temperature ultrasonic couplant. When high enough pressure is applied between this supporting plate and a large substrate, ultrasound can propagate into the large substrate from the supporting plate through the high temperature couplant between the plate and substrate. In this experiment, a thin aluminum foil was used as the couplant. The high pressure was applied through the screws shown in Figure 4.13 and Figure 4.14, which shows the real employed experimental arrangement.

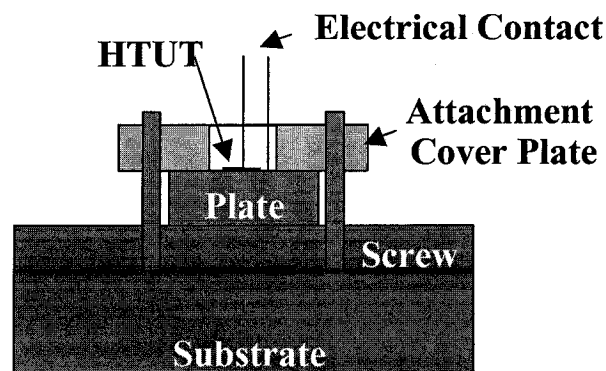


Figure 4.13 Schematic of ultrasonic monitoring for large substrate at elevated temperature.

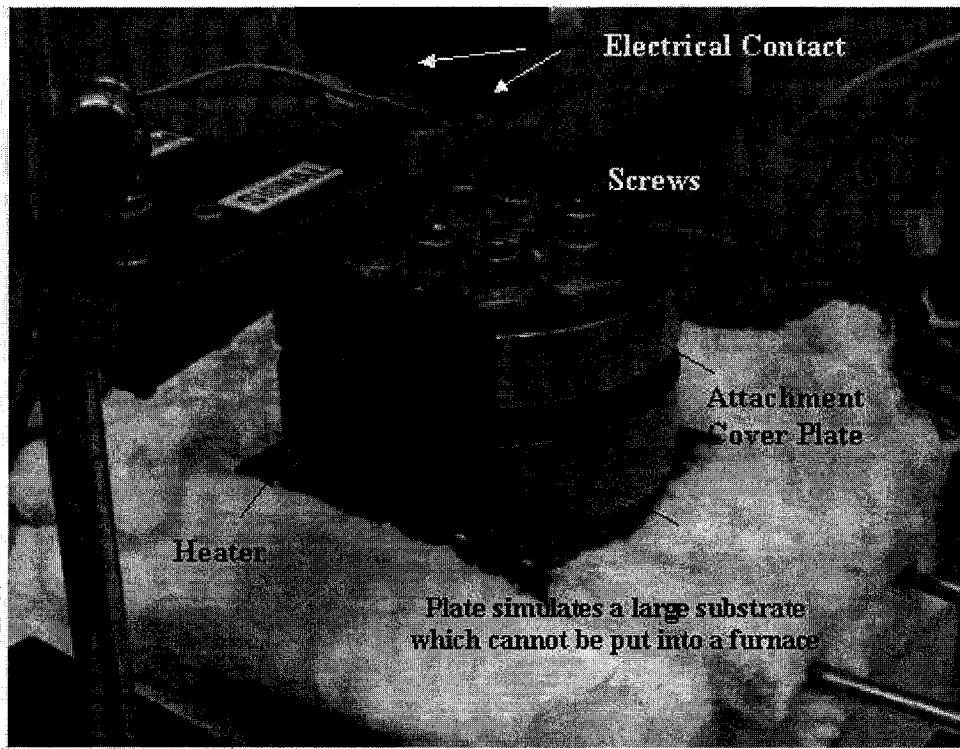
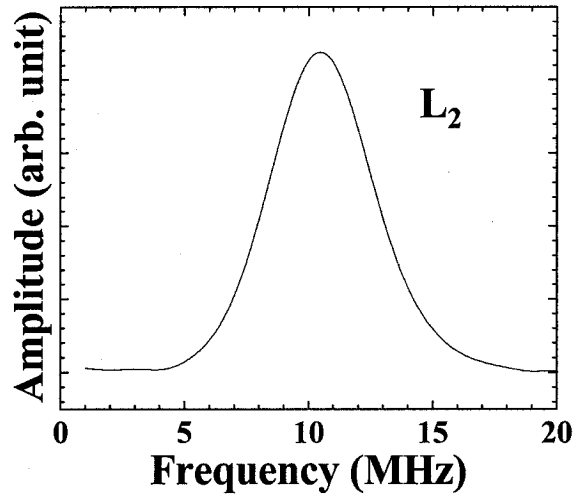
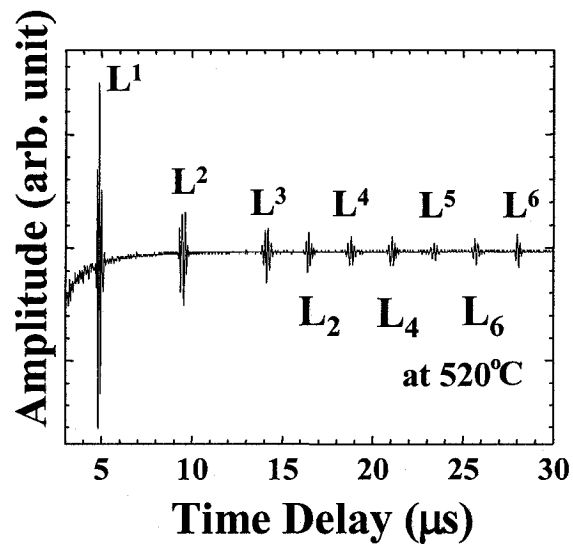


Figure 4.14 Set up of ultrasonic monitoring for a large substrate at elevated temperature.

Ultrasonic measurement results in time domain using this arrangement shown in Figure 4.14 is given in Figure 4.15 (a). In Figure 4.14, the whole setup was sitting on a hot plate and the temperature of the large substrate was 520°C during the measurement. L^n ($n = 1, 2, \dots$) is the n th round trip echo in the supporting plate. Ultrasonic signal reflected from the bottom of the large substrate through the supporting plate, L_2 , was clearly seen. The frequency spectrum of L_2 was given in Figure 4.15 (b) shows the capability of the sol gel sensor for NDE of large metal substrate at high temperatures with good SNR.



(a)



(b)

Figure 4.15 Ultrasonic performance of an 80 μm thick BIT/PZT film deposited on a supporting plate attached to a large substrate in (a) time and (b) frequency domains of L_2 at 520°C.

4.5- Immersion HT ultrasonic thickness measurement and imaging

For applications at nuclear power generation plants [5,6], galvanization plants [7], petrochemical facilities, *etc.*, inspection of hot objects in harsh environments is desirable. HTUTs are essential in order to develop an ultrasonic inspection system that can operate under such severe conditions to achieve high spatial resolution for thickness measurement and for ultrasonic imaging. Since sol gel type HTUTs can operate up to 450°C with high SNR, immersion HT probes are developed. In this section, pulse-echo thickness measurements in molten zinc at 450°C and ultrasonic imaging in silicone oil at 200°C will be demonstrated.

Galvanization is a common technique to prevent corrosion of steel components such as bolts, knots, doors, panels, *etc.* The steel components are dipped into a bath of molten zinc at temperatures of 450-460°C, so that molten zinc can compose thin Fe-Zn alloy layers on surface of parts; then a zinc layer can be composed above the Fe-Zn alloy layers. Ideally the baths of molten zinc are heated uniformly, but in practice the heating is not uniform. In addition, there is a gradual loss of the wall of the molten zinc bath due to a Fe-Zn layer forming on the inside of the bath. Non-uniform heating and the build-up of dross at the bottom of the bath may lead to accelerated corrosion of the bath; therefore the bath must be examined periodically to ensure its safe condition.

Previously an electromagnetic transducer (EMAT) was reported to measure the wall thickness at the external side of the bath [7]. However, the mechanical raster scan of the external surface of the bath for thickness profiling by EMAT can be difficult. Ultrasonic measurement and imaging inside the molten zinc using long buffer rods, have been reported [117]. The UT was outside the molten zinc, cooled by compressed air. However for a large, deep bath, for example, 6 m × 3 m × 1 m, such a long buffer rod may not be suitable.

4.5.1- Immersion HT ultrasonic probe

In this section, a compact immersion HT probe was developed. 8 MHz BIT/PZT HTUTs were fabricated onto a buffer rod, as shown in Figure 4.16; the length of the steel buffer rod was 51 mm. The diameters at the UT and probing ends were 32 mm and 30 mm, respectively. The periphery of the rod had a 2° taper angle from the UT to the probing end, to expedite assembling the rod in a holder. The HT probe was mounted in a stainless steel holder, as shown in Figure 4.17, to seal the HTUT from liquids. This immersion HT probe has the advantage that it can easily scan the inner wall of the bath to obtain a thickness profile inside the molten zinc, which acts as a liquid couplant between the probe and the wall. A coaxial cable made of stainless steel with magnesium oxide insulators was used as an electrical cable, tolerating up to 900°C. Figure 4.18 shows the schematic diagram of the ultrasonic measurement in molten zinc. The immersion type probe was immersed into molten zinc at 450°C. The probe radiates and receives ultrasound with a pulser receiver (5072PR, Panametrics Inc., Waltham, MA). The temperature of molten zinc was controlled by a temperature controller with an immersed thermocouple. Ultrasonic signals were recorded using a data acquisition board (CS12100, Gage Applied Science Inc., Lachine, QC, Canada). To measure thickness, a 24.5 mm-thick steel sample was also immersed. A stainless steel crucible containing zinc was heated by an electric resistance furnace.

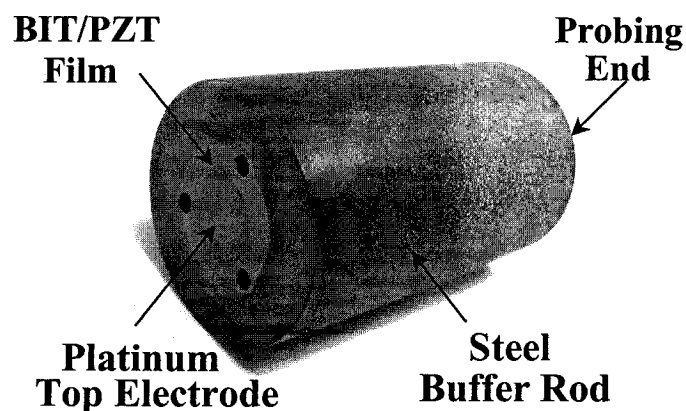


Figure 4.16 HT ultrasonic probe consisting of a BIT/PZT HTUT fabricated onto a steel buffer rod.

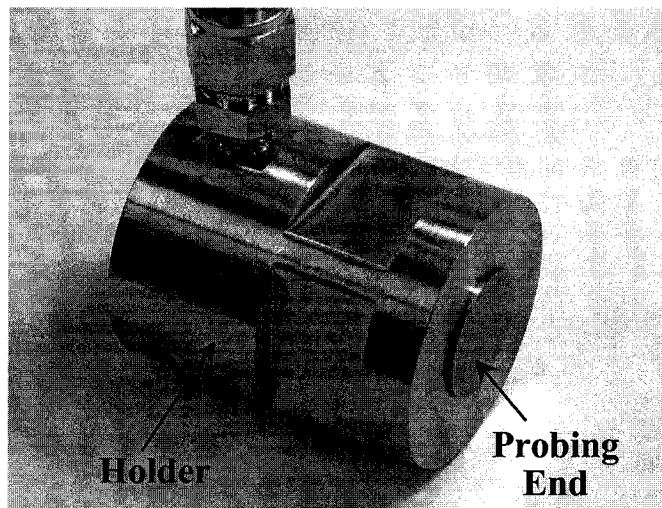


Figure 4.17 HT immersion type ultrasonic probe with a holder.

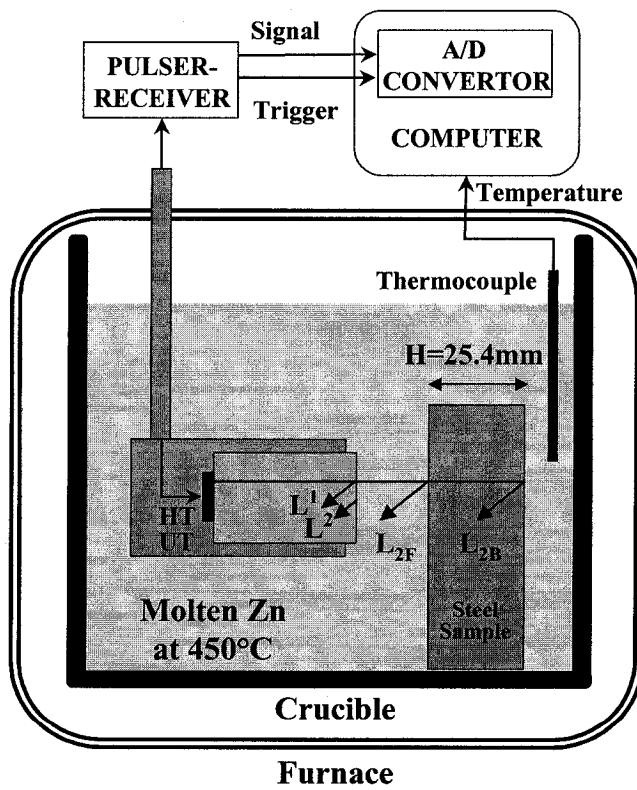


Figure 4.18 Schematic diagram of ultrasonic thickness measurement in molten zinc at 450°C.

4.5.2- Ultrasonic thickness measurement in molten zinc

The result of the thickness measurement in molten zinc at 450°C is given in Figure 4.19. L^n ($n = 1, 2, \dots$) denotes n th round trip echo in the 51 mm long steel buffer rod. Two echoes, indicated by L_{2F} and L_{2B} in Figure 4.19, which were echoes reflected from the front and back surfaces of the sample, respectively, were clearly obtained as shown in Figure 4.19. Therefore the thickness of the wall of the galvanization bath could be profiled, because the thickness of the steel sample, t , can be calculated by $t = v \times \Delta T / 2$, where v is the longitudinal ultrasonic velocity in steel at 450°C, obtained empirically or from the literature, and ΔT is the time delay between L_{2F} and L_{2B} . This steel probe was immersed in the molten Zn for many hours and the probing surface was only slightly corroded after even 9 hours. It means that the surface remained acceptably flat during the experiment. In fact, when this probe was placed facing the SS container, the wall thickness of the SS container could be measured as well.

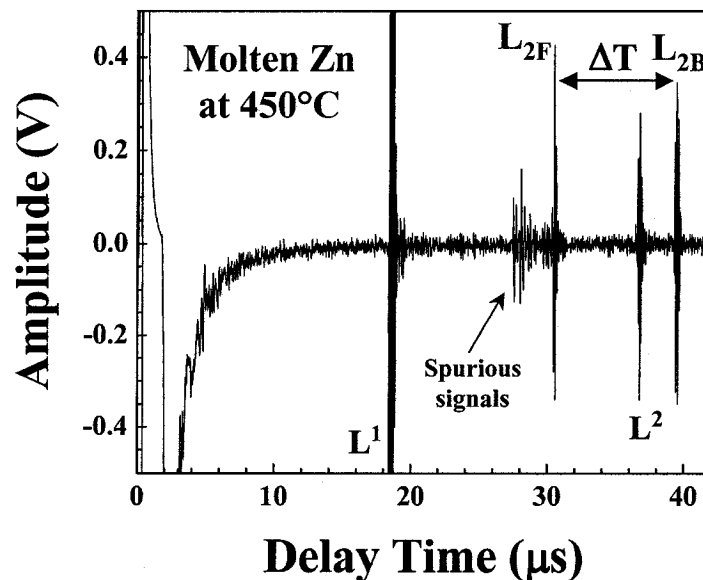


Figure 4.19 Ultrasonic signals for thickness measurement in molten zinc at 450°C.

4.5.3- Ultrasonic imaging in silicone oil at 200°C

Imaging at elevated temperatures is demonstrated here to show the high spatial resolution of an immersion HT ultrasonic probe with focusing lens at the probing end. The probing end of the 8 MHz immersion HT probe was machined into a semi-spherical surface as an ultrasonic lens, as shown in Figure 4.20. This focused probe was 50 mm long. The radius of curvature and aperture diameter of the lens were 11 mm and 15 mm, respectively.

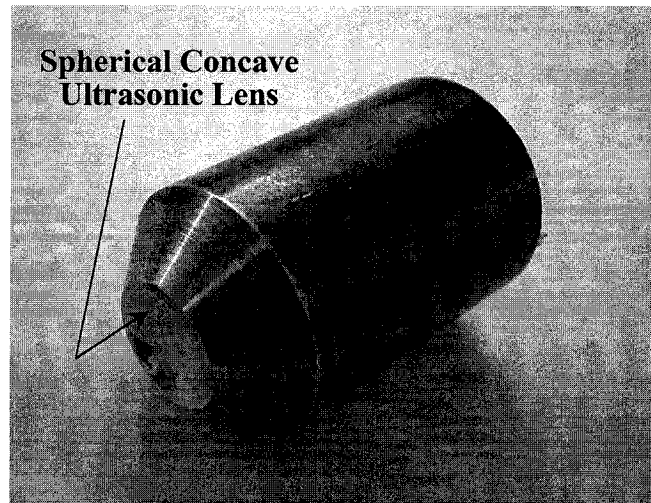


Figure 4.20 HT probe with an ultrasonic lens.

The experimental set-up is shown in Figure 4.21. The HT focusing probe was mounted on a manual vertical-translation stage (Z-stage) to adjust the distance between the probing end and the sample, and manipulated horizontally using an XY-stage driven by stepping motors. A crucible furnace (Model CF 56822C, Lindberg, NC, USA) heated the silicone oil in a stainless steel crucible. A US one cent coin was polished on the back head side to serve as a scanned sample for surface and subsurface imaging, and fixed on the sample holder. The sample photo is shown in Figure 4.22. The line thickness of the smallest characters (“E · PLURIBUS · UNUM”, the part of the phrase with Latin, “IN GOD WE TRUSTTIE PLURIBUS UNUM”) on the coin was about 0.2mm. The

temperature of the silicone oil was controlled and maintained at $200^{\circ}\text{C} \pm 1^{\circ}\text{C}$ using a temperature controller with a thermocouple.

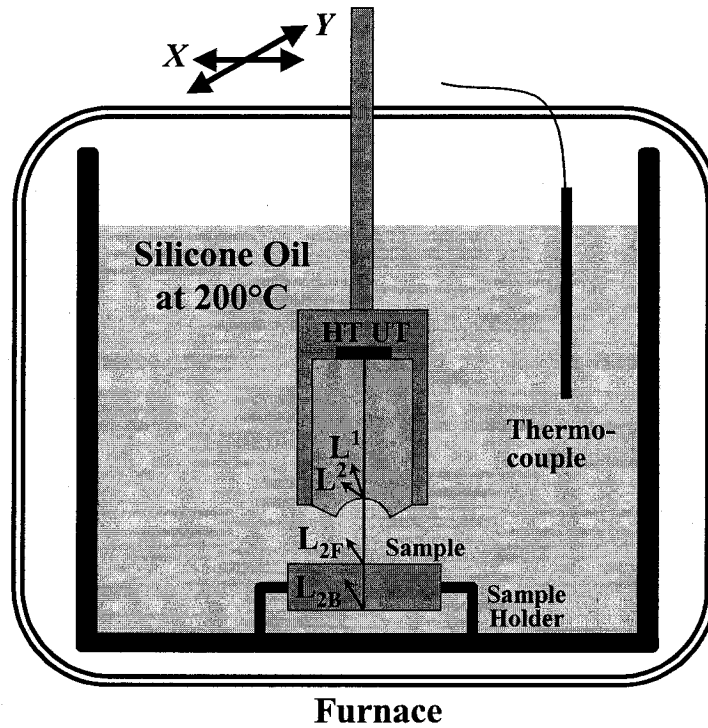


Figure 4.21 Ultrasonic imaging set-up.



Figure 4.22 American one cent coin used for imaging experiments. The tail side had its figures but the head side was polished to be flat.

The focusing ability of ultrasound was evaluated in water at room temperature, and in silicone oil (200 Fluid-100 cst, Dow Corning, Midland, Michigan) at 200°C, using this immersion HT ultrasonic probe at a frequency of 10 MHz, to estimate spatial resolution for surface imaging. The lateral resolution dr and focusing depth dz are estimated using the following equations [124]:

$$dr \cong 1.02\lambda \cdot \frac{l}{a} \quad (5.5)$$

$$dz \cong 7.1\lambda \cdot \left(\frac{l}{a}\right)^2 \quad (5.6)$$

where λ is the wavelength of ultrasound in liquid, l is the focal length and a is the aperture diameter of the lens. λ and l are calculated by $\lambda = v_{liquid} / f$ and $l = r / (1 - v_{liquid} / v_{steel})$, respectively, where v is longitudinal wave velocity and r is the curvature radius of the lens. The calculated results are summarized in Table 4.1. The v_{liquid} for water and v_{steel} at 23°C are 1491 m/s [125] and 5923 m/s [126], respectively. At 200°C, the v_{liquid} for silicone oil was estimated to be 612 m/s empirically using the time delay of the signals reflected from the sample surface at the focus of the lens, and the v_{steel} is 5843 m/s [126]. Due to the lower ultrasonic velocity in silicone oil at 200°C than that in water at 23°C, the higher spatial resolution is expected in silicone oil at 200°C.

Table 4.1 Calculated results of the focusing ability of ultrasound.

	In water at 23°C	In silicone oil at 200°C
dr	0.19 mm	0.065 mm
dz	1.31 mm	0.38 mm

Figure 4.23 (a) shows the time domain signals obtained when the front surface of the sample was located at the focus of the probe in water at room temperature. The first and second round trip echoes of longitudinal waves in the rod, indicated by L^1 and L^2 , were observed at time delays of about 16 μs and 32 μs , respectively. Echo L^{2F} represents the desired signal for surface imaging, reflected from the front surface of the sample. Spurious signals are caused by the semi-spherical surface of the lens, which produces different ultrasonic wave path lengths. The L_{2F} shown in Figure 4.23 (a) had enough SNR for constructing ultrasonic images in water at room temperature.

The signals obtained in silicone oil at 200°C when the front surface of the sample was located at the focus of the lens is presented in Figure 4.23 (b). The L^3 observed at 48 μs was the third round trip echo in the rod. The L_{2F} signals indicated in Figure 4.23 (b) were about 20 dB smaller than those in water at room temperature. This is due to the facts that the ultrasonic attenuation in silicone oil at 200°C is significant and also the acoustic impedance mismatching between the steel rod and silicone oil (200°C) is larger than that between the steel rod and water (24°C), resulting in less transmission of ultrasonic energy from the rod into silicone oil than into water. In addition, the spurious signals in silicone oil at 200°C shown in Figure 4.23 (b) were much larger than those in water shown in Figure 4.23 (a) because of the 20 dB larger electronic amplification of the signals than in water, which reduce the SNR of the L_{2F} . However amplitude and time delay of these spurious signals are fixed at a constant temperature because they are mainly echoes reflected inside the rod. Therefore, such spurious signals can be eliminated by subtracting background signals measured without the sample from the signals measured with the sample by digital signal processing techniques. In the following imaging experiments, the data after subtraction are presented. It is noted that the attenuation of ultrasound in the steel rod at 200°C is negligible because the probe was operated at 450°C and the signal strength of the L^1 at 450°C was only 1.5 dB smaller than that at 22°C.

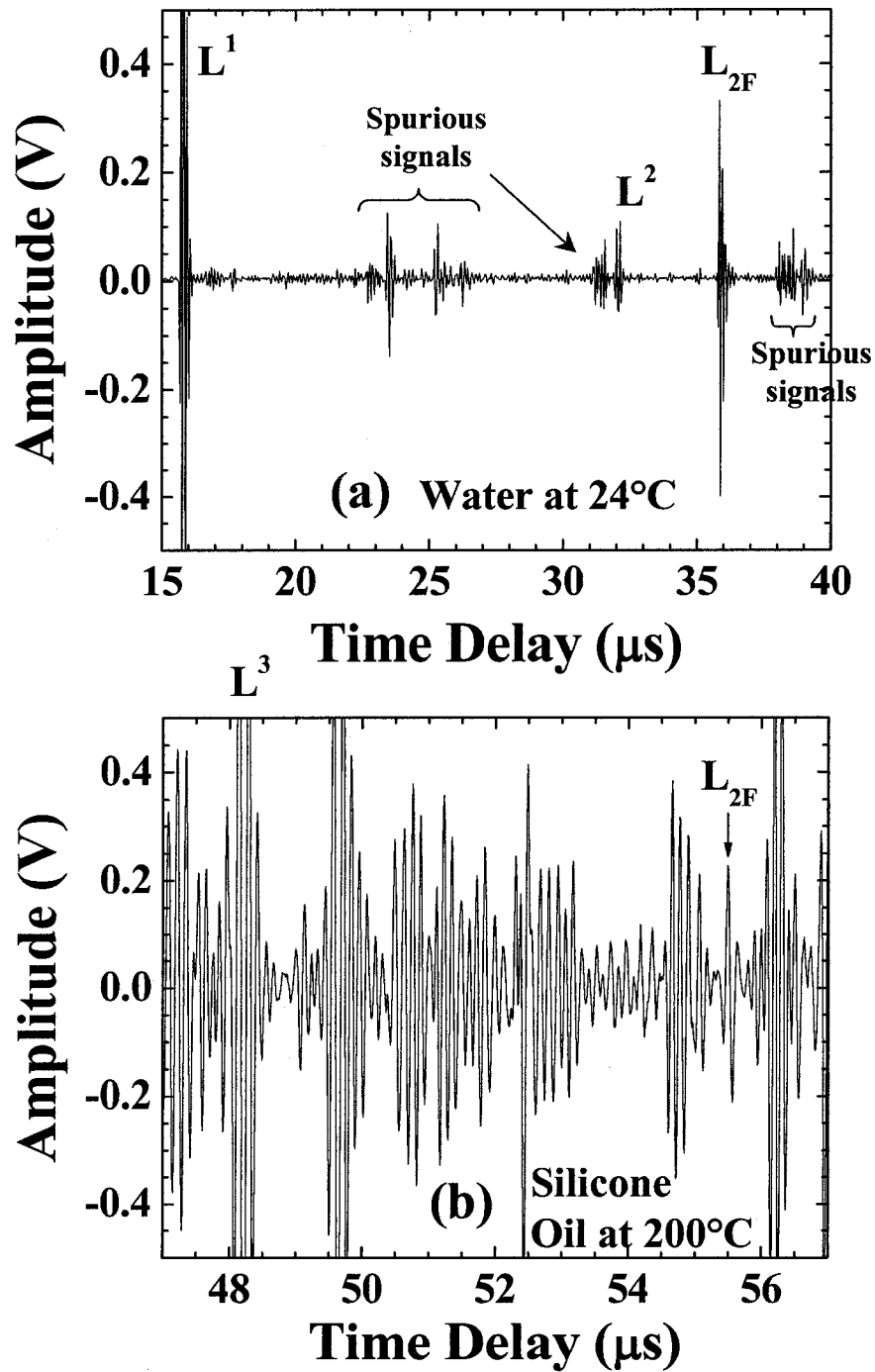


Figure 4.23 Ultrasonic signals from the rod and the sample (a) in water at room temperature and (b) in silicone oil at 200°C.

The imaging experiment was first carried out in water at room temperature, then in silicone oil at 200°C using the same probe and sample. Figure 4.24 (a) and (b) show the used signals for surface imaging, L_{2F} , reflected from the front surface of the sample in water at 24°C and in silicone oil at 200°C, respectively. Figures 4.25 and 4.26 show ultrasonic images derived in water at room temperature and in silicone oil at 200°C, respectively. Scan step was 100 μm for XY raster scan. The figures were constructed from the amplitude or time delay of the echoes from the sample surface; darker color shows larger amplitude, or longer time delay. The images of the figures including the characters having 0.2mm-thickness on the one cent coin were clearly observed. Slight deformation of the images was caused by movement errors of the XY -stage used in this experiment.

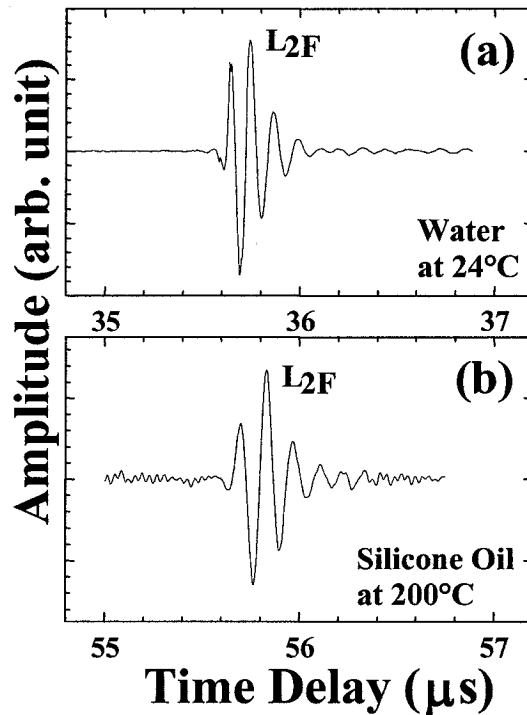


Figure 4.24 Ultrasonic signals obtained when a front surface of the sample is at focus of the lens (a) in water at room temperature and (b) in silicone oil at 200°C.

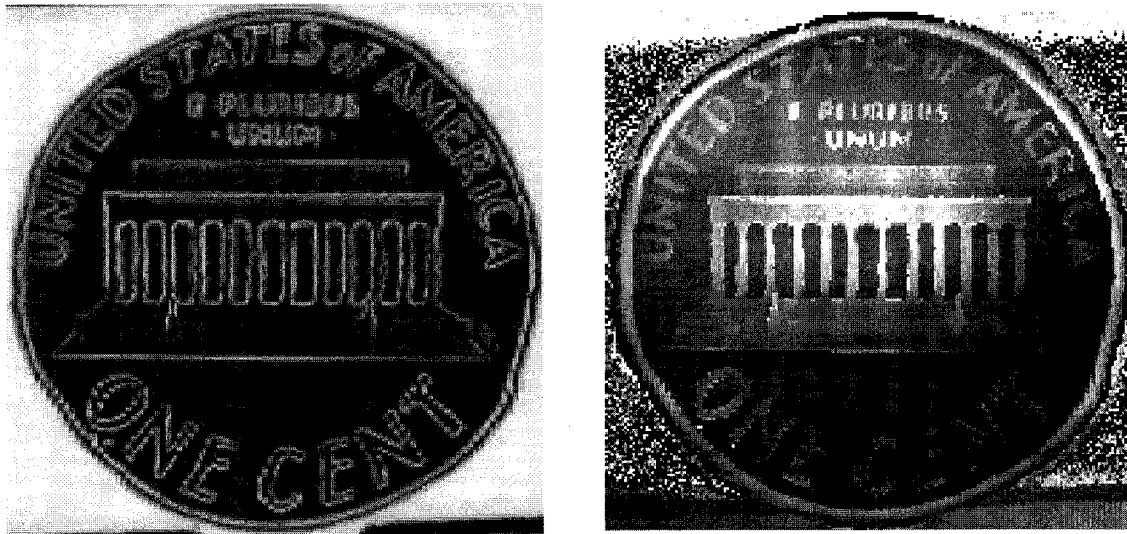


Figure 4.25 Ultrasonic images of a US coin in water at room temperature, obtained by plotting (a) the amplitude and (b) the time delay of the echo.

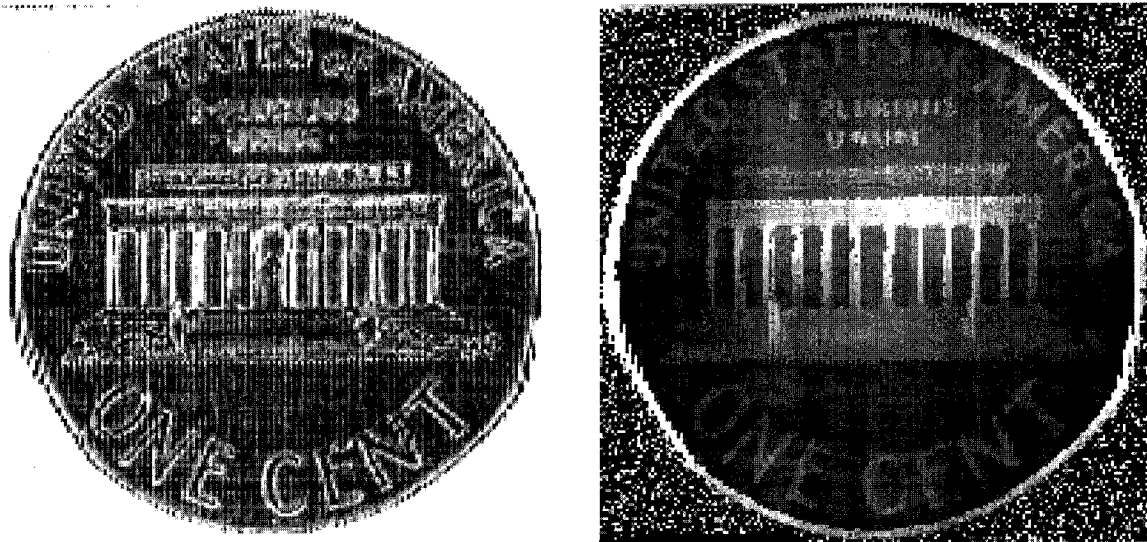


Figure 4.26 Ultrasonic images of a US coin in silicone oil at 200°C, obtained by plotting (a) the amplitude and (b) the time delay of the echo.

In order to investigate the performance of the HT probe for inspecting defects inside materials, experiments for sub-surface imaging were carried out. The same sample

and experimental set-up as in Figure 4.21 were used again, except that the sample was face-down for sub-surface imaging. Figure 4.27 (a) and (b) show the ultrasonic signals reflected from the back surface of the sample in water at room temperature and in silicone oil at 200°C, respectively. In addition to the L_{2F} reflected from the front surface of the sample, the signals reflected from the back surface of the sample (L_{2nB}) were observed in water and in silicone oil, where the L_{2nB} ($n=1,2$) indicates the n -th round trip signals in the sample.

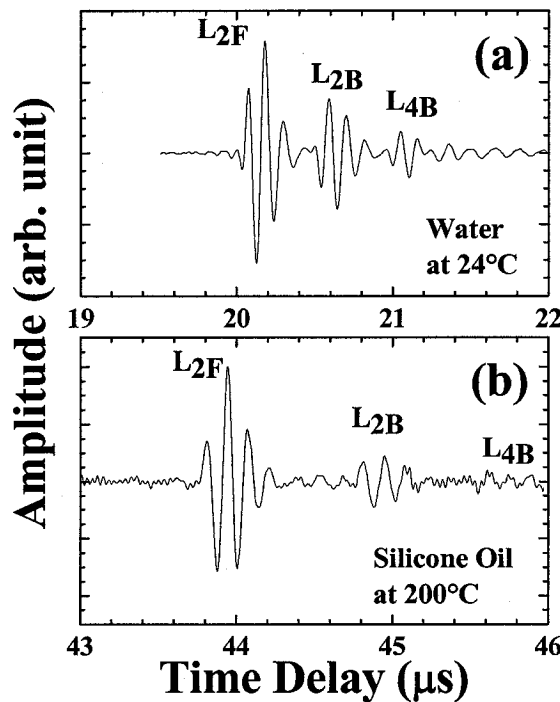


Figure 4.27 Ultrasonic signals obtained when a back surface of the sample was at focus of the lens (a) in water at room temperature and (b) in silicone oil at 200°C.

Figure 4.28 and Figure 4.29 show the ultrasonic sub-surface images measured in water at room temperature and in silicone oil at 200°C, respectively. The sub-surface features of the image of the US one cent coin were observed. The sub-surface images in silicone oil at 200°C were not clear due to insufficient SNR. The imaging quality could be improved by modifying the lens design shown in Figure 4.20, fabricating cladding layers on periphery of the rod [117], and impedance matching layer at the lens-silicone oil interface [127]. All of these steps could increase the SNR of the probe.

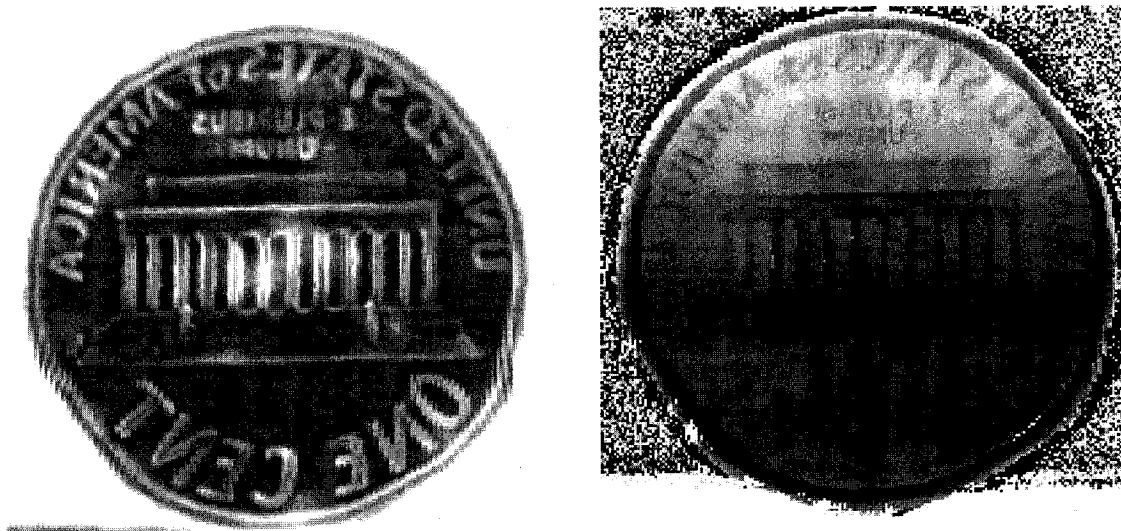


Figure 4.28 Ultrasonic sub-surface images of US coin in water at room temperature, obtained by plotting (a) the amplitude and (b) the time delay of the echo.

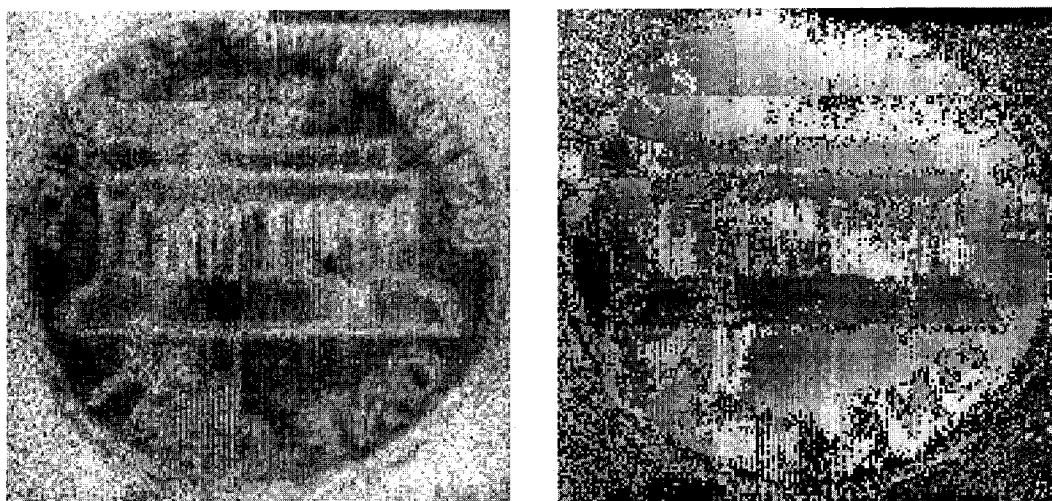


Figure 4.29 Ultrasonic sub-surface images of US coin in silicone oil at 200°C, obtained by plotting (a) the amplitude and (b) the time delay of the echo.

4.6- Summary

BIT/PZT films fabricated by the sol gel spray technique were deposited on various substrates to demonstrate the capability of realizing NDE of metallic structures at high temperature. These films with thickness ranging from 40 μm to 200 μm were also successfully coated directly on substrates, such as steel, stainless steel, titanium, nickel and copper substrates, with planar, spherical concave and convex, and cylindrical concave and convex surfaces, and thin sheets or foils. Ultrasonic measurements using the films fabricated onto cylindrical and spherical convex surfaces were performed at 440°C. Flat and curved self-supported films were also successfully fabricated. The capability of ultrasonic monitoring of the extent of the artificial horizontal and vertical defects in steel substrates at 440°C was also presented. An ultrasonic measurement setup for NDE of large metallic substrates at high temperature was demonstrated. A supportive steel plate was firmly attached to a large steel substrate through screws which exerted high pressure between them. Ultrasonic signal generated by the BIT/PZT UT successfully passed the supportive substrate, the aluminum foil couplant and reflected from the bottom of the large steel substrate, and then received by the same UT at 520°C.

Ultrasonic measurement of the thickness of a steel plate was successfully demonstrated with the probe fully immersed in molten zinc at 450°C. Ultrasonic surface and sub-surface imaging in water at room temperature and in silicone oil at 200°C were also carried out. The scanned ultrasonic surface and sub-surface images taken by the fully immersed focused probe show good resolution.

Chapter 5

Applications of sol gel composite HTUTs for on-line ultrasonic monitoring of polymer process

5.1- Introduction

Ultrasound is capable of real-time monitoring of material properties and processing conditions by penetrating barrels, molds. It has been proven in previous chapters that BIT/PZT films fabricated by sol-gel based spray coating can operate at temperatures up to more than 450°C with high SNR, up to 40 dB in the pulse-echo mode, 2-30 MHz operating frequency and broad bandwidth. Since plastics manufacturing processes are usually carried out at elevated temperatures, the UTs for polymer process monitoring must withstand the required temperatures continuously. Since these HTUTs can be fabricated directly onto even curved surfaces such as barrels of extruder machine in a non-intrusive manner, they can be a preferable choice for monitoring. In addition, couplant is not required and this is beneficial for continuous monitoring.

In this chapter, BIT/PZT and LT/PZT films fabricated by sol gel based spray coating are used because of high operating temperatures. Applications for the real-time monitoring of polymer extrusion, injection molding and micro-molding are demonstrated by using a real industrial machine.

5.2- Polymer extrusion: Barrel and screw status

Polymer extrusion is one of the most common industrial material processing techniques in the plastic industry. The standard set-up includes an extruder and a die. The polymer is fed into the extruder in the form of pellets through a hopper. Then it is melted and transported along the barrel through various zones, such as solid conveying, melting, mixing and pumping. Finally, polymer melt flows through a die where it forms the desired shape of the product [30].

In this section, ultrasonic real-time monitoring of barrel wear and screw status was attempted with LT/PZT and BIT/PZT films, to demonstrate their capability. The conditions of barrels and screws are important to polymer extrusion [24-26]. Once screw or barrel wear occurs, the clearance between threads of the extruder and the barrel increases; as a result, production rate decreases because the melt in the barrel cannot be transported efficiently. There are four basic mechanisms for wear: adhesion, abrasion, corrosion and delamination. The wear may come from abrasion by abrasive materials such as glass-fiber reinforced polymers; chemical corrosion resulted from, for example, degradation of polyvinyl chloride (PVC) releasing hydrogen chloride, and erosion, etc. Careful maintenance of the equipment and proper selection of screw and barrel can reduce wear. However, screw and barrel wear is inevitable, and the extrusion efficiency decreases rapidly with increasing clearance, following a cubic relationship [28]. Usually the screw and barrel are examined periodically, for example, every few months. This involves first shutting down the operation, removing and cleaning the screws, and then manually measuring the size of individual screw and barrel elements. In order to maintain a high production rate, real time monitoring of screw and barrel status is preferable, to prevent costly, unnecessary shutdowns and deterioration of production efficiency and quality before any serious production problem occurs.

For demonstration purpose, two sol gel based sprayed LT/PZT and BIT/PZT HTUTs were deposited onto the top external surface of an extruder adaptor made of H13

steel, which is commonly used as barrel material. HTUTs can be fabricated at desired locations through a shadow mask. A schematic diagram for the ultrasonic wave propagation in a pulse/echo mode is shown in Figure 5.1. UTs mounted on the external surface of the barrel adaptor generate ultrasonic waves. The ultrasonic waves propagate into the barrel to its inner wall. The ultrasonic energy is partly reflected at the barrel inner wall/molten polymer interface, and partly transmitted to the molten polymer, and then reflected either by the flight or the root of the screw. Echoes are denoted by L^1 , L_{2F} and L_{2R} in Figure 5.1 respectively; echoes L^2 , L^3 , L_{4F} , L_{6F} , L_{4R} and L_{6R} represent further round trip echoes in the corresponding media. The same UT receives the returned echoes. This technique is non-intrusive to the barrel. It is also non-destructive to the polymer melt, since the average ultrasonic energy is only on the order of ten mill watts. Experimental data obtained during extrusion of low-density polyethylene (LDPE) and high-density polyethylene (HDPE) on a Werner & Pfleiderer (W&P) 30-mm twin-screw extruder are presented.

Barrel wear δt_B , the reduction in the thickness of the barrel wall t_B with respect to that of an un-worn one, can be measured as [57],

$$\delta t_B = t_{B0} - t_B = t_{B0} - v_{LB} \cdot \Delta t_B / 2 \quad (5.1)$$

where t_{B0} is the nominal barrel thickness, v_{LB} is the ultrasonic longitudinal velocity in the barrel, and Δt_B is the time delay between echoes L^1 and L^2 , as seen in Figure 5.1. v_{LB} is a function of temperature, pressure and composition of the barrel steel. From reference [146] and unpublished data at IMI, v_{LB} in barrel steel is around 6000 m/s at room temperature. The velocity change is nearly 1 m/s per °C when temperature is below 400°C, higher than the highest barrel temperature during polymer extrusion.

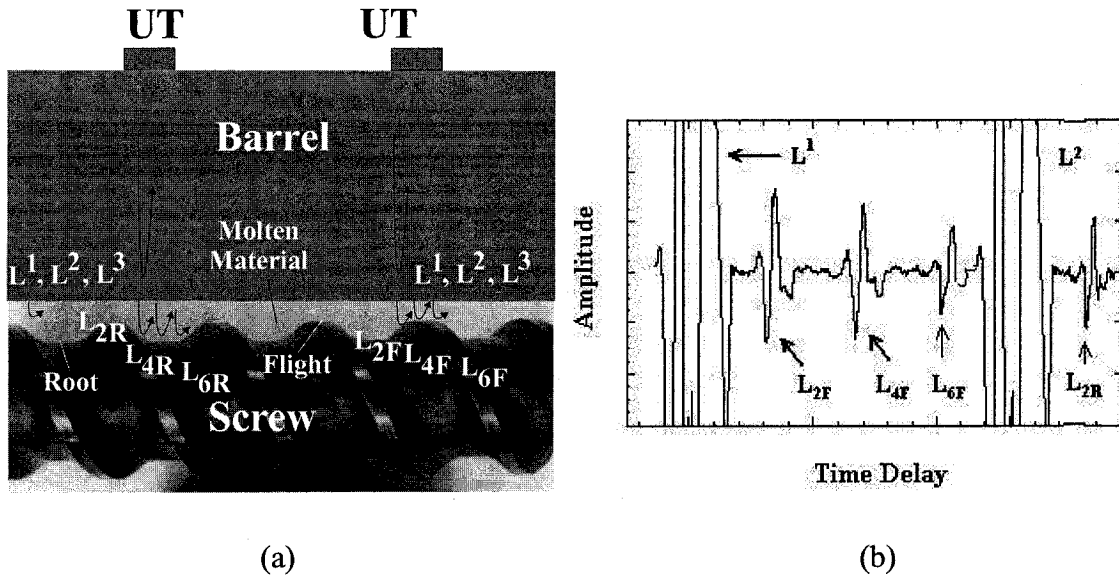


Figure 5.1 (a) A schematic diagram of the ultrasonic waves propagating in the extruder barrel and polymer melt and (b) the example of the echoes.

In cases where the barrel wall is worn but there is no screw misalignment, the screw wear δt_{p_screw} can be determined as [57],

$$\delta t_{p_screw} = \langle t_p \rangle - t_{p0} - \delta t_B = v_{LP} \cdot \langle \Delta t_p \rangle / 2 + v_{LB} \cdot \Delta t_B / 2 - t_{p0} - t_{B0} \quad (5.2)$$

where $\langle \rangle$ represents an average over a certain observation time in order to eliminate the effect of screw deflection, t_p is the distance between the barrel wall and screw flight, t_{p0} is the nominal barrel/screw clearance, v_{LP} is the longitudinal velocity in the polymer melt, and Δt_p is the time delay between echoes L_{2F} and L_{4F} , as shown in Figure 5.1. It should be noted that only screw flight wear is considered. In practice, screw wear is much severe at the flight than at the root, and has the most dominant impact on production. v_{LP} is a function of temperature and pressure. Empirically most polymer melts exhibit similar rates of change. Velocity *versus* temperature and pressure for the polypropylene melt is about 2 m/s per °C and 4.4 m/s per 100 psi, respectively [14]. In the following section, LT/PZT and BIT/PZT HTUTs are demonstrated for barrel wear and screw status measurements.

The cross-correlation method was used as a signal processing procedure to obtain time delay precisely. The correlation of two signals, $w_1(t)$ and $w_2(t)$, denoted $\text{Corr}(w_1(t), w_2(t))$, is defined by [128],

$$\text{Corr}(w_1(t), w_2(t)) \equiv \int_{-\infty}^{\infty} w_1(\tau + t)w_2(\tau)d\tau \quad (5.3)$$

When $w_1(t) \neq w_2(t)$, the correlation is called a cross-correlation, a function of time, with a maximum corresponding to the two signals, $w_1(t)$ and $w_2(t)$. The *correlation theorem* says that this correlation of two real signals is one member of the Fourier transform pair [128]

$$\text{Corr}(w_1(t), w_2(t)) \Leftrightarrow W_1(\omega)W_2^*(\omega) \quad (5.4)$$

where $W_1(\omega)$ and $W_2(\omega)$ are Fourier transforms of $w_1(t)$ and $w_2(t)$, and the asterisk denotes complex conjugation. Cross-correlation can be computed using the Fast Fourier Transform (FFT) algorithm. By inverse transformation, it is possible to obtain a maximum function value in the time domain, corresponding to the time delay between two signals.

Figure 5.2 shows four LT/PZT films deposited on the top external surface of an extruder adaptor [27]. Two platinum top electrodes, which were made by the vacuum sputtering technique and define the active area of the HTUT, are aligned with screws underneath. Spring-loaded HT electrical contacts were used to contact the top and bottom electrodes; the bottom one is the steel adaptor itself. The actual setup in a W&P 30-mm twin-screw extruder is shown in Figure 5.3. The monitored screw element was a 28/28 RH bushing in the pumping zone; the extruded material was LDPE. The average barrel temperature, surface temperature of the external adaptor, and melt pressure at the monitored area, were about 200°C, 190°C and 1000 psi, respectively.

Observed signals reflected from the barrel/molten polymer interface are shown in Figure 5.4. The center frequency is around 18 MHz. Figure 5.4 clearly indicates good L¹

and L^2 signals; therefore barrel wear can be measured. From these measurements it was found that the frequency is too high and the piezoelectric strength of LT/PZT film was not sufficient to see signals reflected from the screw, for screw status monitoring. Therefore, BIT/PZT films were developed and used to replace LT/PZT film HTUTs.

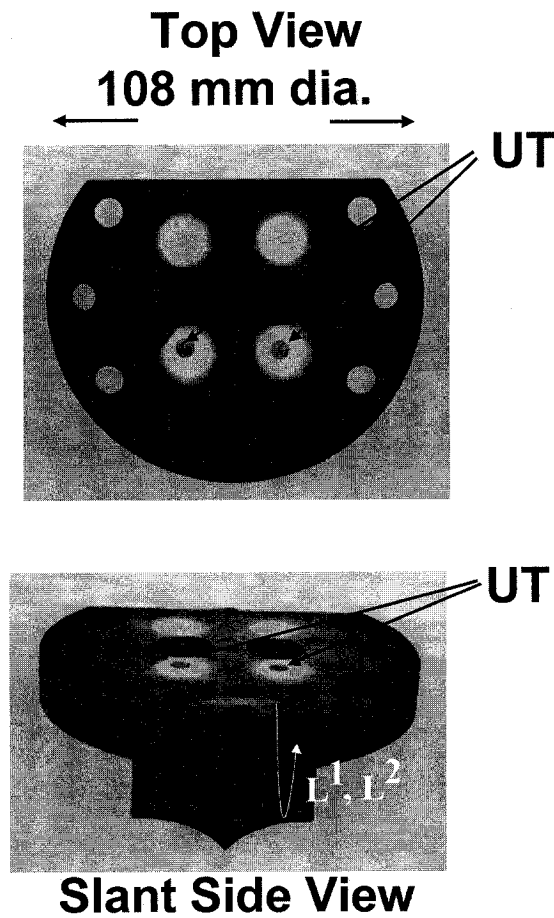


Figure 5.2 Four LT/PZT UTs deposited on the top surface of an extruder barrel adaptor.

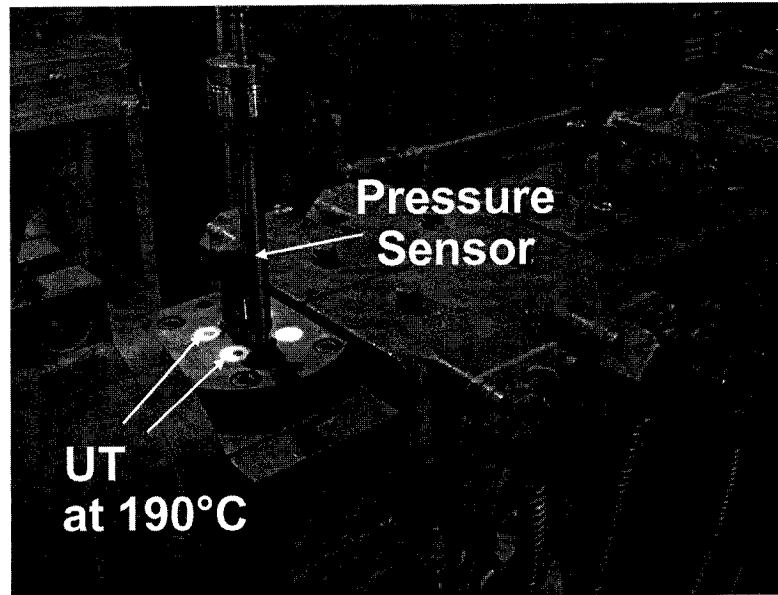


Figure 5.3 LT/PZT UTs on the top surface of an extruder barrel adaptor in a W&P 30-mm twin-screw extruder.

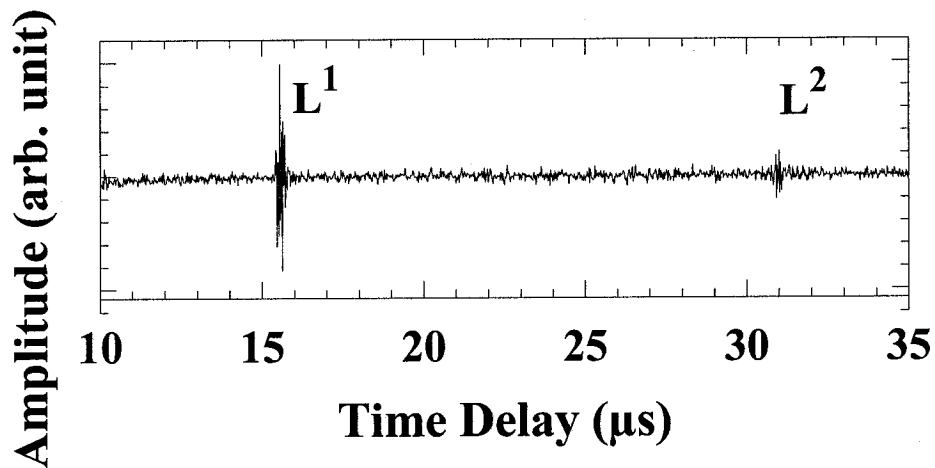


Figure 5.4 Echoes reflected from the extruder barrel adaptor/molten polymer interface.

Figure 5.5 shows BIT/PZT films deposited on the top external surface of an extruder adaptor [57]. Three 11 mm diameter silver paste top electrodes, which define the active area of the HTUT, were coated and aligned with screws underneath. Spring-loaded HT electrical contacts were used to contact the top silver paste and bottom electrodes and the bottom one is the steel adaptor itself. The monitored screw element was a 20/20 RH bushing in the pumping zone. The extruded material was HDPE. The average barrel

temperature, surface temperature of the external adaptor, and melt pressure at the monitored area were about 200°C, 190°C and 1000 psi, respectively.

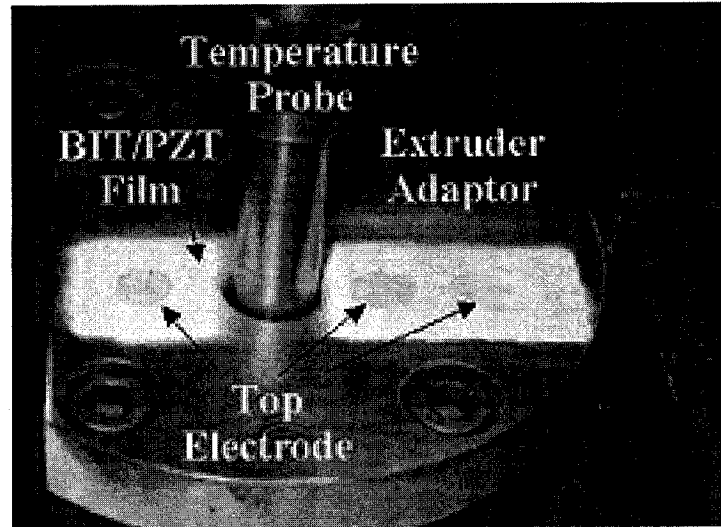


Figure 5.5 Sol gel sprayed BIT/PZT HTUTs deposited onto the top external surface of an extruder adaptor placed at the pumping zone of the extruder.

Three echoes, L^1 , L^2 and L^3 , reflected from the barrel adaptor/polymer melt interface, are shown in Figure 5.6. The center frequency of these echo signals is around 10 MHz. The L^1 and L^2 signals have a SNR of 35 dB and 10 dB, respectively. At these SNRs of L^1 and L^2 , the commonly practiced cross correlation method can provide a measurement accuracy of ± 0.5 ns and then thickness measurement can remain the same accuracy of ± 3 μm with provided temperature, pressure, and composition of the steel.

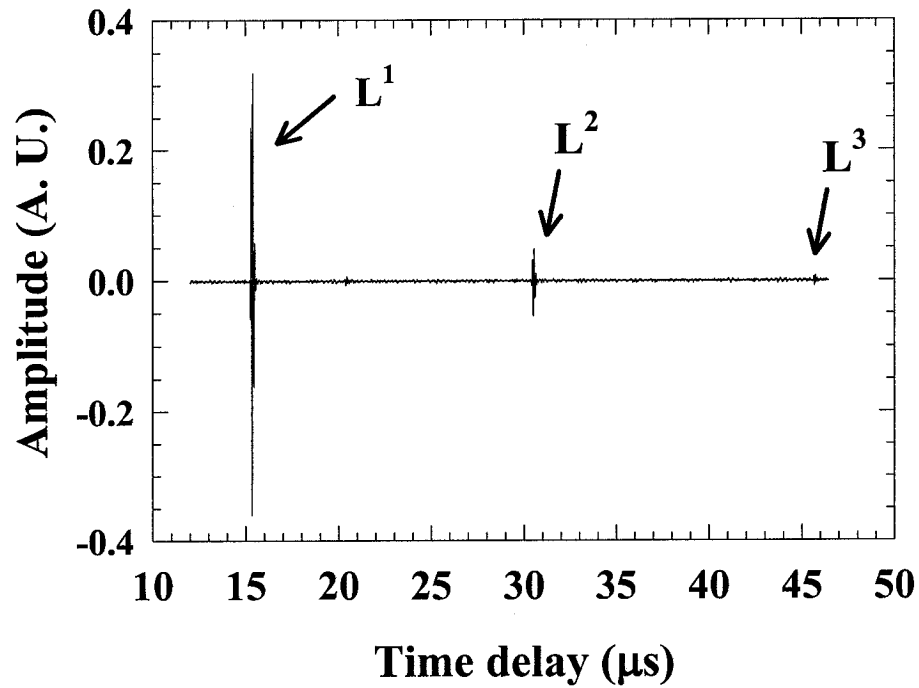
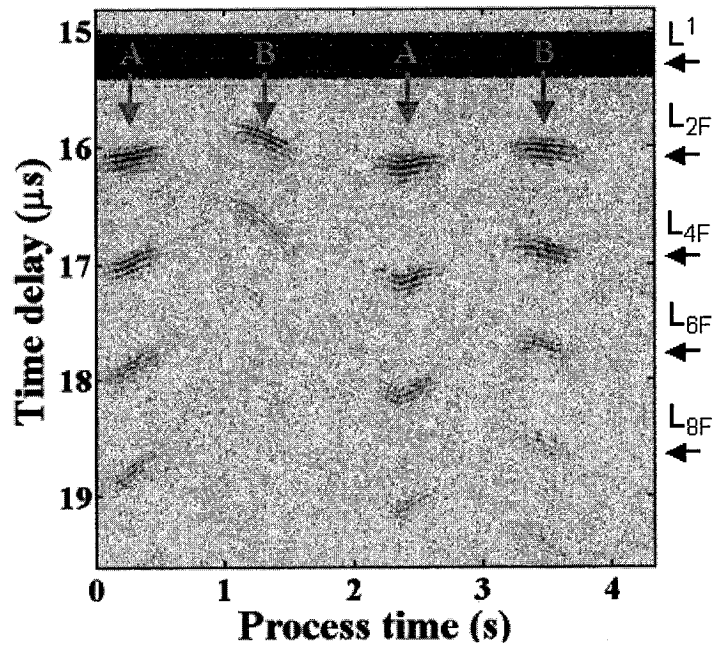
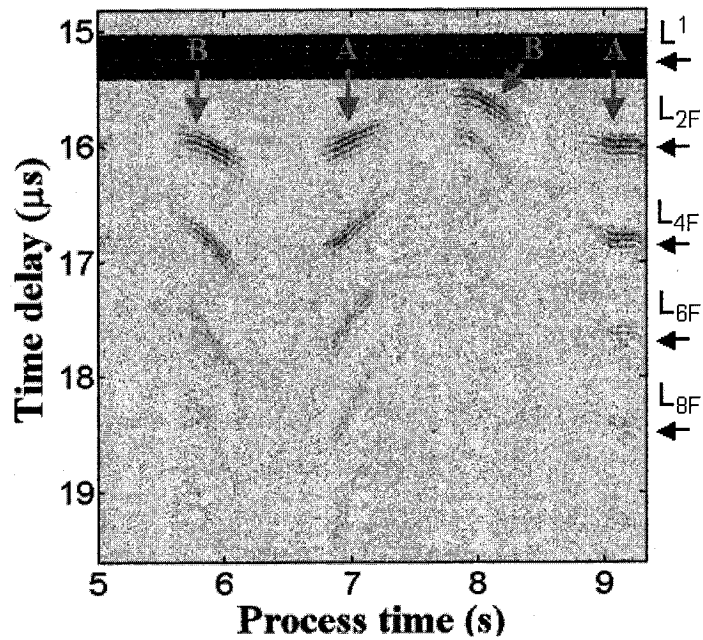


Figure 5.6 Echoes reflected at the adaptor/molten polymer interface and received by the sol gel sprayed BIT/PZT HTUT shown in the center of Figure 5.5.

Figures 5.7 (a) to (d) show the evolution of echoes reflected at the adaptor/polymer melt, and from the screw flight during the first 40 s of data acquisition, such as 0-4.25 s, 5-9.25 s, 10-14.25 s, and 35-39.25 s, respectively. In Figure 5.7, the amplitudes of the echoes are represented in gray scale, *i.e.* the higher the amplitude, the darker the gray level. Letters A and B denote echoes reflected by the tip of each screw flight. The varying arrival times of echo signals reflected from flights A and B were confirmed; these figures clearly demonstrate the ability of the sol gel sprayed HTUT to monitor screw deflection during extrusion.

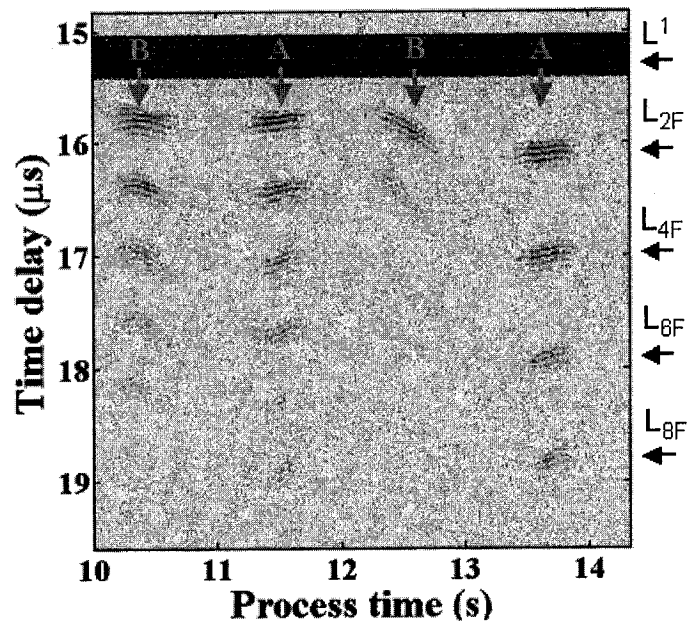


(a)

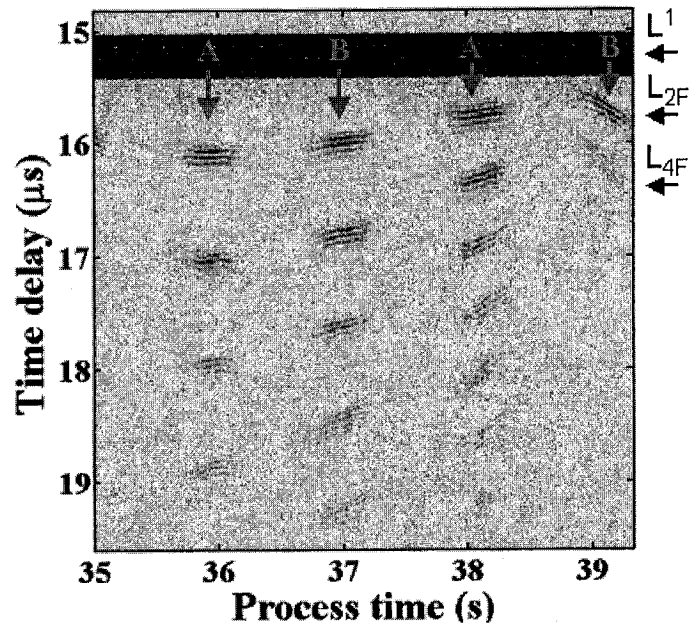


(b)

Figure 5.7 Evolution of echoes reflected at the adaptor/molten polymer interface (L^1) and from the screw flight (L_{2F} , L_{4F} , and L_{6F} , *etc.*) at the pumping zone with the sol gel- sprayed BIT/PZT HTUT during the first 40s of data acquisition. Letters A and B denote echoes reflected by the tip of each screw flight within one revolution.



(c)



(d)

Figure 5.7 Evolution of echoes reflected at the adaptor/molten polymer interface (L^1) and from the screw flight (L_{2F} , L_{4F} , and L_{6F} , etc.) at the pumping zone with the sol gel- sprayed BIT/PZT HTUT during the first 40s of data acquisition. Letters A and B denote echoes reflected by the tip of each screw flight within one revolution.

To demonstrate signal quality, a single trace of the echoes extracted at 0.25 s process time from Figure 5.7 (a) is shown in Figure 5.8. Since the SNR is about 6 dB, the commonly practiced cross correlation method can provide a measurement precision of ± 10 ns and the gap between the barrel inner surface and top of the flight can be measured with accuracy of $10 \mu\text{m}$, assuming that the longitudinal velocity in the polymer melt is 1000 m/s using and that temperature, pressure and composition of the melt are constant. The accuracy of t_p measurement is limited to $55 \mu\text{m}$, due to uncertainty and variance in temperature and pressure measurements. Because of the low SNR, there may be the need of a rather dedicated signal processing technique for real-time monitoring of screw status. It should be noted that in large polymer extruder machines, the surface of the tip of screw flights is much larger than those of the screw used in this section, thus much higher ultrasonic echo strength, and as a consequence, a much higher SNR is expected, which could enable real time monitoring of screw status.

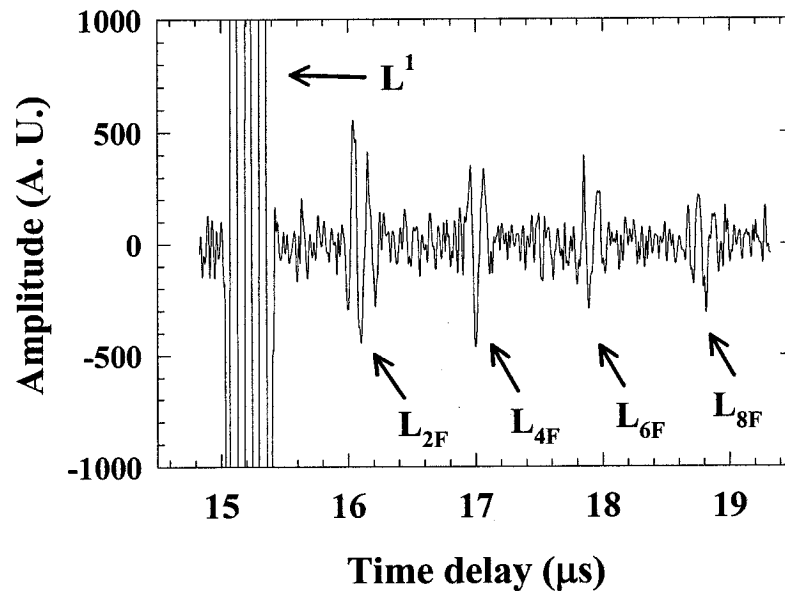


Figure 5.8 A single trace of signal extracted from Figure 5.7 (a) at 0.25 s process time.

In this section, only barrel wear and screw status monitoring is demonstrated. However, material properties such as density and viscosity can also be measured, since

ultrasound velocity, attenuation, reflection coefficient and scattered signals depend on molecular, chemical and physical properties of the material, and any changes in material properties and process parameters may be linked with variation of ultrasonic properties. In published papers, UTs have been demonstrated for monitoring viscosity [129], polymer degradation [129,130], extrusion instabilities [131], and residence time distribution [132]. It is expected that sol gel sprayed HTUTs are also capable of monitoring material properties during processing for real-time quality control.

5.3- Polymer injection molding

Polymer injection molding is widely used for mass production of various kinds of products such as telecommunication, transportation, automobile, commodity, and medical applications, *etc.* Real-time process monitoring during injection molding remains a fundamental issue as requirements of for high quality products and high production yield increase. Conventional on-line quality control strategies require the use of thermocouple and pressure sensors mounted in the mold. However, holes and channels must be machined in the mold for sensor installation, which is not preferable due to economic and geometric constraints. Furthermore, such conventional sensors may not provide sufficient information. For instance, thermocouples may provide only the surface temperature of the polymer melt, but not the bulk temperature nor temperature profile. Pressure sensors have a threshold below which no accurate reading may be obtained. Because of the condition of ruggedness, both temperature and pressure sensors may be big and lead to slow response. Non-intrusive and non-destructive ultrasonic sensors may be one of complementary tools, because of its ability to monitor the properties of polymers inside the barrel and mold during injection molding in real time. In this section, developed BIT/PZT HTUTs are applied to real-time process monitoring of polymer injection molding [23,133,134].

Injection molding is the process of forcing melted polymer into a mold cavity having a unique shape for a designed production part. Figure 5.9 shows a typical cycle of

injection molding: (i) the filling stage, where the polymer melt is injected into the cavity of a mold through a gate; (ii) the packing/holding/solidification stage, in which the cavity is completely filled with the material, and additional melt is forced into the cavity under high pressure until the gate is frozen, in order to compensate for shrinkage due to continuous cooling. The part is then further cooled until it is sufficiently solidified; (iii) the mold opening stage, when the mold is opened and the part is detached from the immobile mold; and (iv) the part ejection stage, when the part is ejected from the cavity of the mobile mold by the ejection pin. Then the mold is closed, and each stage is repeated.

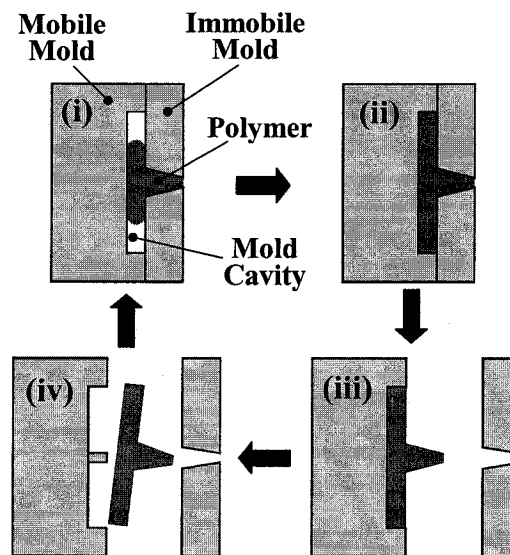


Figure 5.9 Cycle of the injection molding process: (i) the filling stage; (ii) the packing, holding and solidification stage; (iii) the mold opening stage; and (iv) the part ejection stage.

Overall, essential information can be monitored by ultrasonic technique during the process, such as filling completion, flow front advancement and flow front velocity, and solidification, which significantly affects the quality of the molded part. Here, real-time monitoring of filling completion is demonstrated using developed BIT/PZT ultrasonic sensors. Filling completion of the mold with the injected material is one of the most critical requirements for the molding process since the incomplete parts must be rejected.

In order to probe the behavior of the polymer inside the mold cavity during the injection molding process, BIT/PZT HTUT sensors were integrated into the mold insert. Mold inserts are commonly used in injection molding machines, particularly for multi-cavity molding processes. This approach, using sensor inserts in combination with a mold insert, is practical for molds of any size. Figure 5.10 shows a BIT/PZT HTUT sensor insert with (right) and without (left) electrical connection. A BIT/PZT HTUT was directly deposited onto a steel substrate as a small insert with dimensions of 44.5 mm × 25.4 mm × 12.7 mm. A silver paste top electrode with a diameter of 10 mm, which defines the active sensor size, was fabricated at the center of the substrate. Teflon insulated coaxial cables were used for electrical connection between the HTUTs and pulser-receivers. The maximum operating temperature of this coaxial cable is 200°C. For applications above 200°C, a ceramic insulated cable may be used as an electrical cable.

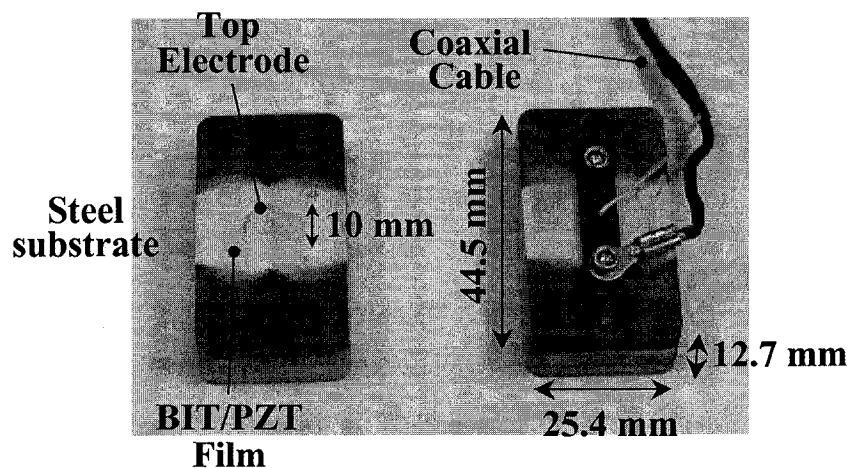
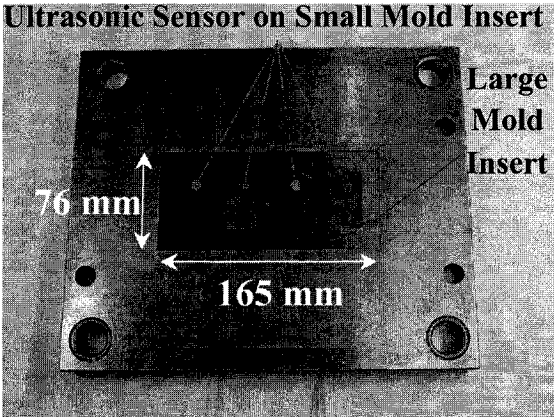


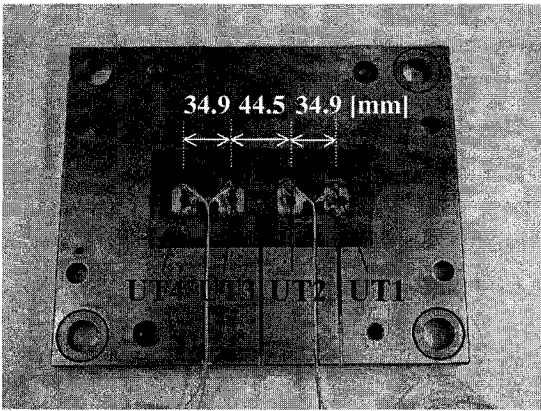
Figure 5.10 HTUT sensor inserts with (right) and without (left) electrical connection, used for monitoring the injection molding process.

A mobile mold and a large mold insert with four embedded HTUT sensor inserts (small inserts) are shown in Figure 5.11. The mold and mold insert were made of steel, like the substrates of HTUT sensors. The mold cavity dimensions are 76 mm × 165 mm × 1 mm. A hole at the center of the mold insert is for an ejection pin used for demolding

urpose. By replacing the mold insert, the shape and dimensions of the molded parts can easily be modified to meet the customer's demands. The bottom surfaces of the HTUT or insert and mold insert become the cavity surface of the mobile mold, as shown in Figure 5.11 (a). The distance between the centers of UT1 (UT3) and UT2 (UT4) was 34.9 mm, and the distance between UT2 and UT3 was 44.5 mm, as shown in Figure 5.11 (b). All HTUTs had almost the same ultrasonic performance. The center frequency and 6 dB bandwidth were 9-11 MHz and 6-8 MHz, respectively.



(a) Front View (Polymer Side)



(b) Back View (UT Side)

Figure 5.11 A mobile mold and a large mold insert with four embedded HTUT sensor inserts (small inserts).

Figure 5.12 presents a cross-sectional view of the mold (mobile and immobile), the large mold insert with four HTUT sensor inserts (UTs 1-4), and the molded part (or polymer melt), showing the paths of ultrasonic echoes. UTs 1-4 correspond with Figure

5.11. During the injection molding process, polymer melt is injected into the mold cavity through the gate placed at the center of the immobile mold. After a certain period, the mobile mold and the molded part are separated from the immobile mold; then the molded part is ejected from the cavity of the mobile mold by the ejection pin, as seen in Figure 5.9. For comparison with ultrasonic data, a temperature and pressure sensor (6190A, Kistler Instrument AG, Winterthur, Switzerland), whose sensing end is circular with a diameter of 4 mm, is attached to the immobile mold, with the end of the sensor flush with the inner surface of the immobile mold. The end of this Kistler sensor faces UT1, as shown in Figure 5.12. Ultrasonic waves propagated into the mold insert are reflected at the bottom surface of the mold insert contacting the mold cavity; when the polymer fills the mold cavity, the ultrasonic energy is partly transmitted to the molten polymer, and then reflected by the immobile mold. Echoes are denoted by L^1 and L_2 in Figure 5.12 respectively. The echoes L^2 , L^3 , ... and L_4 , L_6 , ... represent further round-trip echoes in the corresponding media.

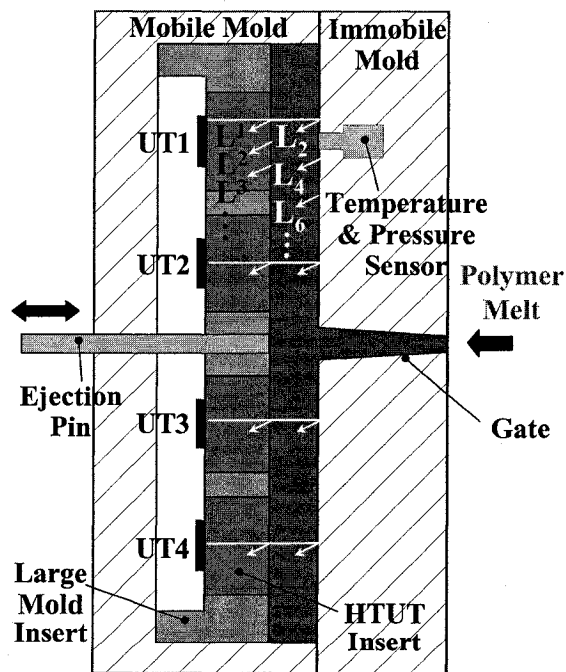


Figure 5.12 Cross-sectional view of the mold (mobile and immobile), large mold insert with four HTUT sensor inserts (UTs 1-4), and molded part (polymer melt). L^n and L_{2n} ($n=1,2,3,\dots$) represent n -th round trip echoes propagating in the mold insert and the polymer, respectively.

All the experiments presented in this section were conducted in ultrasonic pulse-echo mode. The ultrasonic data acquisition system was composed of four pulser-recivers (PR35, JSR Ultrasonics, Pittsford, NY for UT1 and UT2; 5072PR, Panametrics Inc., Waltham, MA for UT3 and UT4), two 12 bit dual-channel digitizing boards (CompuScope 12100, Gage Applied Science Inc., Montréal, QC, Canada) with a sampling rate of 50 MHz for each channel, and two personal computers. The experiments were carried out using a 150-ton injection molding machine (Engel GmbH, Schwertberg, Austria). The material employed was an injection grade polycarbonate, PC (CALIBRE 200-14, Dow Chemical Co., Midland, MI), an amorphous thermoplastic. The molding conditions were set as follows: melt temperature was 320°C; mold temperature was 120°C; and injection speed was 110 mm/s. The total cycle time was about 30 s. The data acquisition rate was 10 Hz, unless specifically mentioned.

Figure 5.13 shows a typical result of acquired signals from UT1 during injection molding. Although the signals were acquired during a whole cycle (30 s) with time delay ranging from 4 to 24 μ s, covering L^1 to L^5 echoes, only the signals at the beginning (from 4 to 9 s) and the end (from 22 to 27 s) of the process in the time delay range from 4 to 9.6 μ s, covering L^1 to L^2 echoes, are shown. S^1 represents the first round trip shear wave echo reflected at the bottom surface of the mold insert, contacting the mold cavity. When the polymer melt arrived at UT1's location at a process time of 5.8 s, L_2 and L_4 echoes propagating in the polymer started to appear. At this moment, L_6 and L_8 echoes were out of the time delay range in Figure 5.13. At a process time of 25.5 s, L_2 , L_4 , L_6 and L_8 echoes vanished, indicating that the molded part was detached from the mold insert.

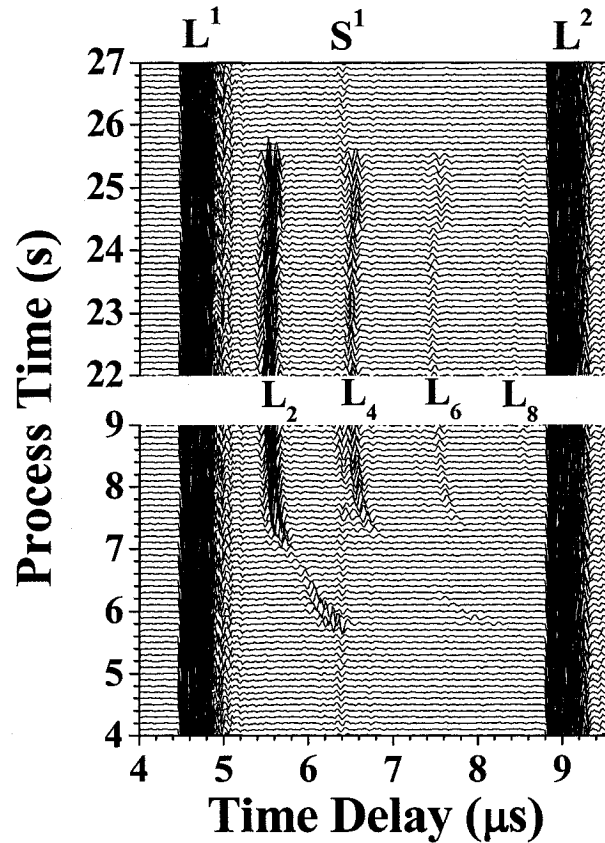


Figure 5.13 Typical signals measured with UT1 during injection molding.

In order to investigate further the correlation between observed ultrasonic signals and the process cycle, the amplitude values of L^4 and L^2 echoes with respect to process time were calculated, using signals obtained from UT1. Here the L^4 echo was chosen instead of L^1 , since higher-order round trip echoes of L^n can lead to higher sensitivity to the mold insert/polymer interface condition in principle, because of more reflection at this interface [4]. This result is presented in Figure 5.14 (a). Temperature and pressure values measured by the Kistler sensor are also presented in Figure 5.14 (b) for comparison. It should be noted that the data shown in Figure 5.14 were acquired during a different cycle than those in Figure 5.13; thus the process time at which L_2 echo appeared or disappeared in Figure 5.14 (a) is different from that in Figure 5.13.

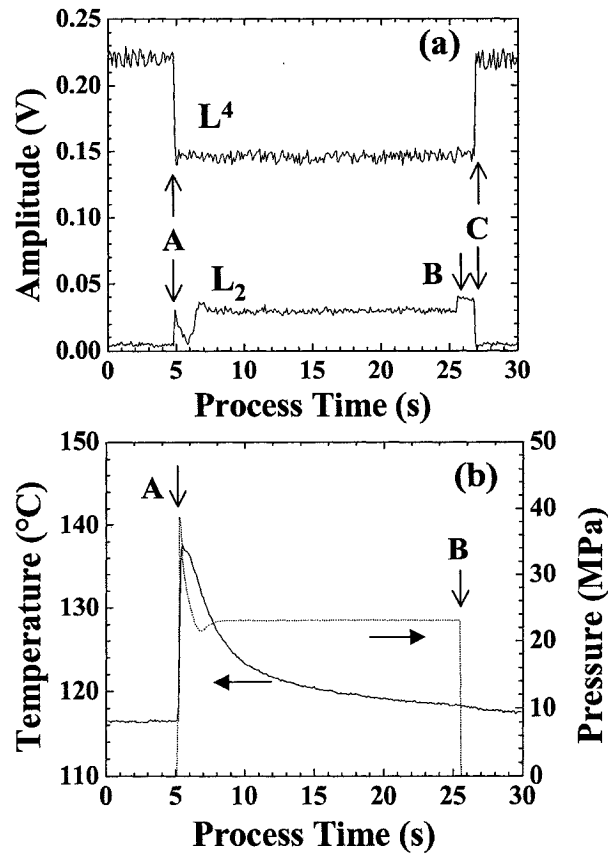


Figure 5.14 (a) Amplitude variations of L^4 and L_2 echoes measured with UT1, and (b) temperature (solid line) and pressure (dotted line) variation measured with a Kistler sensor during injection. Arrows A, B and C indicate the times of flow front arrival at UT1 location, mold opening and part ejection, respectively.

At process time A, the polymer melt arrived at UT1 and the Kistler sensor location simultaneously. The amplitude of L^4 echo suddenly decreased, and L_2 started to appear, as seen in Figure 5.13 (a), since a part of the ultrasonic energy was transmitted into the polymer through the mold insert/polymer interface. As shown in Figure 5.13 (b), around process time A, the pressure and temperature raised sharply from zero to 40 MPa and from 116°C to 137°C, respectively. It should be noted that the pressure sensor has a threshold in its response, resulting in a slight time delay, in this case around 0.1 s response difference from the ultrasonic measurement. In addition, the measured temperature was below the melt temperature of 320°C, since the Kistler sensor is only

able to measure the temperature of the contact (or surface) of the part and not melt temperature.

Just after time A, the amplitude of L_2 echo decreased and increased for a few seconds, between 5 and 7 s, which may reflect varying ultrasonic attenuation in the polymer during solidification. As soon as the molten polymer is injected into the mold cavity, it comes into contact with the cold mold, and starts to solidify. During solidification, attenuation takes a maximum value at a certain temperature, even though the velocity increases monotonically [135]. At process time B, the mold was opened and the molded part was detached from the immobile mold, as shown in Figure 5.9 (iii). Consequently, the amplitude of L_2 echo increased due to the almost total reflection at the polymer-air interface. In addition, a phase change of 180° was observed in the L_2 echo at process time B, since the acoustic impedance of the polymer is less than that of the steel mold but larger than that of air, resulting in a change of sign of reflection coefficient at this interface from plus to minus. Such phase reversal of the L_2 echo is also a good indication of part detachment from the immobile mold. At time C, the amplitude of the L^4 echo recovered to its initial value and the L_2 echo disappeared, indicating that the part was detached from the mold insert due to part ejection, as shown in Figure 5.9 (iv). Therefore it can be declared that the times of flow front arrival, mold opening and part detachment were clearly observed in the ultrasonic echoes, as indicated by arrows A, B and C, respectively, in Figure 5.14 (a).

Complete filling of the mold with the material being injected is the most critical requirement for the molding process, since incomplete parts must be rejected. Figure 5.15 shows one incomplete molded part (#1) and three successively molded (#2-4) parts under the same molding conditions. Accidentally part #1 had defects on both bottom corners, as indicated by arrows in Figure 5.15. The volume filling rate for part #1 was calculated to be 99 %. Figure 5.16 presents the amplitude of L_2 echoes obtained during the cycles for parts #1-4 shown in Figure 5.15 from UTs 1-4, whose locations are indicated in Figure 5.15. Even though the part was filled at UT3 and UT4 locations for part #1, one can see that the L_2 echoes measured with UT4 appeared for a few seconds

only at the beginning of the cycle. In addition, the amplitude of the L_2 echoes measured with UT3 gradually decreased to noise level before the mold opened at process time B. These are due to the fact that the part detachment at the UT3 and UT4 locations occurred before the mold opened, because of shrinkage of the part caused by inadequate filling pressure. The L_2 echoes measured with UT2 for part #1 appeared in the entire time range between A and B; however the amplitude was a little smaller than those for parts #2-4. It is concluded that the presented ultrasonic method is able to monitor incomplete filling of the part, even if the lack of filling rate is only 1 %.

It should be noted that part ejection time C was not observed on the L_2 echoes measured with UT2 and UT3 for parts #2-4, as shown in Figure 5.16. This is because part detachment at UT2 and UT3 locations had already occurred at time B, since the part in the gate area was weakly pulled towards the immobile mold when the mold was opened, resulting in a slight bending of the part. The part in the gate area was cut from the molded parts after ejection; hence the part in the gate area is not seen in Figure 5.15.

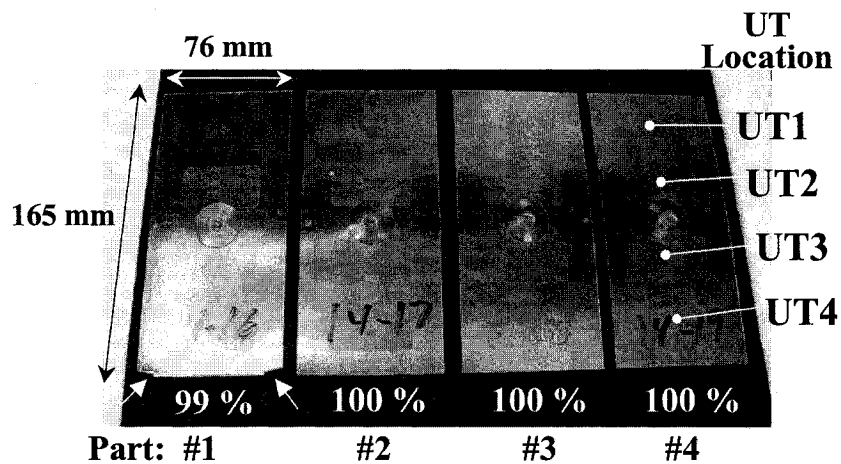


Figure 5.15 One incomplete (#1) and three complete (#2-4) molded parts under the same molding conditions. Filling rate of part #1 was 99%.

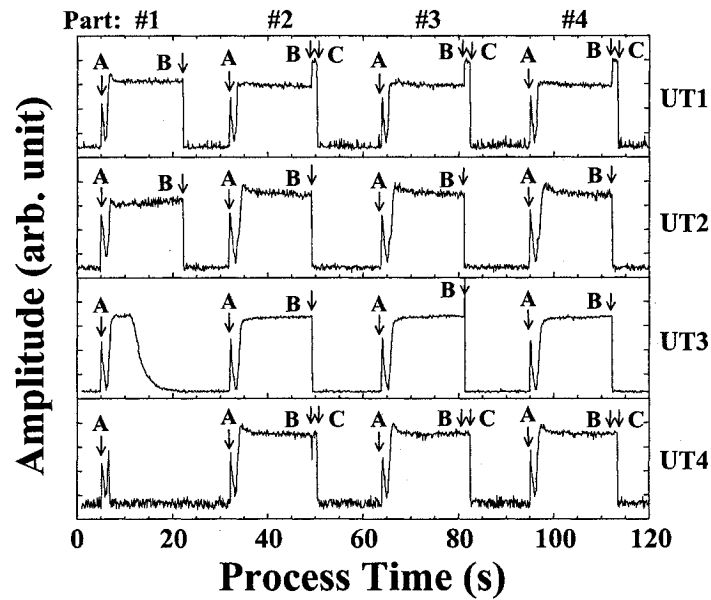


Figure 5.16 Amplitude variation of L_2 echoes measured during injection cycles for parts #1-4 shown in Figure 5.15.

5.4- Micro-molding

Miniaturization continues to be a demanding trend in the fields of MEMS, microelectronics, communication, optoelectronics, and biotechnology. However, conventional injection molding mentioned in the previous section has a scale-down problem: the smallest molded part has dimensions on the order of 1 mm, and a mass less than a gram [20]. In recent years micro-molding has been developing rapidly, and demonstrates the ability of fast and precise micro-fabrication [21, 22]. Micro-molding is different from conventional injection molding in terms of high injection speed and rapid cooling, while the fundamental process is similar. Process conditions may be more difficult than those in conventional molding. Very little work has been performed to investigate the actual dynamics of the process, even though real-time monitoring provides a deeper understanding of the process, crucial for simulated model validation. The size of micro-cavities may be difficult for conventional sensors to monitor. However, in a previous report [21], a pressure sensor was mounted behind the cavity ejector pin, and a

thermocouple in the mold, to monitor cavity pressure and mold temperature, respectively. As mentioned before, pressure sensors have a threshold response resulting in a time delay, and installing it behind the ejector pin puts a certain limit on its sensitivity [19].

It is the intention in this section to monitor the entire micro-molding process. Therefore, BIT/PZT UTs were fabricated on the external barrel and a mold insert of a micro-molding machine. A Battenfeld Microsystem 50 was selected as a typical commercial micro-molding machine; feed hopper and barrel section of the machine are shown in Figure 5.17. The barrel is mounted at an angle of 45 degrees to the injection axis, so the feeding metering piston can accurately prepare a dose of material.

Feed Hopper

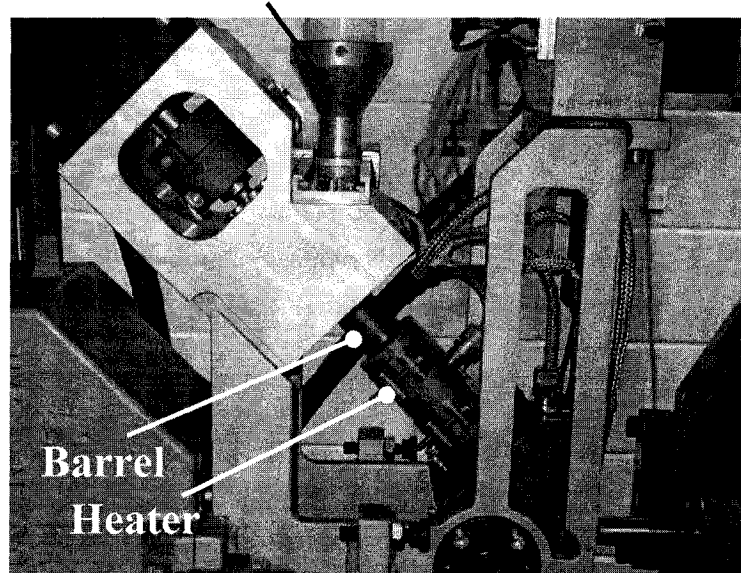


Figure 5.17 A part feed hopper and barrel sections of a Battenfeld Microsystem 50.

Figure 5.18 shows seven UTs fabricated on the barrel. UTs 1-3 and 5-7 were located in the feeding and heating zones, respectively, and UT4 between these zones. The length of the barrel was 265 mm. The internal diameter was 14 mm, and the external diameter at the areas of UTs 1-3, 5-7 and UT4 were 40 mm and 30 mm, respectively. All UTs had almost the same ultrasonic performance. The center frequency and the 6 dB bandwidth were around 13 MHz and around 13 MHz, respectively.

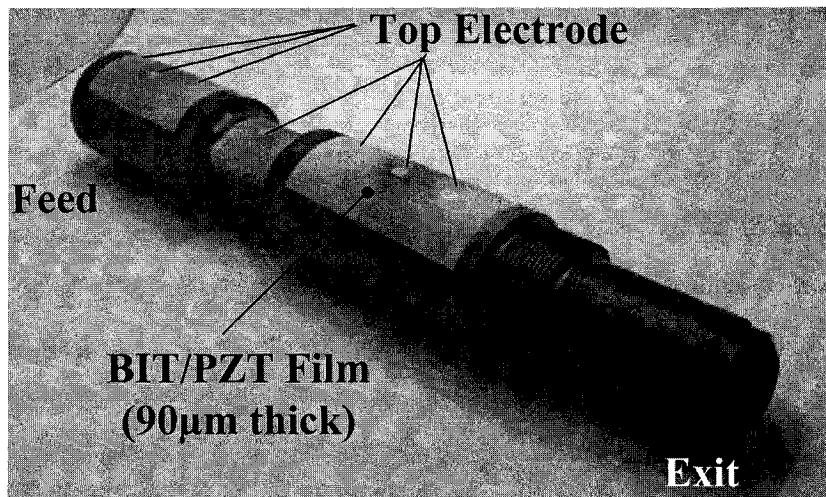


Figure 5.18 BIT/PZT UTs fabricated on the barrel of a micro-molding machine.

Figure 5.19 shows the four BIT/PZT UTs on the mold insert, with electrical connections for UT1 and UT2. The diameter and thickness of the mold insert were 61 mm and 18 mm, respectively. UT1 and UT2 were located above the cavity of the mold insert at depths of 1 mm (runner area) and 0.3 mm (part area), respectively. All HTUTs had almost the same ultrasonic performance. The center frequency and the 6 dB bandwidth were 9-11 MHz and 6-8 MHz, respectively.

Real-time monitoring of the micro-molding process was performed with the UTs fabricated on the barrel shown in Figure 5.18. First, polyethylene (PE) pellets were fed into the barrel and melted. The screw rotated at 110 rpm. A schematic diagram of ultrasonic wave propagation in a pulse-echo mode is shown in Figure 5.20. The UT mounted on the external surface of the barrel generates ultrasonic waves, which propagate through the barrel to its inner wall, contacting the PE melt. Similar to the description in section 5.1, the ultrasonic energy is partly reflected at the barrel inner wall/PE melt interface, and partly transmitted to the PE melt, then reflected either by the flight or the root of the screw. These Echoes are denoted by L^1 , L_{2F} and L_{2R} in Figure 5.20 respectively. Echoes L^2 , L_{4F} , and L_{6F} represent further round trip echoes in the corresponding media. Figure 5.21 shows resulting acquired signals from UT6 in the

heating zone of the barrel, as shown in Figure 5.18. The signals reflected from the flight and the root of the screw are clearly confirmed in Figure 5.21, with SNR of more than 10 dB. Therefore, real-time monitoring of polymer melt properties such as viscosity, density, composition, *etc.* is possible [135].

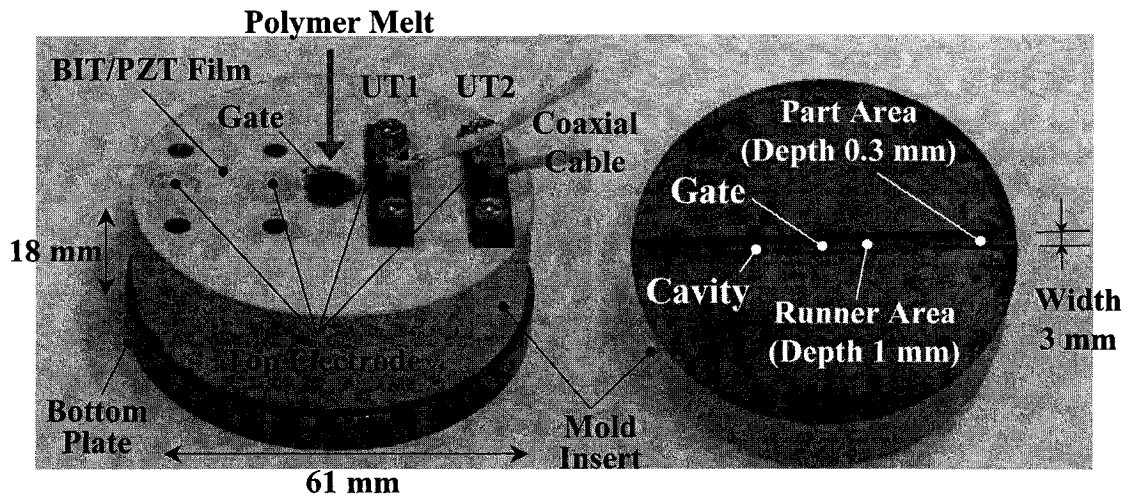


Figure 5.19 BIT/PZT UTs fabricated on the mold insert of a micro-molding machine.

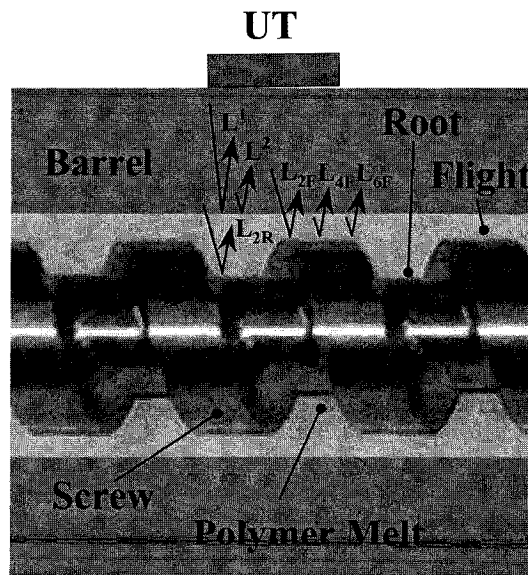


Figure 5.20 Schematic view of ultrasonic signals propagating in the barrel and the polymer melt.

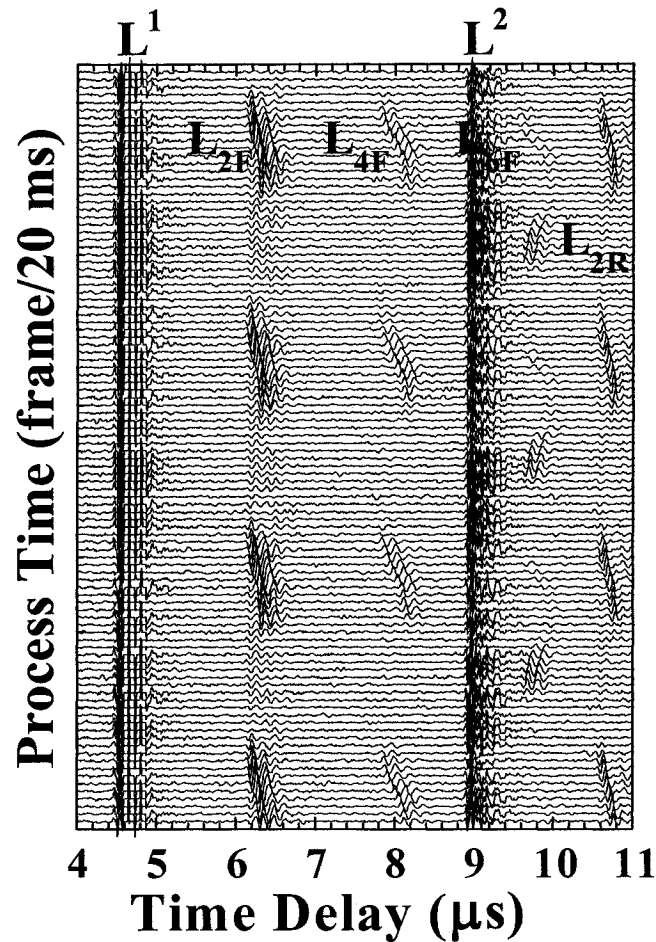


Figure 5.21 Ultrasonic signals reflected at the barrel/PE melt and PE melt/screw interfaces measured with the UT6 at the heating zone of the barrel.

Next, PE melt is injected and fills the cavity of the mold insert shown in Figure 5.19. Figure 5.22 presents a cross-sectional view of the mold insert with UT sensors (UT1 and UT2) and the PE melt, showing the paths of ultrasonic echoes. The ultrasonic waves propagate into the mold insert; their energy is reflected at the bottom surface of the mold insert contacting the mold cavity, and when the polymer fills the mold cavity, the ultrasonic energy is partly transmitted to the molten polymer, and then reflected by the immobile mold. Echoes are denoted by L^1 and L_2 in Figure 5.22 respectively. The echoes L^2 and L_4, L_6, L_8 represent further round trip echoes in the corresponding media. Figure 5.23 (a) and (b) show ultrasonic signals reflected at the mold insert/PE melt interfaces measured with UT1 above 1 mm-thick PE melt, and those measured with UT2 above 0.3 mm-thick PE melt in the cavity. The echo propagating in the PE melt with a thickness of

0.3 mm was clearly determined. It should be noted that echoes could be observed even with a thickness of less than 100 μm because of sufficient spatial resolution of the broadband BIT/PZT UT.

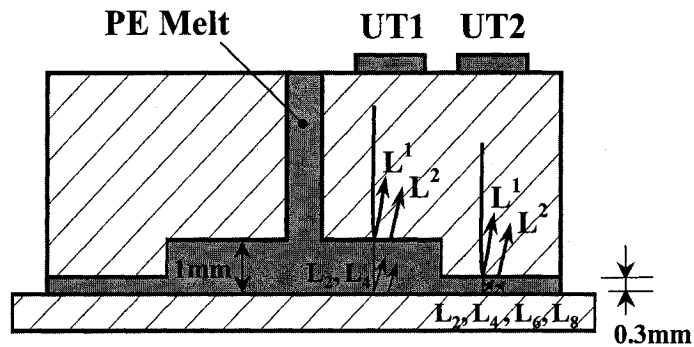


Figure 5.22 Schematic view of ultrasonic signals propagating in the mold insert and the PE melt.

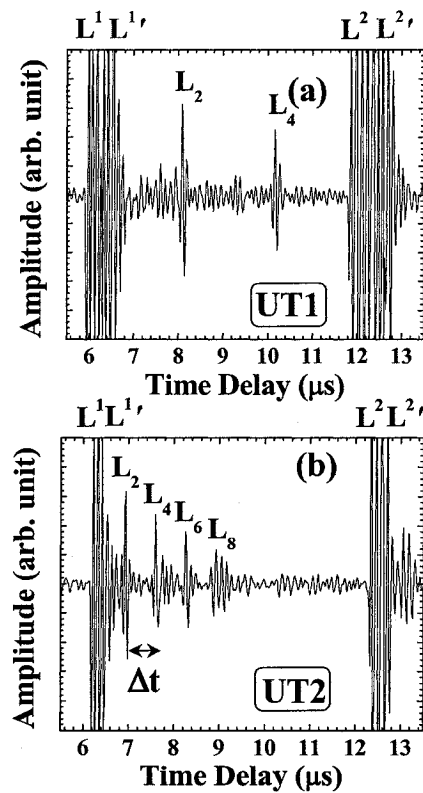


Figure 5.23 Ultrasonic signals reflected at the mold insert/PE melt interfaces, measured by UT1 above 1 mm-thick PE melt (a), and by UT2 above 0.3 mm-thick PE melt (b).

After complete filling of the cavity with PE melt, the ultrasonic velocity variation of the PE was measured during solidification. The velocity was obtained by $2t/\Delta t$, where t is a thickness of the PE in the cavity and Δt is the time delay difference between L_2 and L_4 echoes measured with UT2, as shown in Figure 5.23 (b). The result is presented in Figure 5.24. The velocity increases linearly as temperature increases. This result is in good agreement with that measured by the static ultrasonic measurement system [135].

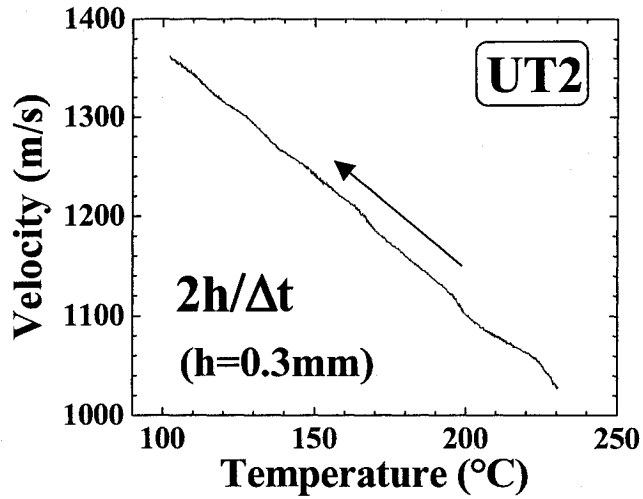


Figure 5.24 Velocity change of PE in the cavity of the mold insert during solidification.

5.5- Summary

Real-time monitoring of industrial material processing, such as polymer extrusion, injection molding, and micro-molding, has been demonstrated. BIT/PZT and LT/PZT UTs were fabricated on the external surfaces of barrel and mold inserts in order to probe conditions inside the barrel and the mold cavity, respectively.

By using the broadband HTUTs developed in this thesis work, real-time monitoring of barrel wear and screw conditions during polymer extrusion, and of filling completion during injection molding, have been successfully performed. For injection molding, HTUT were fabricated onto small mold inserts embedded into a large mold insert. In this configuration, ultrasonic monitoring was non-invasive and non-destructive. A thickness measurement of less than 100 μm in PE melt is possible for micro-injection molding. Velocity obtained during solidification of PE during micro-molding shows good agreement with that measured by a static ultrasonic system. Since ultrasonic velocity is related to material properties such as viscosity, density, composition, *etc.* [135], it is suggested that real-time monitoring of material properties is possible, and offers great potentials for micro-molding as well.

Chapter 6

Development of HTUTs using brazing and diffusion bonding techniques

6.1- Introduction

As mentioned in Introduction, development of cost-effective sensors and ultrasonic systems is crucial for industries to produce high quality products with low cost. Nondestructive testing of materials at elevated temperature and on-line ultrasonic monitoring application include the following required conditions for HTUTs; high operating temperature, relatively low MHz center frequency, broad frequency bandwidth, high SNR, high piezoelectric strength, *etc.* However, it is quite a challenge to fulfill all these requirements. For example, sol gel spray HTUTs can satisfy all the above requirements except that the piezoelectric strength is not strong due to the porosity existed in the thick film. If the strength is not high, for example, the thickness of the polymer melt under monitoring must be small; this causes the limitation of on-line ultrasonic monitoring of polymer processes.

To fabricate a HTUT, using a high T_c piezoelectric material is not sufficient, rather the entire HTUT assembly must be able to withstand high temperature and with acceptable performance. For example, backing materials and couplants are generally used for UTs, as shown in Figure 6.1, to obtain broad bandwidth and good ultrasonic transmission, respectively. But Tungsten/Epoxy composite, mainly used as a backing material for room temperature UT because of its high absorbance and acoustic impedance matching [55], cannot be used. The reason is that most epoxies cannot exceed 250°C [56]. Liquid couplants can be usually interposed between a piezoelectric transducer and the object, to help ultrasonic transmission. However, they evaporate at elevated temperatures.

It means that after a certain time, replenishment of liquid couplant is required. This might not be practical for continuous on-line monitoring. Dry ceramic powder or refractory adhesive cement may also serve as an alternative couplant, and can work at over 300°C [51,52]. However, signal strength and SNR will degrade due to the porous, thick film after drying [53]. Thin metal films such as gold and aluminum foil can replace the liquid couplant. In this case, in order to obtain acceptable ultrasonic transmission, pressure of $> 10 \text{ N/mm}^2$ should be applied between the stand-alone UT and the object during monitoring [54], which is not convenient.

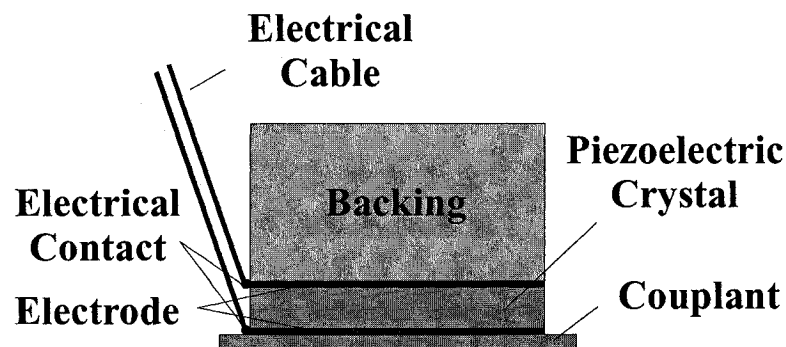


Figure 6.1 Schematic of a broadband UT with high loss backing material.

Therefore, in this chapter permanent bonding of single crystal with high T_c and high piezoelectric strength onto steel substrates are investigated. It is expected that single crystals will provide high piezoelectric strength because of lack of porosity. However, the ability to be used on curved surfaces may be sacrificed. To fabricate broadband HTUTs, a delay line with matched acoustic impedance can be used instead of a high ultrasonic absorption backing material [136-138]. Such a schematic is shown in Figure 6.2. In this chapter methods to establish bonding between piezoelectric single crystal and steel substrate for high-temperature use will be focused. Forming a successful bonding means that ultrasound can be transmitted through the interface efficiently during thermal cycles. Since the reflection coefficient at the solid-air interface is large, a gap larger than $1 \mu\text{m}$ may lead to total ultrasonic reflection at the gap. Therefore the bonding task is not trivial,

because substantial differences in mechanical and physical properties, especially in their coefficients of thermal expansion between the piezoelectric single crystal and metallic electrode or substrate or delay line lead to excessive stress at the interface. This stress may induce cracks and crack propagation during thermal cycles. In terms of bonding methods, brazing and diffusion bonding are discussed in this section. An LN single crystal was chosen for the piezoelectric crystal, due to its high T_c (around 1150°C [32, 45]) and commercial availability.

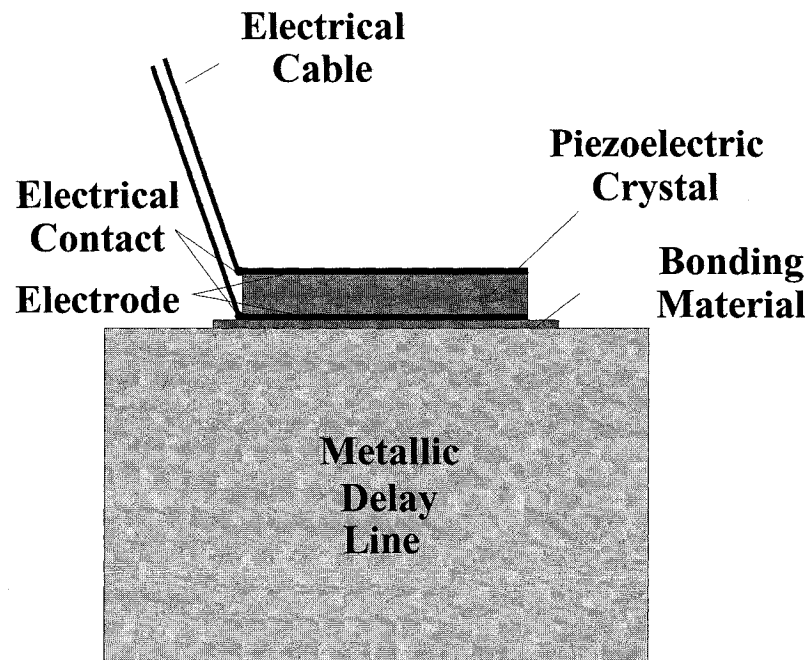


Figure 6.2 Schematic of a Broadband UT with a metallic delay line.

6.2- Brazing HTUTs

Brazing is a joining technique using heat and a filler metal whose melting temperature is above 450°C, but below the melting point of the joined materials. If the filler's melting temperature is lower than 450°C, the join is called soldering. Soldering is often not suitable for high temperature use, since the maximum operating temperature for the bonded parts depends on the melting temperature of the filler metal. If the melting

temperature of the filler temperature is higher than the joined materials, there is no reason to use a filler metal. Welding is similar to brazing; it joins metal parts by melting and fusing them together, usually with the addition of welding filler metal. Welding is not suitable for bonding LN to a steel substrate which is the delay line material used in this thesis, for several reasons given below. First, welding is not suitable for assembling dissimilar materials. Second, welding requires a higher temperature than brazing. Because piezoelectric materials tend to be depoled above half of their T_c , a lower processing temperature such as for brazing is preferable. Third, welding uses localized heating, which is not desirable for LN because LN is usually single crystal and has weak thermal shock resistance.

The principal of creating strong bonding between two parts by brazing is capillary action. During brazing, heat is applied. The filler metal is melted instantly by the heat, and drawn by capillary action completely through the joint interface. The bonding is created by a metallurgical bond between the filler metal and the surface of the part being bonded. In joining, forming an “intimate” interface is the first requirement. An “intimate” solid (the parts being joined)/liquid (the molten filler metal) interface can be formed if the liquid wets or spreads, thereby penetrating irregularities on the solid surface. The second crucial requirement in all cases is the presence of a stable chemical equilibrium at the interface.

As is seen in Figure 6.3, the shape of a drop of molten filler metal on a solid surface is determined by gravity and the interacting forces of solid-liquid interfacial energy (U_{SL}), solid-vapor interfacial energy (U_{SV}), and liquid surface tension (U_{LV}). This balance of interfacial tensions is characterized at equilibrium by the Young equation [139]:

$$U_{SL} - U_{SV} + U_{LV}\cos\theta = 0 \quad (6.1)$$

The angle between the solid surface and the tangent to the liquid surface at the contact point, or contact angle θ , varies from 0 to 180°. Contact angle θ is greater than 90° when

U_{SL} is larger than U_{SV} , and the molten filler drop tends to become spheroid, as shown in Figure 6.3 (a). If the contact angle θ is less than 90° , the liquid filler metal drop flattens out and wets the solid surface, as shown in Figure 6.3 (b). To form a joint with brazing filler metal, the surface of the solid material must be wet, meaning that U_{SV} must be larger than U_{SL} . However, since ceramics and crystals both have high U_{SL} , it is difficult to wet their surfaces. In addition, they do not react with normal brazing filler metal liquids, so that there is no chemical equilibrium at the interface.

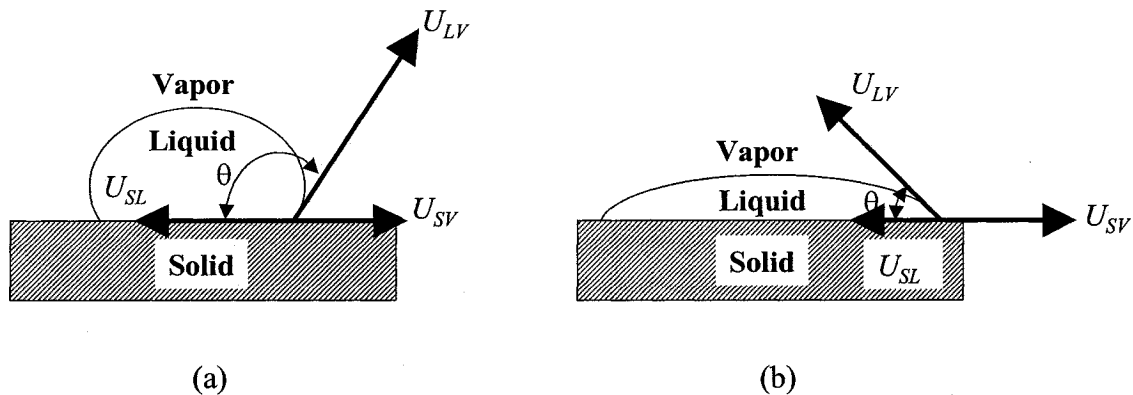


Figure 6.3 Schematic of sessile drops and interfacial energies (a) non-wetting (b) wetting.

There are two main approaches to accomplish wetting and an equilibrium reaction between a metal part and a ceramic or crystal part: one is active brazing [75,139]. A small percentage of a reactive metal such as titanium is added to the Cu x Ag brazing filler metal. The high oxidation potential of titanium causes a redox reaction with the ceramic, which results in spreading the brazing filler liquid metal, forming an oxide compound at the interface, and strong chemical bonding. Another extensively used procedure is metallizing the ceramic surface, so as to join two metal surfaces with standard brazing materials. In this section, the latter procedure metallizing was selected, since active brazing materials cause chemical reactions with the piezoelectric material, which may degrade its piezoelectricity. Molybdenum/manganese or some other type of metallizing is common; however, this process is complicated and expensive [139,140]. In this section, we used LN single crystals with Cr/Au electrodes, a commonly commercially available configuration, so that metallizing for wettability and top electrode fabrication can be accomplished in one step.

Next we explain the detailed brazing bonding procedure. First one must prepare an LN crystal with a Cr/Au electrode and a steel substrate; commercial 36° rotated Y cut LN crystals for longitudinal UT with Cr/Au electrodes were purchased, for example, from Almaz Optics, Inc, Marlton, NJ, USA. Then both surfaces must be carefully cleaned; capillary action works properly only when the surfaces are clean. Contaminants such as oil or grease will form a barrier between the surfaces and the brazing material, carbonize during heating, cover the surfaces, and disturb the wetting. Oil and grease are removed by dipping into a suitable degreasing solvent. For the steel delay line, abrasive cleaning is required next to remove the oxide layer. After rinsing, further ultrasonic cleaning with degreasing solvent is carried out. Once the parts are thoroughly clean, the brazing process should be done as soon as possible, to prevent recontamination.

After cleaning, parts should be assembled with brazing material before heating. The brazing filler metal is placed between the LN crystal coated with Cr/Au electrode and the steel delay line. The brazing filler metal is usually covered by flux, a chemical compound to prevent, dissolve and absorb any oxides during heating. Fluxing is an essential step in the brazing operation, since heating a metal surface accelerates the formation of oxides, resulting in chemical combination between the hot metal and oxygen in the air, which impedes wetting. Fluxing can be omitted if the assembly is brazed in a controlled atmosphere, a gaseous mixture or vacuum in an enclosed space, usually a brazing furnace, so that the atmosphere completely envelops the assembly and prevents oxidation. The pressure to the LN crystal and the brazing material is added during heating.

Since LN has weak resistance to thermal shock, heat is added to the entire assembly up to the flow point of the brazing filler metal, in a furnace or a vacuum furnace. Problems encountered here include poor adhesion and crystal cracking. Poor adhesion comes from the weak amalgam composed of the brazing filler metal and the gold top electrode; this indicates that selecting the brazing filler material is important. Crystal cracking is mainly due to sudden thermal shock to the LN crystal. For brazing, rapid heating and cooling after the flow point is ideal; however, because of the thermal

conductivity difference between the LN crystal, Cr/Au electrode and the steel delay line, rapid heating and cooling causes thermal gradients inside the LN crystal. Furthermore, at the moment when the brazing filler metal liquefies, the temperature of the LN surface contacting the brazing filler liquid metal may increase rapidly, resulting in thermal shock within the crystal. In this section, after some preliminary tests of available brazing materials, a Cu × Ag brazing filler metal, Braze 630 from Lucas-Milhaupt, Inc., Cudahy, WI, USA was chosen. Its characteristics are shown in Table 6.1. Gold may be a better brazing filler metal for improving the wettability of the Cr/Au electrode; however, because of its higher brazing temperature, it can increase the possibility of cracking. Brazing was performed in a vacuum furnace, as shown in Figure 6.4; bonding was carried out inside the cylindrical vacuum chamber of a conventional vacuum system, employing a diffusion pump backed by a rotary pump. Heating came from an induction coil connected to a radio frequency provider. The cross section of the assembly is shown in Figure 6.5. The assembly was heated to around 900°C inside the vacuum chamber.

Table 6.1: Characteristics of Braze 630

Nominal Composition	
Silver	63.0 ± 1.0 %
Copper	28.5 ± 1.0 %
Tin	6.0 ± 0.5 %
Nickel	2.5 ± 0.5 %
Total other elements	0.15 % max.
Physical Properties	
Color	White
Solidus (Melting point)	690°C
Liquidus (Flow point)	800°C
Brazing temperature range	855°C – 1010°C

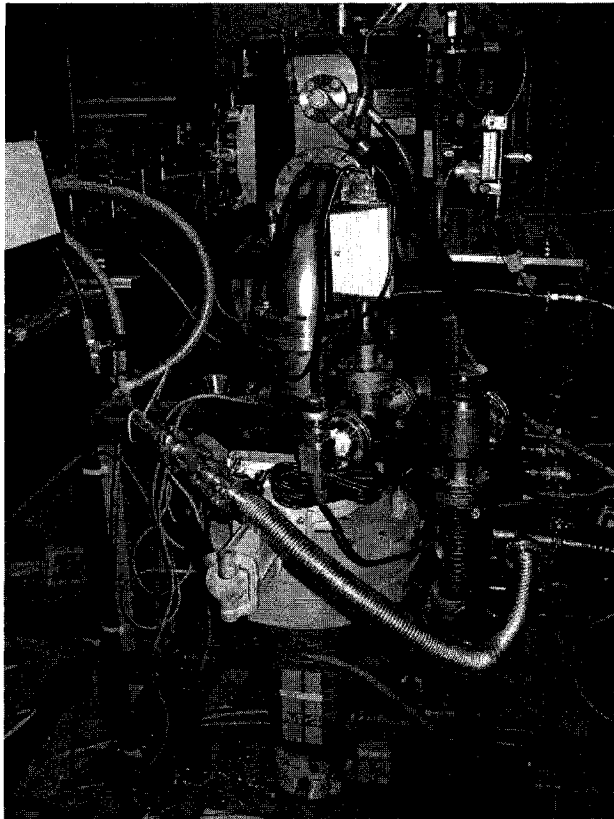


Figure 6.4 Vacuum furnace for brazing.

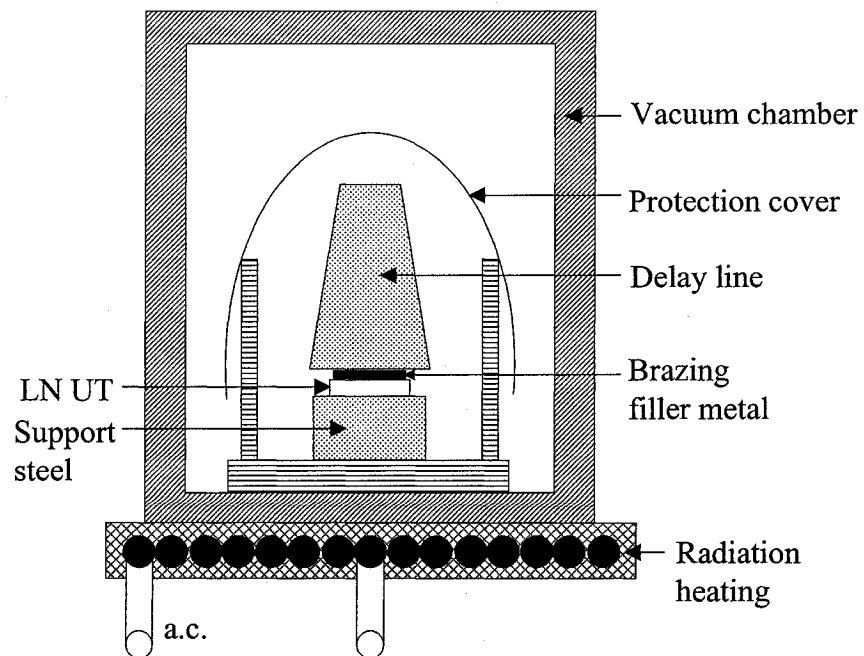


Figure 6.5 A cross section of the assembly for vacuum brazing.

The sample obtained is shown in Figure 6.6. The ultrasonic signal L^1 , L^2 , L^3 was obtained at 460°C; the results, shown in Figures 6.7 and 6.8, indicate the capability to fabricate a broadband HTUT. L^1 , L^2 , L^3 are n th echo reflected from the bottom of the substrate. Figure 6.8 shows the spectrum of the L^1 signal in Figure 6.7. The center frequency was around 13 MHz, and the 6 dB bandwidth is about 10 MHz. The SNR was more than 20 dB. However, several problems still remain. First, after brazing, the signal strength was weaker by 40 dB than that before brazing. The reason could be the deterioration of the Cr/Au electrode. The second problem is low reproducibility. For the future experiment, to change the brazing filler metal to gold filler metal or high-temperature soldering material may improve the reproductivity. Because of the weak piezoelectric strength, the ultrasonic performance of HTUTs made by brazing technique is inferior to that of the sol gel sprayed composite thick film BIT/PZT HTUTs.

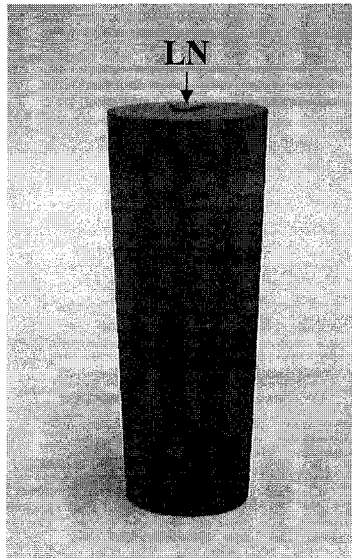


Figure 6.6 A sample of a LN HTUT brazed to a delay line.

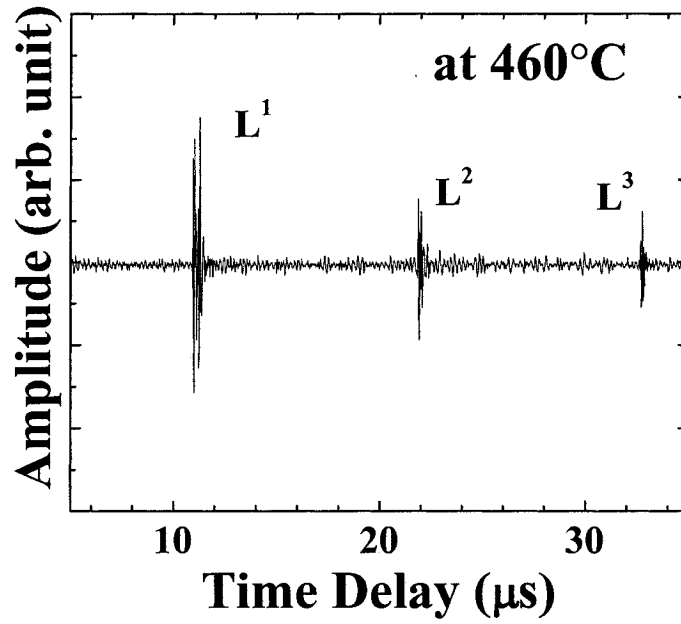


Figure 6.7 Time domain of ultrasonic signal obtained from the sample seen in Figure 6.6 at 460°C.

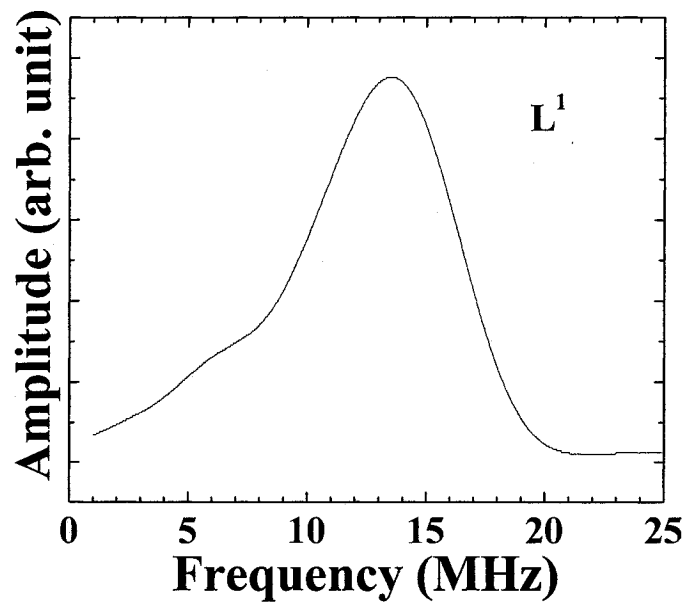


Figure 6.8 Frequency domain of ultrasonic signal obtained from the sample seen in Figure 6.6 at 460°C.

6.3- HTUTs with diffusion bonding

Solid-state diffusion bonding of ceramics to metals offers an alternative to brazing. According to the definition of the International Welding Institute, “Diffusion bonding of materials in solid state is a process for making a monolithic joint through the formation of bonds at the atomic level, as a result of closure of the mating surfaces due to local plastic deformation at elevated temperature, which aids interdiffusion at the surface layers of the materials being joined.” [141]. Diffusion bonding is also referred to as pressure joining, thermo-compression welding, solid-phase welding, *etc.*, since this process uses heat below melting temperature, along with pressure [141,142].

Diffusion refers to the actual transport of mass in the form of discrete atoms through the lattice of a crystalline solid. Diffusion may proceed by four mechanisms, such as exchange of place between two adjacent atoms, motion of interstitial atoms, circular exchange of four atoms, or motion of vacancies, as shown in Figure 6.9 (a)-(d), respectively. According to comparison results of activation energies, the vacancy mechanism is dominant for pure metals and alloys. An atom at a lattice site may jump to an adjacent site; when this happens, the diffusing atom can be activated so that it can clear the potential barrier between the sites, making diffusion bonding possible.

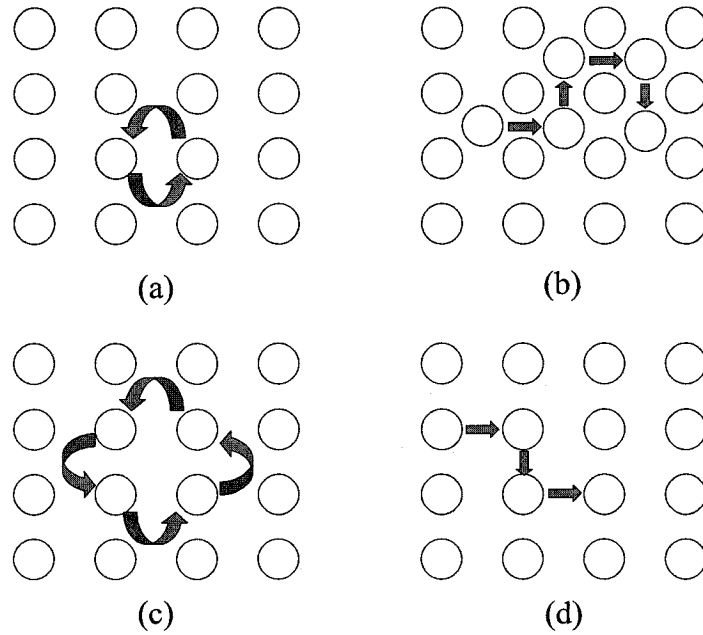


Figure 6.9 Mechanism of diffusion in a metallic lattice: (a) exchange of places between two adjacent atoms, (b) motion of interstitial atoms, (c) circular exchange of four atoms, and (d) motion of vacancies.

The diffusion of atoms can occur only if the diffusing atoms have sufficient energy to migrate through the lattice. For diffusion bonding two factors, mechanical and thermal energy, must be taken into account simultaneously. The diffusion bonding process can be divided into two basic phases; the first phase is forming and developing initial contact between the surfaces, and the second phase is forming a joint and developing bulk interaction. During the first phase, activation by heat and deformation, and the scouring of the surfaces, raise the potential energy of atoms so that metallic bonds can form. The activation parameters are bonding temperature τ and bonding pressure Π ; the hyperbolic relation is confirmed empirically as [141]

$$\Pi \tau = \nu_M \nu_N \sigma_y \tau_m = \text{constant} \quad (6.1)$$

where ν_M is the factor related to the mechanical energy extended to deform a volume B , ν_N is the factor related to the thermal energy imparted to the same volume B , σ_y is the yield strength, and τ_m is the melting point. The second phase is characterized by bulk,

grain-boundary and surface hetero- and/or self-diffusion; the principal parameters are bonding temperature τ , bonding pressure Π , deformation ζ , and holding time Δt . A simple, single model that covers all the varieties of diffusion bonding is difficult to develop. As an example, the equation for optimal parameters for a joint with impact strength $a_i = 0.5$, which is related with ν_N , of the bonding quality of low-carbon, low-alloy, and stainless steel in vacuum is obtained empirically as [141]

$$K_w = (\sigma_i^1 / \Gamma) (0.284 + \Pi / 25 - 0.046\sqrt{\Delta t}) \quad (6.2)$$

where K_w is the minimum value of σ_i^1 / σ_i^2 , σ_i^1 is the tensile strength of the softer metal, such as gold or aluminum in our case, in the combination at bonding temperature τ , and σ_i^2 is that of the harder metal, such as a steel delay line in our experiment.

Diffusion bonding offers several advantages over brazing and welding; specifically, high quality joints can be obtained at relatively low temperature. Therefore diffusion bonding between LN single crystals and acoustic delay lines has been investigated for many years [81,143-146]. Indium is used as the soft metal in many cases [81,143-145]. However, indium oxidizes easily, even at room temperature; therefore vacuum conditions are necessary for indium diffusion bonding. In this section, diffusion bonding between an LN crystal with Cr/Au electrode and a steel delay line was attempted at relatively low temperature, without vacuum. Gold/aluminum or gold alone was selected instead of indium/gold.

The detailed fabrication process is the following. First one prepares an LN with Cr/Au electrode and a steel delay line. Well-polished LN UTs with Cr/Au electrodes are commercially available. The steel delay line must be well polished, because good surfaces in contact are essential for diffusion bonding. Even for soft metals such as aluminum or gold or gold/aluminum, surface roughness should not exceed 80 μm . The surfaces are cleaned by acetone, methanol, and pure water, to improve adhesion between top surfaces and coated metal films in the next step.

A thin chromium layer is evaporated before soft metal evaporation, in order to enhance the adhesion between the top surfaces of the LN with Cr/Au electrode, the steel delay line, and the soft metals. Then a thick aluminum (soft metal) layer, around 1500-2500 Å, is evaporated onto each chromium layer. After fabricating the aluminum layer, a thick Au layer of around 500-1000 Å is evaporated onto the top of Al layer. Here Al layers can be replaced with thicker Au layers. These two types of configuration diffusion bonding will be examined and mentioned later.

After removal from the vacuum evaporation chamber, the additional Au layers of the LN with Cr/Au electrode and the Au layer on top of the steel substrate should be placed in contact with each other in a diffusion bonding unit, as shown in Figure 6.10, as soon as possible to prevent further contamination or oxidation. The sample assembly is almost the same as in Figure 6.11, except that a titanium sheet and an additional steel block were placed onto the LN UT. The additional steel block was applied to decrease the temperature transition inside the LN crystal. The LN UT has a Cr/Au top electrode, so that diffusion bonding might occur between the Cr/Au top electrode of the LN and the additional steel block, which would not be desirable. Titanium is more difficult to diffuse into steel than gold; thus it can suppress the bonding between the LN and the additional steel block.

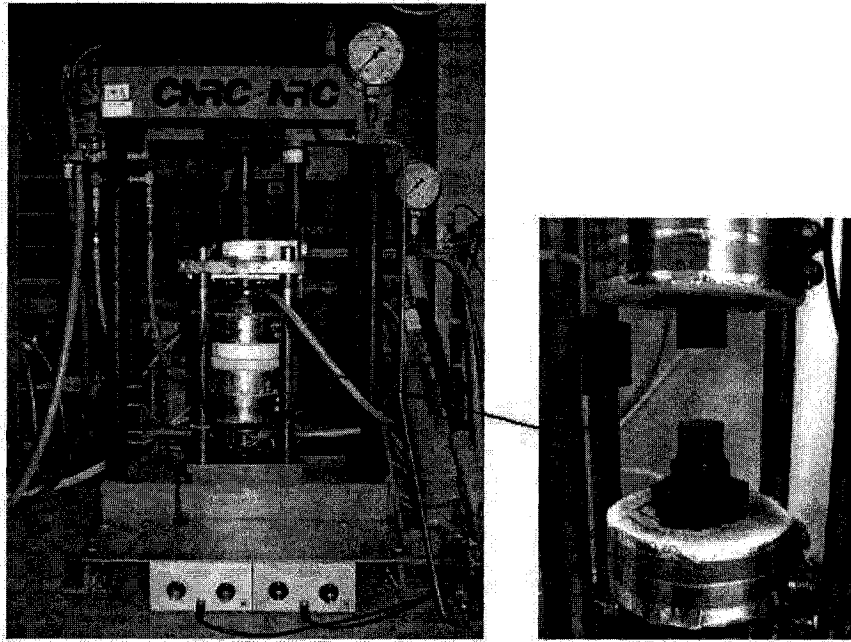


Figure 6.10 The diffusion bonding unit.

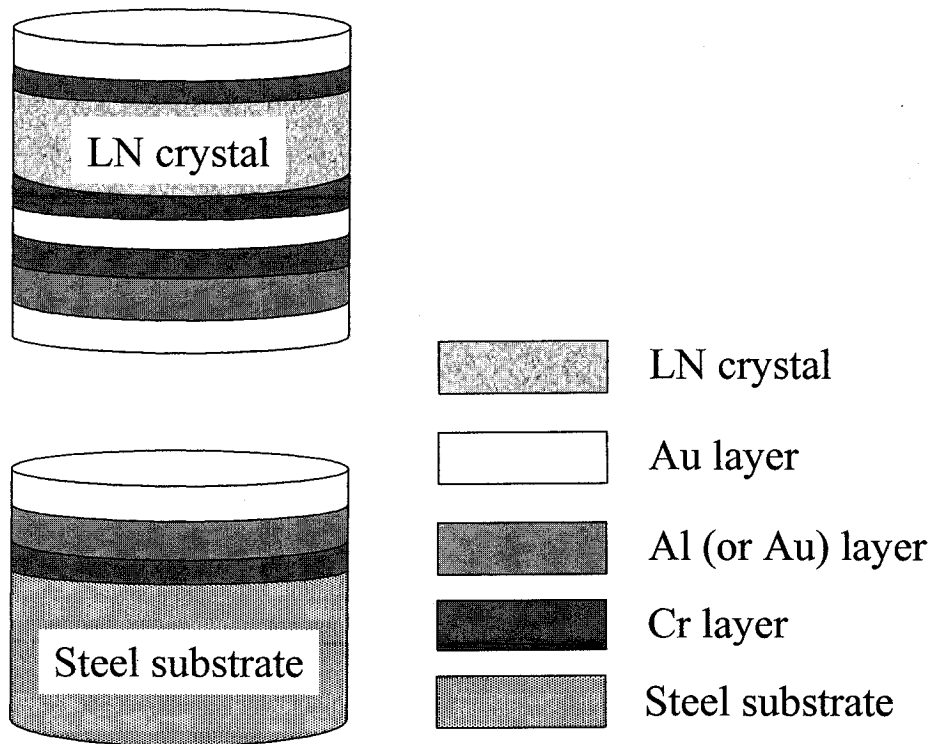


Figure 6.11 An exploded view showing the components before the diffusion bonding process.

Pressure is applied to the clean mating Au surfaces to establish contact. It is believed that the pressure produces several effects; first, it breaks up and removes brittle surface oxidation and contamination. Second, it brings the mating surfaces close, so as to enhance the actual contact and atomic interaction. Third, it activates the subsequent diffusion. When the pressure exceeds the yield strength, the surface crystals are brought to within the atomic distance in the lattice, so that actual contact is established. The concept of actual contact is broad; even when the surface crystals are brought to within the atomic distance in the lattice, the surface crystal does not produce a permanent and continuous crystalline structure. An electric contact is any mechanical contact between two mating surfaces which can conduct an electric current. For acoustic purposes, the contact must be much better than an electric contact, for ultrasound to penetrate through the contact, indicating that for acoustic contact, higher pressure is required than for electric contact.

The atoms in crystals are in a constant vibratory motion about their equilibrium positions in the lattice. As the temperature of the material increases, the amplitude of the motion in the lattice also increases. By quantum theory, the energy corresponding to frequency of energy quantum ϕ is given by [141]

$$U = \frac{1}{2} h\phi + \frac{h\phi}{\exp(h\phi / R\tau) - 1} \quad (6.3)$$

where h is Planck's constant, R is Boltzman's constant, and τ is the absolute temperature. The increase in amplitude raises both the kinetic and the potential energy of the atoms, and leads to disordered atomic structure in the case of metals. The most important effect of heating is to increase the rate of diffusion. Raising the temperature stimulates the re-distribution of atoms on the mating surfaces, brings the atoms close to each other, promotes the removal of various lattice defects in the bonding zone, and increases the rate of diffusion. It has been found empirically that at low temperature, the resulting bond is good even with a low diffusion rate. By heating to a temperature lower than the recrystallization point but sufficient to bring atoms to diffusion, there is a slowly

progressive recrystallization which is responsible for forming shared grains in the bonding zone of similar metals. This is an essential fact for diffusion bonding [141].

Therefore, high pressure and relatively low temperature were applied to the steel substrate, and these conditions were maintained for a relatively long period. The pressure, temperature and holding time used in the experiments were 67500 kilopascal, 300-350°C, and 6 hours, respectively. As mentioned before, two types of diffusion bonding, Cr/Al/Au and Cr/Au inter layers, were examined. A bonded sample is shown in Figure 6.12. Both types look similar, except that the samples using Cr/Al/Au inter layers include a purple colour in the gold, indicating that aluminium diffuses into the gold layer. Ultrasonic signals reflected at the bottom of the 12 mm thick steel substrate are shown in Figures 6.13 and 6.14 in the time domain at 300°C. L^n is the n th echo reflected from the bottom of the substrate. Signal strengths of both types for L^1 were almost the same, and 20 dB higher than that of a BIT/PZT HTUT; SNR was about 30 dB and 20 dB, respectively, lower than that of the BIT/PZT HTUT. Therefore, for high temperature experiment, this type of HTUTs can be used as complementary probes to sol gel sprayed composite thick film HTUTs because of high piezoelectric strength. However, further research is required to reduce the noise due to ringing effect that most likely comes from the incomplete bonding. Figure 6.15 and 6.16 show the frequency spectrum of the L^1 signal in Figure 6.13 and 6.14, for Cr/Al/Au and Cr/Au interlayer, respectively. Their center frequencies were about 5 MHz, and the 6 dB bandwidths were about 4 MHz, indicating that these two HTUTs with broad bandwidth were realized.

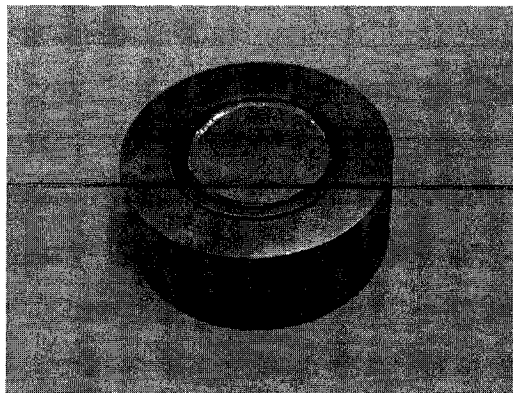


Figure 6.12 A diffusion-bonded LN HTUT.

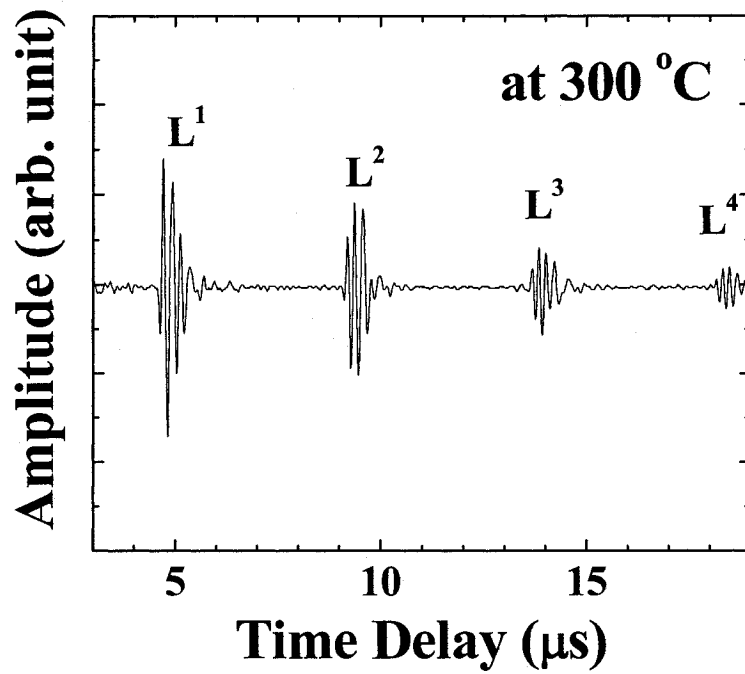


Figure 6.13 Time domain of ultrasonic signals obtained from the sample gold- and aluminium-diffusion bonded at 300°C.

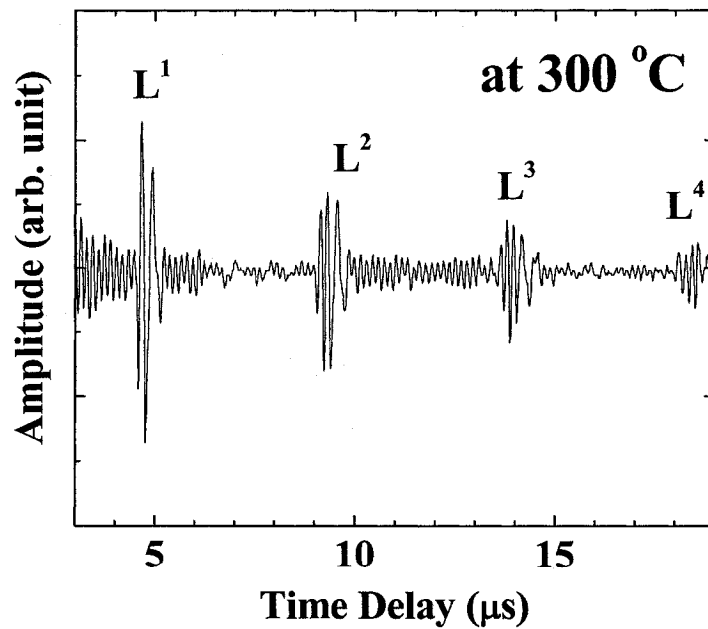


Figure 6.14 Time domain of ultrasonic signals obtained from a sample gold diffusion-bonded at 300°C.

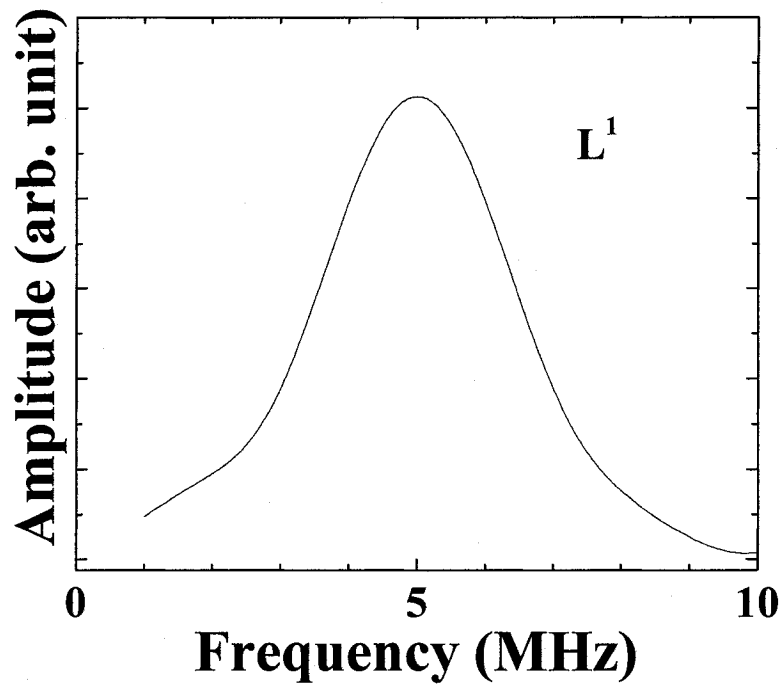


Figure 6.15 Frequency domain of ultrasonic signals corresponding to Fig. 6.13.

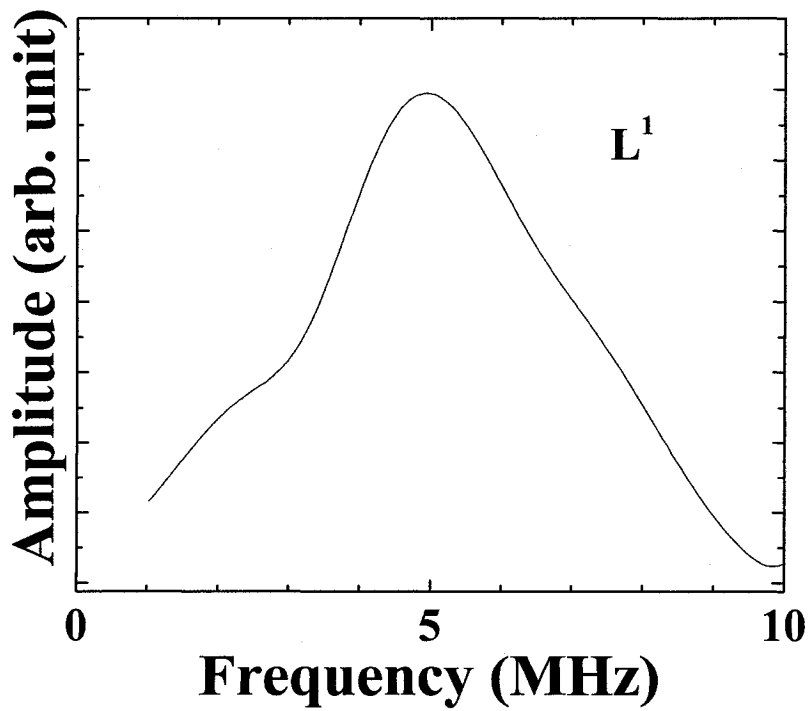


Figure 6.16 Frequency domain of ultrasonic signals corresponding to Fig. 6.14.

During raising and holding the temperature at elevated conditions, the signal seemed to be stable, and even had a few dB better SNR than that at room temperature. However, when the temperature is above 500°C, ultrasonic signals were significantly weakened, indicating that because of thermal expansion mismatch, good bonding was lost. Therefore, this type of HTUT currently operates below 300°C. After 140 thermal cycles between room temperature and 300°C, signal strength reduced by only 1 dB as shown in Figure 6.17.

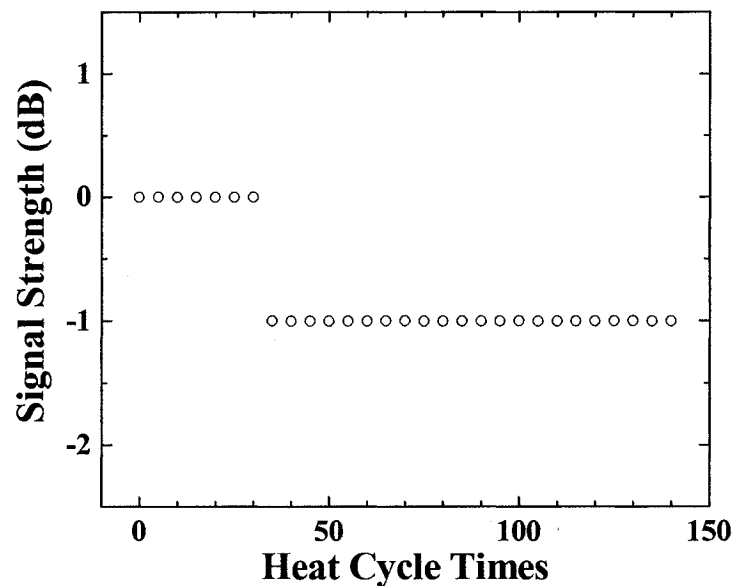
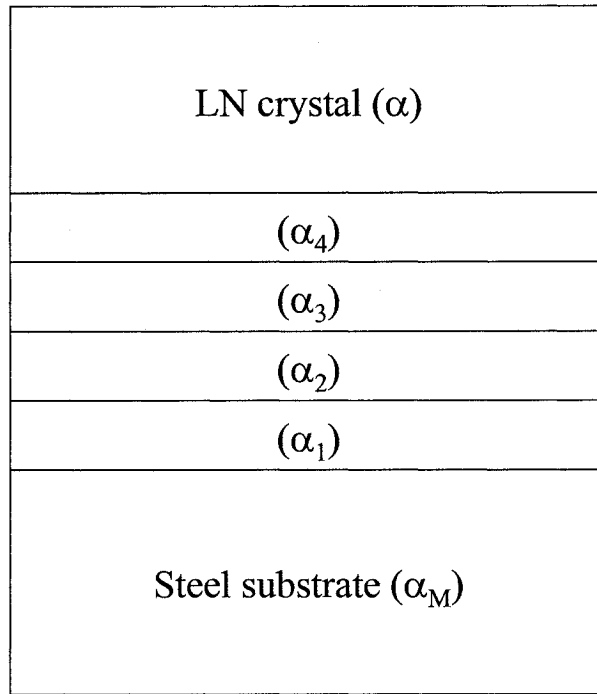


Figure 6.17 Durability test for a diffusion-bonded LN HTUT under thermal cycles between room temperature and 300°C.

Effects of the difference in thermal expansion coefficients between crystal and metal may be minimized by placing several layers between the substrate and the crystal. If the difference in thermal expansion coefficients between each layer is small, the interface stress also becomes small. The graded alpha technique shown in Figure 6.18 can reduce mismatch by incorporating layers of different thermal coefficients; interface stress may be minimized if the layers are properly designed [139].



$$\alpha < \alpha_4 < \alpha_3 < \alpha_2 < \alpha_1 < \alpha_M$$

Figure 6.18 Graded alpha technique designed to reduce thermal expansion coefficients.

The thermal expansion coefficient α is the first order thermal expansion coefficient. According to reference [136], the thermal expansion coefficient α of lithium niobate is about 1.5×10^{-5} . Thermal expansion coefficients of typical metals are shown in Table 6.2; thermal expansion coefficients α of alloy steels and gold are also around 1.5×10^{-5} and 1.4×10^{-5} , respectively, and agree well with that of lithium niobate. The chromium layer is negligible, since it is much thinner than other layers. Aluminum has a higher value, 2.5×10^{-5} , and may not be suitable since the aluminum interlayer can give high interface stress. However, the SNR of a sample using Cr/Al/Au interlayer was 10 dB better than with Cr/Au interlayer, as shown in Figures 6.13 and 6.15. Inter-diffusion between gold and aluminum may improve the bonding strength; alternative material candidates for aluminum include copper, nickel, titanium, *etc.*

Table 6.2: Thermal expansion coefficients α of typical metals

Material	High side of α ($\times 10^{-5}$)	Low side of α ($\times 10^{-5}$)
Zinc & its alloys	3.5	1.9
Lead & its alloys	2.9	2.6
Aluminum & its alloys	2.5	2.1
Tin & its alloys	2.3	
Silver	2.0	
Stainless steels	1.9	1.1
Coppers	1.8	1.4
Nickels & its alloys	1.7	1.2
Alloy steels	1.5	1.1
Gold	1.4	
Titanium & its alloys	1.3	0.9
Palladium	1.2	
Platinum	0.9	
Molybdenum	0.6	0.5

6.4- Summary

Brazing and diffusion bonding were tried to establish permanent acoustic bonding between a lithium niobate single crystal and a steel substrate to obtain HTUT with high signal strength. In brazing, the brazing filler metal, a kind of silver-copper alloy, was inserted between a lithium niobate crystal and a steel substrate, and then they were heated inside a vacuum furnace to around 900°C. The brazed sample demonstrated broadband characteristics at temperatures up to 460°C; for example, the center frequency was around 13 MHz, 6 dB bandwidth around 10 MHz, and the SNR about 20 dB. Further research is required to improve signal strength and the fabrication yield. In diffusion bonding, upon each surface of the lithium niobate and steel substrate, a thick gold layer or thick aluminum/gold layers were deposited; thin chromium layers were used for adhesion. After fabricating the interlayers, temperature of 300-350°C, and high pressure of 67,500 kilopascal were applied for 6 hours. The diffusion bonding sample also demonstrated broadband characteristics; for example, the center frequency was around 10 MHz, and the 6 dB bandwidth also 10 MHz, up to 350°C. This HTUT has a higher signal strength by 20 dB than sol gel HTUTs; the SNR was around 20-30 dB. Further research is required to improve the SNR and raise the operating temperature. Experimental results indicate that the performance of the HTUTs made by brazing technique, at present, is inferior to that of the sol gel sprayed BIT/PZT composite film HTUTs. The expected applications of the fabricated HTUTs by diffusion bonding can be similar to those presented in Chapter 4 and Chapter 5 involving flat surfaces.

Chapter 7

Conclusion

7.1- Thesis summary

This thesis began by introducing the need for NDE of metals and on-line monitoring of industrial material processes. The objective of this thesis was to develop broadband piezoelectric HTUTs for these applications and two methods were used. The former one was sol gel sprayed HTUTs, and the latter one was LN single crystal permanent bonding onto a steel substrate using brazing or diffusion bonding technique. Both types of HTUTs had been used for ultrasonic measurements at elevated temperatures.

The original features of sol gel type HTUTs presented in this thesis were film fabrication method, material selections, poling method and electrode materials. Previously sol gel type HTUTs were made by spin coating and they had exhibited broadband HTUT characteristics without couplant nor backing material [67-69]. However, spin coating technique used was not practical for industrial purpose, because it was difficult to fabricate HTUTs on the curved surfaces such as a barrel for micro-molding, and on the relatively large and odd shape's substrate such as an extruder adaptor for polymer extrusion. This problem had been solved by selecting spray coating technique as the film fabrication method. As sol gel composite materials, in addition to PZT/PZT and LT/PZT, which had been already tried at Queen's University [68,69], BIT/PZT and BIT/BIT were investigated in this thesis. BIT/PZT had demonstrated the excellent ultrasound characteristics at elevated temperature up to more than 450°C. Corona discharge poling had been used to achieve the piezoelectricity instead of the traditional poling. Since corona discharge poling does not require the top electrode, thus the poling at elevated temperature and/or for relatively large area can be accomplished without

dielectric breakdown. Top electrode was made of silver paste or vacuum sputtered platinum film.

The commercially available piezoelectric powders, BIT, PZT or LT powders were dispersed into PZT, alumina, and BIT precursor. In order to assure the uniformity of the composite solution, ball milling was operated and fine powders of which particle size was less than 1 μm were obtained. The composite solution was sprayed onto substrates by an air gun. The heat treatments up to 650°C were processed for the deposited films to crystallize the sol gel phase. The spray coating and heat treatments were repeated until the desired thickness for the desired frequency was obtained. After that, the corona discharge poling was operated to align the domain direction of the piezoelectric powders. Finally, the silver paste or platinum top electrodes were fabricated and the fabrication of HTUTs was accomplished.

The important properties for piezoelectric UTs are electromechanical coupling coefficient, dielectric constant, piezoelectric constant, and density. Properties of each film, PZT/PZT, PZT/ Al_2O_3 , LT/PZT, BIT/PZT and BIT/BIT were experimentally obtained. One of the important properties for piezoelectric UTs is thickness mode electromechanical coupling coefficient k_t . Recently resonance spectrum method was reported and simulation results for PZT/PZT films on stainless steel substrate were demonstrated [111,112]. In this thesis, the experimental measurement of k_t was tried for PZT/PZT film on steel substrate using this resonant spectrum method. Ultrasonic performances at room temperature and elevated temperature was examined for each sol gel film. BIT/PZT had mainly demonstrated the highest operation temperature among the tested materials, up to more than 450°C, and broadband characteristics with high SNR. For example, the center frequency, the 6 dB bandwidth and SNR for the first round trip echo reflected from a 12 mm thick steel substrate using BIT/PZT HTUT was 8.5 MHz, 4MHz and 34 dB, respectively. Therefore BIT/PZT had been mainly chosen as the material of HTUTs for NDE of metals, ultrasonic surface and sub-surface imaging at high temperature, and on-line industrial material process monitoring.

The experimental values of relative dielectric constant were compared with theoretical values of cube model as in several previous papers [107,147]. The calculated values of dielectric constant were significantly affected by volume % of pores. The volume % of the pores in sol gel sprayed film was estimated as around 20 % from this result. It confirmed the effectiveness of the cube model for sol gel sprayed composite materials. Therefore if the precise data are available such as elastic compliance, piezoelectric constant, Poisson's ratio, *etc.* of the pure sol gel film, the cube model could simulate the values precisely not only the dielectric constant but also d_{33} and k_t . It would be useful for the material selection and the decision of the volume ratio of powder over sol gel.

Using the developed sol gel spray coating technique, several kinds of piezoelectric sol gel composite films, such as BIT/PZT, LT/PZT, PZT/PZT, BIT/BIT and PZT/ Al_2O_3 40-200 μm films, in the range of 3-30 MHz, were directly fabricated on various surfaces, such as metal plate, concave and convex cylindrical surfaces, concave and convex spherical surfaces, and thin metal sheets and foil. This indicated that they could work as embedded or integrated sensors in materials and structures, because the piezoelectric materials could be sensors and actuators at the same time. NDE of metals at high temperature were tried using sol gel type HTUT and the extent of the defect in metal substrate could be observed at 440°C. Immersion type HT probe using BIT/PZT film were immersed into the molten zinc at 450°C for thickness measurement. The reflected echoes from the front side and the backside of a steel plate inside the molten zinc were successfully obtained. Ultrasonic surface and sub-surface imaging in water at room temperature and in silicone oil at 200°C were also carried out. The scanned ultrasonic front- and sub-surface images taken by the fully immersed focused probe showed good resolution.

HTUTs for on-line monitoring several industrial polymer material processes, such as extrusion, injection molding and micro-molding were tried. For polymer extrusion of high-density polyethylene (HDPE) and low-density polyethylene (LDPE), BIT/PZT and LT/PZT HTUTs were fabricated onto the surface of the extrusion adaptor respectively,

where the surface temperature was 190°C. They had demonstrated the capability of monitoring the barrel wear and screw status, which are important to keep the extrusion product quality and the production efficiency. For injection molding of polycarbonate (PC), four BIT/PZT HTUTs were fabricated onto the steel substrate and they were integrated into mold insert. The mold temperature and melt temperature were set as 120°C and 320°C, respectively. The signals through the polymer melt were obtained in real-time from four different points so that real-time on-line monitoring of filling completion was successfully demonstrated. Even 1 % lack of filling was clearly detected. For micro-molding of polyethylene (PE), BIT/PZT transducers were fabricated onto the barrel and the mold insert to monitor the entire process. The real-time monitoring was demonstrated at the barrel. The velocity change during the solidification of the polymer melt was measured at mold insert. The velocity of the polymer melt increased linearly as its temperature decreases. This result had good agreement with previous static ultrasonic system.

The establishment of rigid acoustic bonding at high temperature was tried between LN crystal with Cr/Au top electrode and steel substrate. Two methods were used in this thesis, brazing technique and diffusion bonding technique. In brazing technique, brazing filler metal was inserted between LN crystal and steel substrate, and the assembly was heated up around 900°C inside a vacuum furnace. A sample showed broadband characteristics. For example, the center frequency, the 6 dB frequency and SNR are 13MHz, 10 MHz and >20dB, respectively. And they could operate up to 400°C. The optimum conditions for the brazing process should be improved in the future to improve the signal strength and the reproducibility. In the diffusion bonding technique, thick Au or Al/Au films were fabricated onto the both surfaces of LN UT and steel substrate. Then they were heated to temperature of 300-350°C, and pressed under a pressure of 67500 kilopascal for 6 hours. As a result, HTUTs showed the broadband characteristics, for example, the center frequency, the 6 dB frequency and SNR are 5MHz, 4 MHz and 30dB, respectively. They presented excellent stability under thermal cycling between room temperature and 300°C. After 140 cycles, the signal strength deterioration was only 1 dB.

This type of HTUTs had 20 dB higher signal strength than that of sol gel thick BIT/PZT film HTUTs.

7.2- Claims of originality

The original research contributions of this thesis have been mentioned in different chapters. However, for the convenience of the reader, they are outlined below.

- BIT/PZT sol gel composite was developed. To my knowledge, this material is reported for the first time. BIT/PZT sol gel composite was sprayed onto various materials, such as steel, stainless steel, aluminum, copper, nickel, and titanium substrates. Especially BIT/PZT sprayed thick sol gel film HTUT has high operation temperature more than 450°C with high SNR (up to 40 dB), broad bandwidth at operation frequency range between 2-30 MHz and acceptable signal strength.
- Spray coating, corona poling, and silver paste top electrode were selected during fabrication processes instead of traditional methods, such as spin coating, direct high DC voltage poling, and sputtered or evaporated top electrode. These changes enabled fast and easy fabrication of HTUT onto flat and curved surfaces. With these fabrication processes, BIT/PZT HTUT showed the durability for 180 heat cycles between room temperature and 250°C. There is no report to use these processes for HTUT fabrication.
- Immersion HT probes were developed. Thickness measurement in molten zinc at 450°C and acoustic imaging in silicone oil at 200°C were successfully demonstrated. It seems that there is no commercially available immersion HT probe with a SNR more than 30 dB.

- HTUTs were fabricated onto mold inserts of injection molding and micro-molding machine. Filling completion of injection molding was successfully demonstrated by this system. It is also shown that sol gel HTUTs have the capability to monitor the entire process in real-time, non-destructively and non-invasibly.
- HTUT by diffusion bonding between LN single crystal HTUT and steel substrate was developed. This type of HTUT can operate up to 300°C with high signal strength (20 dB higher than BIT/PZT sol gel film HTUT), high SNR (about 30 dB), and broad bandwidth (center frequency: 5 MHz, 6 dB bandwidth: 4 MHz).

APPENDIX A

Predicting the properties of piezoelectric composite materials is important for material selection. A cube model for composite materials, proposed by Pauer and modified by Banno [148], is suitable for sol gel composites. Finite element [149,150] and matrix [151] methods would be also useful tools for simulating composite material properties. In this chapter, an average method [148,152] is chosen to simulate properties of sol gel sprayed composite materials, because reliable properties of pure sol gel materials are not available. Simple calculations by averaging should be adequate to predict the tendency of their properties. Modeling of composite materials in many studies mainly focused on ceramic/ polymer composites and only a few dealt with ceramic/ceramic composites, which is of interests in this thesis. It is reported that dielectric constants of PZT/PZT composite materials estimated by the cube model show reasonable agreement with experimental results [148]. However, the existence of pores in the composite film was not taken into account, and may exert significant influence.

This section discusses theoretical considerations for the dielectric constant of ceramic-ceramic composite materials with pores; then the theoretical values are compared with experimental values for PZT/PZT, LT/PZT, and BIT/PZT.

When Newnham *et al.* classified piezoelectric composites according to connectivity [152], they introduced series and parallel connection models to calculate the properties in simple linear systems, one-dimensional solutions, as shown in Figure A.1.

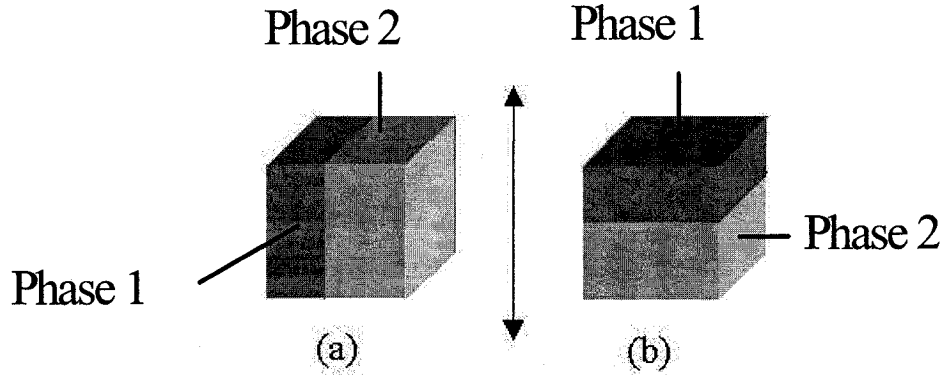


Figure A.1 Schematic representations for (a) parallel and (b) series models.

For the parallel model, the dielectric constant ϵ_3 is summarized as the following [69,152]:

$$\epsilon_3 = B_F^1 \epsilon_3^1 + B_F^2 \epsilon_3^2 \quad (\text{A.1})$$

where B_F is the volume fraction, designating phase 1 with superscript 1, and phase 2 with superscript 2. And conversely, for the series model, the following equations are given [69, 152]:

$$1/\epsilon_3 = B_F^1 / \epsilon_3^1 + B_F^2 / \epsilon_3^2 \quad (\text{A.2})$$

The cube model was proposed by Pauer [67], to obtain 0-3 composite properties using parallel and series equations. A schematic representation of 0-3 composites and a unit cell of 0-3 composite are shown in Figures A.2 and A.3, respectively. In the case where phase 1 (for example, powder) is spherical and 0 self-connectivity, and the distribution into phase 2 (for example, sol gel) is uniform, phase 1 and phase 2 compose the cubic unit cell, divided into 3 parts which exist in a combination of series and parallel phases. First the series characteristics are calculated for block 1. Then the parallel characteristics are calculated for the composite of block 1 and block 2. Finally the parallel

characteristics for the composite of block 3 and the remaining parts, block 1 and block 2, are calculated as whole material characteristics. This calculation resembles the average method, and requires only the dielectric constant ϵ_3 and volume ratio of each phase to obtain the ϵ_3 of the 0-3 composite material. Since it is relatively difficult to obtain precise elastic information for sol gel thin films, this method appears suitable.

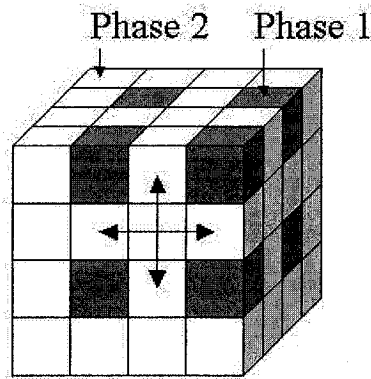


Figure A.2 Schematic representation of 0-3 composite.

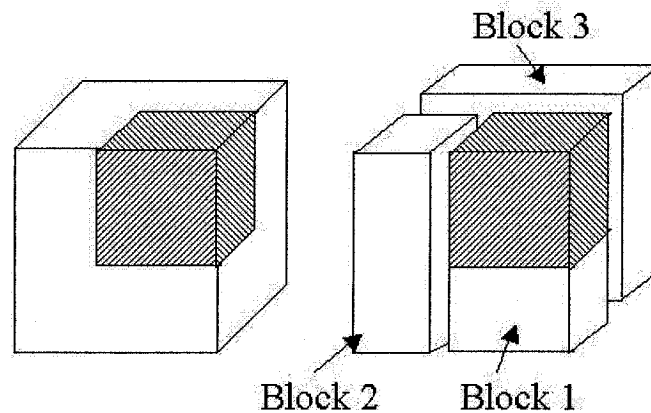


Figure A.3 Schematic representation of unit cell models for 0-3 composite material.

Sol gel composite films may be considered as a 0-3 composite material. If it is assumed that the piezoelectric powders are not connected each other in any direction, and dispersed into the sol gel phase homogeneously, the powder and sol gel phases correspond to phases 1 and 2, respectively as shown in Figure A.2. This model is simple, but it can predict dielectric, elastic, and electromechanical properties. In previous works,

theoretical values from the cube model show reasonable agreement with experimental values concerning the dielectric constant of PZT/PZT and LT/PZT [70,107]. However, the phase of the pores was not included and estimated. This effect may not be ignored, especially in the case of the sol gel spray technique, which introduces plenty pores. If it is assumed that spherical pores are dispersed throughout the PZT sol gel homogeneously, a PZT sol gel can be considered as consisting of an 0-3 composite like a pore/PZT sol gel (Phase1/Phase2). Then the piezoelectric powder and pore/PZT sol gel 0-3 composite organize the 0-3 composite as a powder/PZT sol gel with pores. In this way, it is anticipated that the existence of the pores is taken account of, and the accuracy of the calculation value may be improved.

In order to demonstrate the effectiveness of considering pores in a sol gel spray coating film, the relative dielectric constant ϵ_r of the 0-3 composite between alternative powder and PZT sol gel, such as PZT/PZT, LT/PZT and BIT/PZT were calculated in two ways, a simple cube model ignoring the existence of pores, and a double cube model including the existence of pores, with experimental data as referenced in Figure A.4. The volume ratio between the powder and the PZT sol gel was estimated at 75% from calculation using the mol % of the recipe and the densities. It was assumed that all composite materials in this section, PZT/PZT, LT/PZT, and BIT/PZT, have the same volume fraction of pores, 20 % and 40% of the whole composite material in the later calculation method. The simulation was carried out using the LabView program. It is clear that volume % of pores gives significant influence onto the dielectric constant. When the volume % of pores was set as 20 %, the simulation result showed good agreement with experimental result. Therefore the volume % of pores may be predicted by double cube model.

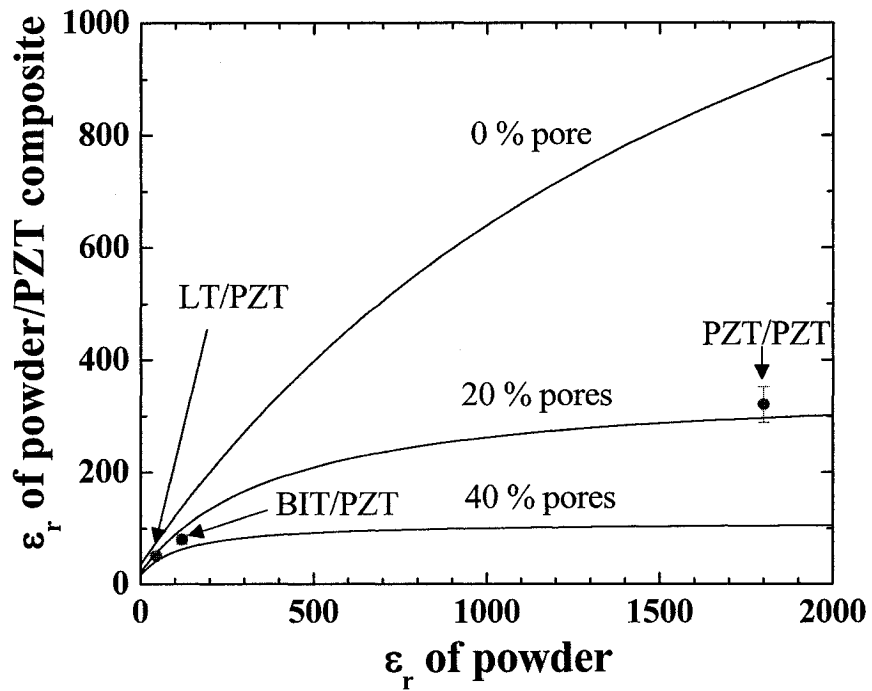


Figure A.4 Comparison of relative dielectric constant calculations of powder/PZT sol gels from conventional cube model and double cube model including pores, as a function of the relative dielectric constant of powder, with experimental results.

References

- [1] E.F. Crawley and J. de Luis, "Use of piezoelectric actuators as elements of intelligent structure", *AIAA Journal*, vol. 25, no. 10, pp. 1373-1385, 1987.
- [2] S. Mall, "Integrity of graphite/epoxy laminate embedded with piezoelectric sensor/actuator under monotonic and fatigue loads", *Smart Mater. Struct.*, vol. 11, pp 527-533, 2002.
- [3] V. Glurgutlu and J. Bao, "Embedded ultrasonic structural radar with piezoelectric wafer active sensors for the NDE of thin-wall structures", *Proceedings of IMECE 2002*, pp. 31-38, Nov. 2002.
- [4] G.S. Agnes and S. Mall, "Structural integrity issues during piezoelectric vibration suppression of composite structures", *Composites, Part B: engineering*, vol. 30, pp. 727-738, 1999.
- [5] J.R. Fothergill, P. Willis, and S. Waywell, "Development of high-temperature ultrasonic transducers for under-sodium viewing applications", *British J. NDT*, vol. 31, no. 5, pp. 259-264, May 1989.
- [6] H. Karasawa, M. Izumi, T. Suzuki, S. Nagai, M. Tamura and S. Fujimori, "Development of under-sodium three-dimensional visual inspection technique using matrix-arrayed ultrasonic transducer", *Journal of nuclear science and technology*, vol. 37, no. 9, pp. 769-779, Sep. 2000.
- [7] S. Dixon, C. Edwards, J. Reed and S.B. Palmer, "Using EMAT to measure the wall thickness of hot galvanizing kettles", *Insight*, vol. 37, no. 5, pp. 368-370, Apr. 1995.
- [8] A.R. Agrawal, I.O. Pandelidis, and M. Pecht, "Injection-molding process control-a review", *Polym. Eng. Sci.*, vol. 27, no. 18, pp. 1345-1357, Oct. 1987.
- [9] R. Gendron, J. Tatibouët, J. Guèvremont, M.M. Dumoulin and L. Piché, "Ultrasonic behavior of polymer blends", *Polym. Eng. Sci.*, vol. 35, no. 1, Mid-January, pp. 79-91, 1995.
- [10] L.C. Lynnworth, "Ultrasonic measurements for process control: theory, techniques, applications", *Academic Press Inc., San Diego*, 1989.

- [11] F. Johannaber, "Injection molding machine-a user's guide", 3rd Edition, Hanser publishers, Munich, Vienna, New York, 1997.
- [12] R. Edwards, L. Diao and C.L. Thomas, "A comparison of position, cavity pressure, and ultrasound sensors for switch/over control in injection molding", Proc. SPE ANTEC, vol. 61, pp. 586-590, 2003.
- [13] D.A. Stubbs and R.E. Dutton, "An ultrasonic sensor for high-temperature materials processing", JOM, vol. 49, pp. 29-31, Sep. 1996.
- [14] L. Piché, D. Lévesque, R. Gendron and J. Tatibouët, "On-line ultrasonic characterization of polymer flows", Proc. VIth Symp. on Nondestructive characterization of Materials, pp. 37-44, 1994.
- [15] L. Piché, A. Hamel, R. Gendron, M.M. Dumoulin, and J. Tatibouët, "Ultrasonic characterization of polymer melts under processing conditions", US Patent, 5,433,112, July 18, 1995.
- [16] D.O. Kazmer, R.X. Gao, C.B. Theurer and L. Zhang, "Wireless pressure sensor for injection molding", Proc. SPE ANTEC, vol. 61, pp. 3290-3294, 2003.
- [17] C. Kiehl, L.-L. Chu, K. Letz and K. Min, "On-line ultrasonic measurement of methyl methacrylate polymerization for application to reactive extrusion", Polym. Eng. Sci., vol. 41, no. 6, pp. 1078-1086, June 2001.
- [18] H. Wang, B. Cao, C.-K. Jen, K.T. Nguyen, and M. Viens, "On-line ultrasonic monitoring of the injection molding process", Polym. Eng. Sci., vol. 37, no. 2, pp. 363-376, Feb. 1997.
- [19] S.-S.L. Wen, C.-K. Jen, and K.T. Nguyen, "Advances in on-line monitoring of the injection molding process using ultrasonic techniques", Intern. Polym. Processing XIV, vol. 2, pp. 175-182, 1999.
- [20] M.T. Martyn, B. Whiteside, P.D. Coates, P.S. Allan, G. Greenway, and P. Hornsby, "Micromoulding: Consideration of processing effects on medical materials", Proc. SPE ANTEC, vol. 61, pp. 2582-2586, 2003.
- [21] J.-W. Choi, S. Kim, R. Trichur, H.J. Cho, A. Puntambekar, R.L. Cole, J.R. Simkins, S. Murugesan, K. Kim, J.-B. Lee, G. Beaucage, and C.H. Ahn, "A plastic micro injection molding technique using replaceble mold-disks for

- disposable microfluidic systems and biochips”, *Micro Total Analysis Systems*, pp. 411-412, 2001.
- [22] A. Rankin and P. Manser, “Small is the big issue: micro moulding”, *Medical Device Technology Magazine*, pp. 18-20, Dec. 2002.
- [23] M. Kobayashi, C.-K. Jen, C. Corbeil, Y. Ono, H. Hébert, and A. Derdouri, “High temperature ultrasonic transducers for monitoring of micro-molding”, *Proc. IEEE Ultrason. Symp.*, pp. 693-698, 2003.
- [24] C.-K. Jen, Z. Sun, M. Kobayashi, M. Sayer, and C.-K. Shih, “Application of ultrasound in the determination of fundamental extrusion performance: barrel and screw wear measurement”, *Proc. SPE ANTEC, #935*, pp. 1-5, 2002.
- [25] S.H. Collins, “Screw and barrel wear, Part I: The causes”, *Plastic Compounding*, pp. 113-124, May/June 1982.
- [26] R.A. Worth and R.A.L. Fook, “Factors affecting the wear of extruder screws”, *Plastics and Rubber: Processing*, pp. 68-72, Jun. 1978.
- [27] S.H. Collins, “Screw and barrel wear, Part II: Prevention and remedy”, *Plastic Compounding*, pp. 16-28, July/August 1982.
- [28] B.H. Maddock, “Effect of wear of their delivery capacity of extruder screws”, *SPE J.*, pp. 433-434, May 1959.
- [29] M. Kobayashi, T. R. Olding, M. Sayer, and C.-K. Jen, “Piezoelectric thick film ultrasonic transducers fabricated a sol-gel spray technique”, *Ultrasonics*, vol. 39, pp. 675-680, 2002.
- [30] D.R. França, C.-K. Jen, K.T. Nguyen, and R. Gendron, “Ultrasonic in-line monitoring of polymer extrusion”, *Polym. Eng. Sci.*, vol. 40, no. 1, pp. 82-94, Jan. 2000.
- [31] C.-K. Jen, B. Cao, K.T. Nguyen, C.A. Loong, and J.-G. Legoux, “On-line ultrasonic monitoring of a die-casting process using buffer rods”, *Ultrasonics*, vol. 35, pp. 335-344, 1997.
- [32] A. McNab, K.J. Kirk, and A. Cochran, “Ultrasonic transducers for high temperature applications”, *IEE Proc.-Sci. Meas. Technol.*, vol. 145, no. 5, pp. 229-236, Sep. 1998.

- [33] J. Soejima, K. Sato, and K. Nagata, "Fabrication and properties of PbNb_2O_6 ceramics for high-temperature transducer", *Key Engineering Materials*, vol. 181-182, pp. 41-44, 2000.
- [34] C.-K. Jen, J.-G. Legoux, and L. Parent, "Experimental evaluation of clad metallic buffer rods for high temperature ultrasonic measurements", *NDT&E International*, vol. 33, pp. 145-153, 2000.
- [35] K. Balasubramaniam, V.V. Shah, R.D. Costley, G. Boudreaux, and J.P. Singh, "High temperature ultrasonic sensor for the simultaneous measurement of viscosity and temperature of melts", *Review of Science Instruments*, vol. 70, no. 12, pp. 4618-4623, Dec. 1999.
- [36] T.L. Jordan and Z. Ounaies, "Piezoelectric ceramics characterization", NASA/CR-2001-211225, ICASE Report No. 2001-28, Sep. 2001.
- [37] K. Kawashima, K. T. Hyoguchi and T. Akagi, "On-line measurement of plastic strain ratio of steel sheet using resonance mode EMAT", *Journal of Nondestructive Evaluation*, vol.12, no.1, pp. 71-77, Mar. 1993.
- [38] H. Shimizu, H. Watanabe and M. Sato, "Noncontacting electromagnetic acoustic transducer for separately detecting longitudinal and transverse waves in metals and its application to AE sensor", *Jpn. J. Appl. Phys. Suppl.*, vol.23, suppl.23-1, pp. 116-118, 1984.
- [39] B.W. Maxfield and C.M. Fortunko, "The design and use of electromagnetic acoustic wave transducers (EMATs)", *Material Evaluation*, vol. 41, no. 12, pp. 1399-1408, Nov. 1983.
- [40] B. Butler, S. B. Palmer and G. J. Primavesi, "Techniques for the generation of ultrasound for extended periods at high temperatures", *Ultrasonics*, vol. 17, no. 6, pp. 249-254, Nov. 1979.
- [41] D.T. Quebeillalt and H. N.G. Wadley, "Temperature dependence of the elastic constants of solid and liquid $\text{Cd}_{0.96}\text{Zn}_{0.04}\text{Te}$ obtained by laser ultrasound", *J. Appl. Phys.*, vol. 83, no. 8, pp. 4124-4133, 1998.
- [42] D. Drolet, A. Blouin, J.-P. Monchalain, P. Bouchard, M. Choquet, C. Padioleau, G. Durou and R. Héon, "Laser-ultrasonics: a noncontact technique for industrial inspection of materials", *Industrial Materials Institute, Boucherville*, 1996.

- [43] H. Nakano and S. Nagai, "Crack measurements by laser ultrasonic at high temperature", *Jpn. J. Appl. Phys.*, vol. 32, no. 5B, pp. 2540-2542, 1993.
- [44] C.B. Scruby and L.E. Drain, "Laser-ultrasonics: techniques and applications", Adam Hilger, Bristol, 1990.
- [45] R.C. Turner, P.A. Fuierer, R.E. Newnham, and T.R. ShROUT, "Materials for high temperature acoustic and vibration sensors: a review", *Applied Acoustics*, vol. 41, pp. 299-324, 1994.
- [46] N.D. Patel, S.X. Fulford, and P.S. Nicholson, "High frequency-high temperature ultrasonic transducers", *Review of Progress in Quantitative Nondestructive Evaluation*, vol. 9, Plenum Press, pp. 823-828, 1990.
- [47] R. Hauser, L. Reindl, and J. Biniash, "High-temperature stability of LiNbO₃ and quartz based SAW devices", *Proc. IEEE Ultrason. Symp.*, pp. 192-195, 2003.
- [48] J. Kushibiki, I. Takanaga, M. Arakawa, and T. Sannomiya, "Accurate measurements of the acoustical physical constants of LiNbO₃ and LiTaO₃ single crystal", *IEEE Trans. Ultrason., Ferroelect., Freq. Contr.*, vol. 46, no. 5, pp. 1315-1323, Sep. 1999.
- [49] N.D. Patel and P.S. Nicholson, "High frequency, high temperature ultrasonic transducers", *NDT International*, vol. 23, no. 5, pp. 262-266, 1990.
- [50] H. Ogi, N. Nakamura, K. Sato, M. Hirao, M., and S. Uda, "Elastic, anelastic, and piezoelectric coefficients of langasite: resonance ultrasound spectroscopy with laser-Doppler interferometry", *IEEE Trans. Ultrason., Ferroelect., Freq. Contr.*, vol. 50, no. 5, pp. 553-560, May 2003.
- [51] D.S. Kupperman and R.N. Lanham, "Ultrasonic shear wave couplant", *US Patent 4,559,827*, Dec. 24, 1985.
- [52] B. Butler, S.B. Palmer, and G.J. Primavesi, "Technique for the generation of ultrasound for extended periods at high temperature", *Ultrasonics*, vol. 17, pp. 249-254, 1979.
- [53] K.J. Kirk, A. McNab, A. Cochran, I. Hall, and G. Hayward, "Ultrasonic arrays for monitoring cracks in an industrial plant at high temperature", *IEEE Trans. Ultrason., Ferroelect., Freq. Contr.*, vol. 46, no. 2, pp. 311-319, Mar. 1999.

- [54] H. Mrasek, D. Gohlke, K. Matthies, and E. Neumann, "High temperature ultrasonic transducers", NDTnet (web journal), vol. 1, no. 9, Sep. 1996.
- [55] T.N. Nguyen, M. Lethiecq, B. Karlsson and F. Patat, "Development of a broadband ultrasonic transducer for high temperature applications", *Acta Acustica*, vol. 3, pp. 331-338, Aug. 1995.
- [56] M.C. Bhardwaj, "Temperature independent ultrasound transducer device", US Patent 4,703,656, Nov. 3, 1987.
- [57] C.-K. Jen, Z. Sun and M. Kobayashi, "Ultrasonic monitoring of barrel wear and screw status", *Proc. SPE ANTEC*, pp.402-406, May 2004.
- [58] A.-U. Rehman, C.-K. Jen, and I. Ihara, "Ultrasonic probes for high temperature immersion measurements", *Meas. Sci. Technol.*, vol. 12, pp. 1-7, 2001.
- [59] J.D. Greathouse, "Portable high temperature ultrasonic testing (UT) piezo probe with cooling apparatus", US Patent 5,936,163, Aug. 10, 1999.
- [60] C.-K. Jen, K.T. Nguyen, B. Cao, H. Wang, and C.A. Loong, "Ultrasonic sensors for on-line monitoring of castings and molding processes at elevated temperatures", US Patent 5,951,163, Sep. 14, 1999.
- [61] C.-K. Jen, J.-W. Liaw, T.-F. Chen, A. Moreau, J.-P. Monchalain, and C.-C. Yang, "Ultrasonic evaluation of semi-solid metals during processing", *Meas. Sci. Technol.*, vol. 11, pp. 1-6, 2000.
- [62] T. Graham, "On the properties of silicic acid and other analogous colloidal substrates", *J. Chem. Soc.*, vol. 17, pp. 318-327, 1864.
- [63] K.D. Budd, S.K. Dey, and D.A. Payne, "Sol gel processing of PbTiO_3 - PbZrO_3 thin films", *Br. Ceram. Proc.*, vol. 36, pp. 107-121, 1985.
- [64] G. Yi, Z. Wu, and M. Sayer, "Preparation of $\text{Pb}(\text{Zr,Ti})\text{O}_3$ thin films by sol gel processing: electrical, optical and electro-optic properties", *J. Appl. Phys.*, vol. 64, pp. 2717-2724, 1988.
- [65] R.W. Schwartz, R.A. Assink, and T.J. Headley, "Spectroscopic and microstructural characterization of solution chemistry effects in PZT thin film processing", *Mat. Res. Soc. Symp. Proc.*, vol. 243, pp. 245-254, 1992.
- [66] G. Yi and M. Sayer, "Sol-gel processing of complex oxide films", *Ceram. Bull.*, vol. 70, no. 7, pp. 1173-1179, 1991.

- [67] M. Sayer, M. Lukacs, T. Olding, G. Pang, L. Zou, and Y. Chen, "Piezoelectric films and coating for device purposes", *Mat. Res. Soc. Symp. Proc.*, vol. 541, pp. 599-610, 1999.
- [68] D.A. Barrow, T.E. Petroff, and M. Sayer, "Method for producing thick ceramic films by a sol gel coating process", US Patent 5,585,136, Dec. 17, 1996 (RE 36,573, Feb. 2000).
- [69] L. Zou, M. Sayer, and C.-K. Jen, "Sol-gel fabricated thick piezoelectric ultrasonic transducers for potential applications in industrial material processes", *Proc. IEEE Ultrason. Symp.*, pp. 1007-1011, 1997.
- [70] M. Kobayashi and C.-K. Jen, "Piezoelectric Thick Bismuth Titanate/PZT Composite Film Transducers for Smart NDE of Metals", *Smart Materials and Structures* in press.
- [71] J.-S. Chang, P.A. Lawless, and T. Yamamoto, "Corona discharge processes", *IEEE Trans. Plasma Sci.*, vol. 19, no. 6, pp. 1152-1166, Dec. 1991.
- [72] D. Waller, T. Lqbal, and A. Safari, "Poling of lead zirconate titanate ceramics and flexible piezoelectric composites by the corona discharge technique", *J. Am. Ceram. Soc.*, vol. 72, no. 2, pp. 322-324, Feb. 1989.
- [73] N. Tohge, Y. Fukuda, and T. Minami, "Formation and properties of ferroelectric $\text{Bi}_4\text{Ti}_3\text{O}_{12}$ films by the sol-gel process", *Jpn. J. Appl. Phys.*, vol. 31, pt. 1, no. 12A, pp. 4016-4017, Dec. 1992.
- [74] P. Fuierer and B. Li, "Nonepitaxial orientation in sol-gel bismuth titanate films", *J. Am. Ceram. Soc.*, vol. 85, no. 2, pp. 299-304, 2002.
- [75] C.D. Coxé, "Joining of non-metallic materials and brazing filler rods therefore", US Patent 2,739,375, Mar. 27, 1956.
- [76] H.A. Omley, "Metal-to-ceramic seal", US Patent 2,917,140, Dec. 15, 1959.
- [77] J.F. Clarke, "Ceramic brazing means", US Patent 3,382,052, May 7, 1968.
- [78] K. Iinuma and E. Itamura, "Method of manufacturing an ultrasonic probe", US Patent 3,952,387, Apr. 27, 1976.
- [79] K. Iinuma and E. Itamura, "Method of manufacturing an ultrasonic probe", US Patent 3,952,387, Apr. 27, 1976.

- [80] D.L. Arenberg, "Method of bonding and article thereby formed", US Patent 2,754,238, Jul. 10, 1956.
- [81] F.K. Sittig and H.D. Cook, "A method for preparing and bonding ultrasonic transducers used in high frequency digital delay lines", Proc. IEEE, pp. 1375-1376, Aug. 1968.
- [82] J.D. Knox, "Method of bonding two bodies together", US Patent 3,921,885, Nov. 25, 1975.
- [83] T. Watanabe, "Piezoelectric vibrator", EU Patent 1,104,099,A9, Aug. 29, 2001.
- [84] G.O. Dayton, W.A. Schulze, T.R. Shrout, S. Swartz, and J.V. Biggers, "Fabrication of electromechanical transducer materials by tape casting", *Advances in Ceram.*, vol. 9, pp. 24-27, Apr. 1983.
- [85] X. Zhao, J.R.G. Evans, and M.J. Edirisinghe, "Direct ink-jet printing of vertical walls", *J. Am. Ceram. Soc.*, vol. 85, no. 8, pp. 2113-2115, 2002.
- [86] M. Koch, N. Harris, R. Maas, A.G.R. Evans, N. M. white, and A. Brunnschweiler, "A novel micropump design with thick-film piezoelectric actuation", *Meas. Sci. Technol.*, vol. 8, pp.49-57, 1997.
- [87] H. Adachi, Y. Kuroda, T. Imahashi and K. Yanagisawa, "Preparation of piezoelectric thick films using a jet printing system", *Jpn. J. Appl. Phys.*, vol. 36, pt. 1, no. 3A, pp. 1159-1163, Mar. 1997.
- [88] N. Katsura, M. Ishikawa, T. Sato, M. Takeuchi, N. Kawashima, M. Kurosawa, and S. Takeuchi, "Development of water immerse type ultrasound probe with PZT film deposited by hydrothermal method", *Proc. IEEE Ultrason. Symp.*, pp. 1300-1305, 2003.
- [89] D.A. Barrow, "Thick ceramic films: macroscopic piezoelectric actuators and novel coatings", Ph. D. thesis, Department of Physics, Queen's University, Kingston, 1995.
- [90] B. Jaffe, W.R. Cook, and H. Jaffe, "Piezoelectric ceramics", *Non-Metallic Solids*, vol. 3, Academic Press, 1971.
- [91] B. Jaffe, R.S. Roth, and S. Marzullo, "Properties of piezoelectric ceramics in the sold-solution series lead titanate-lead zirconate-lead oxide: tin oxide and lead

- titanate-lead hafnate”, Journal of Research of the National Bureau of Standards, vol. 55, no. 5, pp. 239-254, Nov. 1955.
- [92] A.A. Ballman, “Growth of piezoelectric and ferroelectric materials by the Czochralski technique”, J. Am. Ceram. Soc., vol. 48, no. 2, pp. 112-113, Feb. 1965.
- [93] B. Aurivillius, Arkiv Kemi., vol. 1, pp. 499, 1949.
- [94] R. Kazys, A. Voleisis, L. Mazeika, R. Sliteris, R.V. Nieuwenhove, P. Kupschus, and H.A. Abderrahim, “Investigation of ultrasonic properties of a liquid metal used as a coolant in accelerator driven reactors”, Proc. IEEE Ultrason. Symp., pp. 815-818, 2002.
- [95] M. Toyoda, Y. Hamaji, K. Tomono and D.A. Payne, “Ferroelectric Properties and fatigue characteristics of $\text{Bi}_4\text{Ti}_3\text{O}_{12}$ thin films by sol-gel processing”, Jpn. J. Appl. Phys., vol. 33, pt. 1, no. 9B, pp. 5543-5548, Sep. 1994.
- [96] S.Y. Wu, W.J. Takei, and M.H. Framcombe, “Optical switching characteristics of epitaxial bismuth titanate films for matrix-addressed displays”, Ferroelectrics, vol. 10, pp. 209-213, 1976.
- [97] P.C. Joshi, A. Mansingh, M. N. Kamalasanan, and S. Chandra, “Structural and optical properties of $\text{Bi}_4\text{Ti}_3\text{O}_{12}$ thin films by sol-gel technique”, Appl. Phys. Lett. 59 (19), pp. 2389-2390, Nov. 1991.
- [98] M. Sedlar and M. Sayer, “Structural and Electrical properties of ferroelectric Bismuth Titanate thin films prepared by the sol gel method”, Ceram. Int., 22, pp. 241-247, 1996.
- [99] H. Gu, C. Dong, P. Chen, D. Bao, A. Kuang and X. Li, “Structural, morphology and electrical studies on ferroelectric bismuth titanate thin films prepared by sol-gel technique, J. Crystal Growth, vol. 237-239, pt. 1, pp. 468-472, 2002.
- [100] D.C. Giancoli, “Physics: For scientists and engineers”, 2nd Edition, Prentice-Hall, 1988.
- [101] J. Kim, S.H. Kim, J.-P. Kim, Y.-H. Hwang, and M. S. Jang, “A study of grain size dependent ferroelectric properties of annealed amorphous $\text{Bi}_4\text{Ti}_3\text{O}_{12}$ ”, J. Korean Phys. Soc., vol. 35, pp. S1465-S1468, Dec. 1999.

- [102] T. Yamamoto, K. Urabe, and H. Banno, "BaTiO₃ particle-size dependence of ferroelectricity in BaTiO₃/Polymer composites", *Jpn. J. Appl. Phys.* vol. 32, part 1, no. 9B, pp. 4272-4276, Sep. 1993.
- [103] S. S. Chiang, R. M. Fulrath, and J. A. Pask, "Influence of microcracking and slow crack growth on the planar coupling coefficient in PZT", *Communi. Am. Ceram. Soc.*, pp. 141-143, Oct. 1981.
- [104] "IEEE standard definitions of primary ferroelectric terms", ANSI/IEEE Std. 180-1986.
- [105] Z.A. Weinberg, W.C. Johnson, and M.A. Lampert, "High Field Transport in SiO₂ on silicon induced by corona charging of the unmetallized surface", *J. Appl. Phys.*, vol. 47, no. 1, pp. 248-255, 1976.
- [106] Y. Wada and R. Hayakawa, "A model theory of piezo- and pyroelectricity of poly(vinylidene fluoride) electret", *Ferroelectrics*, vol. 32, pp. 115-118, 1981.
- [107] D.A. Barrow, T.E. Petroff, R.P. Tandon, M. Sayer, "Characterization of thick lead zirconate titanate films fabricated using a new sol gel based process", *J. Appl. Phys.*, vol. 81, no. 2, pp. 876-881, Jan. 1997.
- [108] D. Barrow, V. Kumar, R. Pascual, and M. Sayer, "Crystallization of sol gel PZT on aluminum and platinum metallisations", *Proc. Mat. Res. Soc. Symp.*, vol. 243, pp. 113-122.
- [109] L.C. Klein, Ed., "Sol-gel optics: processing and applications", Kluwer, Boston, MA, 1993.
- [110] "IEEE standard on piezoelectricity", ANSI/IEEE Std. 176-1987.
- [111] Z. Wang, Y. Zhang, and J. D. N. Cheeke, "Characterization of Electromechanical coupling coefficients of piezoelectric films using composite resonators", *IEEE Trans. Ultrason., Ferroelect., Freq. Contr.*, vol. 46, no. 5, pp. 1327-1330, Sep. 1999.
- [112] Y. Zhang, Z. Wang, and J. D. Cheeke, "Resonant spectrum method to characterize piezoelectric films in composite resonators", *IEEE Trans. Ultrason., Ferroelect., Freq. Contr.*, vol. 50, no. 3, pp. 321-333, Mar. 2003.

- [113] D.A. Berlincourt, D.R. Curran and H. Jaffe, "Piezoelectric and piezomagnetic materials and their function in transducers", *Physical Acoustics*, vol. 1, pt. A, Chapter 3, pp. 169-270, 1964.
- [114] M. Lukacs, T. Olding, and M. Sayer, "Thickness mode material constants of a supported piezoelectric film", *J. Appl. Phys.*, vol. 85, no. 5, pp. 2835-2843, Mar. 1999.
- [115] R.S. Naik, J.L. Lutsky, R. Reif and C.G. Sodini, "Electromechanical coupling constant extraction of thin-film piezoelectric materials using a bulk acoustic wave resonator", *IEEE Trans. Ultrason., Ferroelect., Freq. Contr.*, vol. 45, no. 1, pp. 257-263, Jan. 1998.
- [116] E.K. Sittig, "Design and technology of piezoelectric transducers for frequencies above 100MHz", in *Physical Acoustics*, vol. IX, W.P. Mason and R.N. Thurston, Eds. New York, Academic Press, 1964, pp. 221-275.
- [117] I. Ihara, C.-K. Jen, and D.R. França, "Ultrasonic imaging, particle detection, and $V(z)$ measurements in molten zinc using focused clad buffer rods", *Review of Scientific Instruments*, vol. 71, no. 9, pp. 3579-3586, Sep. 2000.
- [118] Y. Ono, M. Kobayashi, J.-F. Moisan, and C.-K. Jen, "High temperature and broadband immersion ultrasonic probes," submitted to *IEEE Sensors Journal*, June 2004.
- [119] N. Nakaso, Y. Tsukahara, S. Ishikawa, and K. Yamanaka, "Diffraction-free propagation of collimated SAW around a quartz ball", *Proc. IEEE Ultrason. Symp.*, pp. 47-52, 2002.
- [120] K. Yamanaka, S. Ishikawa, N. Nakaso, N. Takeda, T. Mihara, and Y. Tsukahara, "Ball SAW device for hydrogen gas sensor", *Proc. IEEE Ultrason. Symp.*, pp. 299-302, 2003.
- [121] N.N. Hsu, D. Xiang, S.E. Fick and G.V. Blessing, "Time and polarization resolved ultrasonic measurements using a lensless line-focus transducer", *Proc. IEEE Ultrason. Symp.*, pp. 867-871, Nov. 1995.
- [122] N. Chubachi, J. Kushibiki, T. Sannomiya, and Y. Iyama, "Performance of scanning acoustic microscope employing concave transducers", *Proc. IEEE Ultrason. Symp.*, pp. 415-418, Nov. 1995.

- [123] K. Uchino, "Piezoelectric actuators and ultrasonic motors", Kluwer Academic, Boston, MA, 1997.
- [124] G.S. Kino, "Acoustic Waves: Devices, Imaging, and Analog Signal Processing", Englewood Cliffs, Prentice-Hall, pp. 182-194, 1987.
- [125] W. Kroebel and K.-H. Mahrt, "Recent results of absolute sound velocity measurements in pure water and sea water at atmospheric pressure," *Acustica*, vol. 35, pp. 154-164, 1976.
- [126] C.B. Scruby and B.C. Moss, "Non-contact ultrasonic measurements on steel at elevated temperatures," *NDT & E Int.*, vol. 26, no. 4, pp. 177-188, 1993.
- [127] K. Saito and M. Kawabuchi, "Ultrasonic probe", US Patent, no. 5,030,874, July, 1991.
- [128] H. William, "Fourier transform spectral methods", *Numerical Recipes*, chapter 12, pp. 381-416, Cambridge University Press, 1986.
- [129] L.E. Daigneault, R. Gendron, M.M. Dumoulin, and J. Tatibouët, "Monitoring the peroxide degradation of polypropylene", *Proc. Polym. Processing Society, Americas Meeting 163*, pp. 161-162, 1992.
- [130] J. Tatibouët, A. Hamel, and L. Piché, "Ultrasound as monitoring tool for polymer degradation and reactive extrusion", *Proc. Polym. Processing Society, 15th Annual Meeting*, 1999.
- [131] R. Gendron, L. Piché, A. Hamel, M.M. Dumoulin, and J. Tatibouët, "Ultrasonic characterization of extrusion instabilities", *SPE ANTEC*, vol. 55, pp. 2254-2258, 1997.
- [132] Z. Sun, C.-K. Jen, C.-K. Shih, and D.A. Denelsbeck, "Application of ultrasound in the determination of fundamental extrusion performance: Residence time distribution measurement", *Polym. Eng. Sci.*, vol. 43, no. 1, pp. 102-111, Jan. 2003.
- [133] M. Kobayashi, Y. Ono, C.-K. Jen and C.-C. Cheng, "High temperature ultrasonic transducers and its application for injection molding process monitoring", submitted to *IEEE Trans. Ultrasonics, Ferroelectrics and Freq. Control*, Nov. 2003.

- [134] Y. Ono, M. Kobayashi, C.-K. Jen, C.-C. Cheng, A. Derdouri, and Y. Simard, "Real-time, non-intrusive and non-destructive ultrasonic monitoring of injection and co-injection molding processes", Proc. SPE ANTEC, pp. 556-560, May 2004.
- [135] L. Piche, F. Massines, A. Hamel, and C. Neron, "Ultrasonic characterization of polymers under simulated processing conditions," US Patent 4,754,645, July 5 1988.
- [136] H.A. Rundle and J.E. Kowles, "High temperature ultrasonic transducer", US Patent 3,781,576, Dec. 25, 1973.
- [137] J.G. Rumbold and J.W. Raisch, "Ultrasonic transducer apparatus and method for high temperature measurements", US Patent, 4,567,770, Feb. 4, 1987.
- [138] C.-K. Jen and J.-G. Legoux, "Clad ultrasonic waveguides with reduced trailing echoes", US Patent, 5,828,274, Oct. 1998.
- [139] M.M. Schwartz, "Ceramic joining", ASM International, Materials Park, OH, 1990.
- [140] "The brazing book online", the web book provided by Handy & Harman, Canada.
- [141] "Diffusion bonding of materials", Edited by N. F. Kazakov, Mir Publishers, Moscow, Pergamon Press, English translation, 1985.
- [142] "Joining of advanced materials", R.W. Messler, Jr., Butterworth-Heinemann, 1993.
- [143] D. L. Arenberg, "Method of bonding and article thereby formed", US Patent, 2,754,238, July 10, 1956.
- [144] R. E. Allen, "Delay line bond", U. S. Patent, 3,252,722, May 24, 1966.
- [145] J. R. Chase and J. A. Rimer, "Method for bonding a crystal to a solid delay medium", US Patent, 3,590,467, July 6, 1971.
- [146] C. J. Dunnrowich and J. Callera, "Ultrasonic transducer and its method of manufacture", US Patent 4,434,384, Feb. 28, 1984.
- [147] Y.S. Kim and R.T. Smith, "Thermal expansion of lithium tantalate and lithium niobate single crystal", J. Appl. Phys., vol. 40, no. 11, pp. 4637-4641, Oct. 1969.
- [148] H. Banno and S. Saito, "Piezoelectric and dielectric properties of composites of synthetic rubber and PbTiO_3 or PZT", Jpn. J. Appl. Phys., vol. 22, suppl., pp. 67-69, 1983.

- [149] K.Y. Hashimoto and M. Yamaguchi, "Elastic, piezoelectric and dielectric properties of composite materials", Proc. IEEE Ultrason. Symp., pp.697-702, 1986.
- [150] M. Yamaguchi, K.Y. Hashimoto, and H. Makita, "Finite element method analysis of dispersion characteristics for 1-3 type piezoelectric composites", Proc. IEEE Ultrason. Symp., pp. 657-661, 1987.
- [151] F. Levassort, and M. Lethiecq, "Modeling of highly loaded 0-3 piezoelectric composites using a matrix method", IEEE Trans. Ultrason., Ferroelect., Freq. Contr., vol. 45, no. 6, pp. 1497-1505, November 1998.
- [152] R.E. Newnham, D.P. Skinner, and L.E. Cross, "Connectivity and piezoelectric-pyroelectric composites", Mat. Res. Bull., vol.13, pp. 525-536, 1978.